

# A Study of the Physics and Chemistry of Knock in Modern SI Engines and Their Relationship to the Octane Tests

by

Vikram Mittal

B.Sc. (with honors), Engineering and Applied Sciences  
California Institute of Technology, 2003

M.Sc (*Oxon.*), Engineering Sciences  
University of Oxford, 2005

Submitted to the Department of Mechanical Engineering  
In Partial Fulfillment of the Requirements for the Degree of

Doctorate of Philosophy in Mechanical Engineering

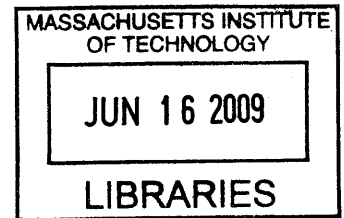
at the

Massachusetts Institute of Technology

June 2009

© 2009 Massachusetts Institute of Technology  
All Rights Reserved

**ARCHIVES**



Signature of Author .....

Department of Mechanical Engineering  
May 2009

Certified by .....

John B. Heywood  
Sun Jae Professor of Mechanical Engineering  
Thesis Adviser

Accepted by .....

David Hardt  
Ralph E. and Eloise F. Cross Professor of Mechanical Engineering  
Chairman, Department of Graduate Committee



# **A Study of the Physics and Chemistry of Knock in Modern SI Engines and Their Relationship to the Octane Tests**

by

Vikram Mittal

Submitted to the Department of Mechanical Engineering  
on May 21, 2005 in Partial Fulfillment of the  
Requirements for the Degree of Doctor of Philosophy in  
Mechanical Engineering

## **ABSTRACT**

Avoiding knock is the major design constraint for spark ignition engines because of the unacceptable noise and engine damage associated with it. Hence, the Research and Motor Octane Number (RON and MON) tests were established in 1928 such that a fuel with a higher RON and MON is less likely to knock than a fuel with a lower value. However, engine and fuel technology has evolved since 1928, and thus the relevancy of these tests for modern engines needed to be evaluated. First, the study compared knock onset, knock metrics, reference fuels, and test conditions for the octane tests to those in modern engines. The results showed that in modern engines, for a given RON, fuels with lower MON values performed better than fuels with higher values, and this trend becomes stronger when engines are boosted and intercooled. Second, detailed chemical kinetics models were used to study fuel autoignition phenomena leading to knocking conditions. These models showed that the fuel autoignition chemistry in modern engine is different from that in the RON and MON tests. Based on these results, it was concluded that the RON and MON tests no longer represent modern engine operating conditions; therefore, modifications are suggested and evaluated to improve the tests' applicability.

Thesis Advisor: John B. Heywood  
Title: Sun Jae Professor of Mechanical Engineering

(this page intentionally left blank)

## AWKNOWLEDGEMENTS

### (THE PORTION OF MY THESIS MOSTLY LIKELY TO BE READ / SCRUTINIZED)

There are many people to whom I want to thank. This list is only a partial list because a full list would be longer than this thesis.

**My Advisor: Prof. John Heywood**

Thank you for your guidance and molding me into the engineer that I am today. Forty years from now, I aspire to be the man that you are.

**My Sponsors: The Engines and Fuels Consortium**

Thank you for your financial, moral, and technical support. In particular, I want to thank Gautam Kalghatgi of Shell and Ahmar Ghauri of Saudi-Aramco.

**My Thesis Committee: Prof. Heywood, Prof. Cheng, Prof. Ghoniem, and Prof. Green**

Thank you for pointing me in the right directions and (hopefully) letting me graduate.

**My Colleagues of the Sloan Automotive Laboratory**

This work was a collaborative effort from everyone in the lab. Whether I was turning bolts, replacing pistons, learning Fortran, writing chemical models, or complaining about my research there was always someone to lend a hand. In particular, I want to thank Craig Wildman, Vince Costanzo, Amir Maria, Emmanuel Kasseris, Dongkun Lee, Jeff McAuley, Alex Sappok, and Steve Przesmitski. I also want to thank Thane Dewitt, Raymond Phan, Janet Maslow, and Karla Stryker for taking care of the logistics of my work here and for always being an open ear. And finally, I want to thank Anselmo “Sam” Brum and Norma; you always seemed to find a way to pick me up.

**My Parents: Vijay and Ameeta Mittal**

Thank you for your continual support and bestowing on me the drive and work-ethic needed to accomplish this research.

**My Brother, Vikas Mittal**

Thank you for always being supportive about every path that I choose to take.

**My Fiancée: Ankita Deshpande**

Thank you for your love.

**My Best Friends: Ryan James and Andrew Homyk**

Thank you for helping me through some difficult times, even from thousands of miles away.

**My Apartment Mates: Vince Costanzo, Paul Njoroge, John Addison, and Craig Wildman**

Thank you for reminding me that there is life outside of lab.

**My Running Friends: Dan Coskren, David Hagerstrom, Seth Miles, and Dino DiBiaso**

Thank you for keeping me sane.

**My US Army Instructors: LTC McGonagle, LTC Hall, DS Murphy, amongst many others**

Thank you for molding me into a leader.

(this page intentionally left blank)

## TABLE OF CONTENTS

Abstract .....	3
Acknowledgements .....	5
List of Tables .....	11
List of Figures .....	13
Chapter 1: Introduction .....	17
1.1 Overview of Knock .....	17
1.2 The Octane Scale .....	21
1.3 Modern Engine Trends and Knock .....	23
1.4 Goals of Study .....	25
Chapter 2: Experimental Apparatus and Modeling Tools .....	27
2.1 Engine Setup .....	27
2.1.1 Test Engine and Instrumentation .....	27
2.1.2 Air and Fuel Systems .....	30
2.2 WAVE Models .....	32
2.3 Chemical Models .....	33
Chapter 3: Evaluation of Different Knock Metrics .....	37
3.1 Commonly Used Knock Metrics .....	37
3.2 Experimental Procedures .....	38
3.3 Results .....	39
3.4 Conclusions .....	46
Chapter 4: Physics of Knock in Modern Engines Compared to the Octane Number Tests .....	47
4.1 Phenomena that Govern Knock Onset in Modern SI Engines .....	47
4.1.1 Dependence of Knock Onset on In-Cylinder Pressure .....	47
4.1.2 Experimental Procedures .....	48
4.1.3 Results and Discussion .....	49
4.2 Phenomena that Govern Knock in the Octane Number Tests .....	58
4.3 Differences between Knock in Modern SI Engines and CFR Engines .....	60
4.4 Conclusions .....	63
Chapter 5: The Dependence of K Values on Different Engine Parameters .....	65
5.1 Experimental Study .....	65
5.1.1 Experimental Procedures .....	65
5.1.2 Experimental Fuels .....	67
5.1.3 How Sensitivity Affects Knock Limits .....	68
5.1.4 The Dependence of K on Different Parameters .....	71
5.1.4.1 Spark Location .....	72

5.1.4.2 Compression Ratio. . . . .	73
5.1.4.3 Relative Air/Fuel Ratio. . . . .	74
5.1.4.4 Engine Speed. . . . .	75
5.1.4.5 Intake Air Temperature. . . . .	77
5.1.4.6 Intake Air Pressure. . . . .	79
5.1.5 Summary. . . . .	80
5.2 WAVE Models and Chemical Simulations. . . . .	81
5.3 Correlating K with Key Engine Operating Conditions. . . . .	85
5.4 Correlating K with Fundamental Engine Parameters. . . . .	87
5.5 Conclusions. . . . .	89
Chapter 6: Fundamentals of Fuel Sensitivity. . . . .	91
6.1 Properties of Individual Fuel Components. . . . .	91
6.1.1 Chemical Bond Energies. . . . .	91
6.1.2 Molecular Structure of Higher Sensitivity Molecules. . . . .	93
6.1.3 Initial Chemical Structure vs Intermediates. . . . .	94
6.2 Effects of Temperature on Fuel Chemistry. . . . .	95
6.2.1 Engine Models. . . . .	96
6.2.2 Different Combustion Regimes. . . . .	99
6.2.3 Transition Region. . . . .	101
6.3 Chemical Fundamentals. . . . .	106
6.3.1 Hydrogen Peroxide, Hydroperoxy Alkyl Radicals, and Aldehydes. . . . .	106
6.3.2 The Formation of RCHO . . . . .	111
6.4 Conclusions. . . . .	111
Chapter 7: Historic Shifts in K Values. . . . .	113
7.1 Early Values of K. . . . .	113
7.2 1951-1991 CRC Study. . . . .	114
7.2.1 Determining K from Survey Data. . . . .	115
7.2.2 Change in the Maximum Required Octane Number. . . . .	115
7.2.3 Average K Value. . . . .	115
7.2.4 Changes in Engine Technology between 1928 and Present. . . . .	118
7.3 Knock Limits of Historic, Current, and Future SI Engines. . . . .	122
7.3.1 Historic (1951) SI Engine Knock Limited Range. . . . .	122
7.3.2 Modern SI Engine Knock Limited Range. . . . .	123
7.3.3 Future SI Engine Knock Limited Range . . . . .	125
7.3.4 Values of K for Historic, Current, and Future Engines. . . . .	126
7.4 Conclusions. . . . .	127
Chapter 8: Modifications to the Octane Number Tests. . . . .	129
8.1 Changing Reference Fuels. . . . .	129
8.2 Changing the Engine Operating Conditions. . . . .	131
8.3 Benefits of Changing Regulations. . . . .	134
8.4 Conclusions. . . . .	137



Chapter 9: Summary and Conclusion .....	139
Appendix A: The CFR Engine.....	143
Appendix B: MON and RON OF Different Pure Hydrocarbons.....	145
Works Cited.....	147

(this page intentionally left blank)

## LIST OF TABLES

Table 1.1: The engine operating conditions for the RON and MON tests . . . . .	23
Table 2.1: Test engine specifications. . . . .	28
Table 3.1: Different instruments used to quantify knock onset . . . . .	38
Table 5.1: Base engine operating conditions. . . . .	66
Table 5.2: Fuel Set 1 – RON96 but varying sensitivity. . . . .	67
Table 5.3: Fuel Set 2 – RON91 but varying sensitivity. . . . .	68
Table 5.4: The intake air conditions for chemical models. . . . .	82
Table 6.1: Bond Dissociation Energies. . . . .	92
Table 8.1: The Research and Motor Toluene Numbers. . . . .	130
Table 8.2: The Research and Motor Toluene Number for PRF96, TRF96, and UTG96 . . . . .	131
Table 8.3: Suggested operating conditions for a modified RON and MON test. . . . .	133
Table 8.4: Engine parameters for an NA and a TC-DI engine . . . . .	135
Table 8.5: Engine parameters that effect octane requirements . . . . .	135
Table 8.6: The increase in efficiency from getting rid of minimum MON requirement . . . . .	137

(this page intentionally left blank)

## LIST OF FIGURES

Figure 1.1: Engine cycle under normal operation. . . . .	19
Figure 1.2: Engine cycle under knocking operation. . . . .	19
Figure 1.3: Image captures from a knocking engine cycle. . . . .	20
Figure 1.4: Commercial fuel pump with posted minimum octane rating. . . . .	23
Figure 1.5: The Increase in RON between 1925 and 1955. . . . .	24
Figure 2.1: Diagrams and picture of the cylinder head used for the experiments. . . . .	28
Figure 2.2: Schematic of engine control systems. . . . .	29
Figure 2.3: Schematic of instruments used to quantify knock intensity. . . . .	29
Figure 2.4: Schematic of the air pathway into the engine. . . . .	31
Figure 2.5: Schematic of the fuel pathway into the engine. . . . .	31
Figure 2.6: WAVE model for the Ricardo-Hydra test engine setup. . . . .	33
Figure 2.7: WAVE model of CFR Engine for RON and MON test. . . . .	33
Figure 2.8: Constant pressure batch reactor. . . . .	34
Figure 2.9: Model used to simulate pressures and temperatures inside of an engine. . . . .	35
Figure 3.1: Different sampling positions for instrumentation. . . . .	39
Figure 3.2: Raw pressure transducer, accelerometer, and microphone data . . . . .	40
Figure 3.3: Pressure trace of knocking cycle and FFT measured from two positions. . . . .	42
Figure 3.4: The different radial and circumferential modes of an engine. . . . .	42
Figure 3.5: Frequency spectrum of accelerometer signals from two positions. . . . .	43
Figure 3.6: Frequency spectrum of microphone signal from two positions. . . . .	44
Figure 3.7: Frequency spectrum for different instrumentation at different engine speeds . . . . .	45
Figure 3.8: Frequency spectrum for different instrumentation at different spark locations . . . . .	45
Figure 4.1: Pressure traces and FFT for knocking and non-knocking engine cycles. . . . .	50
Figure 4.2: The attenuation in pressure oscillations with time. . . . .	51
Figure 4.3: The knock intensity plotted against the spark timing . . . . .	52
Figure 4.4: Percent of cycles with a knock intensity above a certain threshold . . . . .	53
Figure 4.5: The knock intensity plotted against the maximum pressure of the cycle. . . . .	54
Figure 4.6: The autoignition integral plotted against the spark timing. . . . .	55
Figure 4.7: The knock intensity plotted against the autoignition integral for each cycle . . . . .	56
Figure 4.8: The knock intensity plotted against the maximum value of $dp/dt$ . . . . .	57
Figure 4.9: The knock intensity plotted against the mass fraction burned . . . . .	57
Figure 4.10: Pressure trace for a typical cycle for the MON80 test. . . . .	59
Figure 4.11: Frequency spectrum for the MON80 and MON85 tests. . . . .	59
Figure 4.12: Cross section of the modern and CFR engine geometries . . . . .	61
Figure 4.13: Frequency spectrums comparison between MON80 and modern engine knock. . . . .	62

Figure 5.1: The OI plotted against fuel sensitivity. . . . .	69
Figure 5.2: The knock limited spark timing plotted against fuel. . . . .	70
Figure 5.3: Peak pressure plotted against spark timing at the base operating conditions. . . . .	70
Figure 5.4: Knock limited maximum pressure versus fuel sensitivity . . . . .	71
Figure 5.5: K as a function of the spark location. . . . .	72
Figure 5.6: K as a function of compression ratio . . . . .	74
Figure 5.7: K as a function of the air/fuel ratio . . . . .	75
Figure 5.8: K as a function of engine speed . . . . .	76
Figure 5.9: OI versus fuel sensitivity for engine speeds of 1500 rpm and 2000 rpm . . . . .	76
Figure 5.10: K as a function of intake air temperature . . . . .	78
Figure 5.11: OI plotted against fuel sensitivity for different intake air temperatures. . . . .	78
Figure 5.12: K as a function of boosting percentage . . . . .	79
Figure 5.13: OI plotted against fuel sensitivity for intake air pressures . . . . .	80
Figure 5.14: The OI as a function of fuel sensitivity (RON96) at different intake air temperatures, as found through the experiments and chemical models . . . . .	83
Figure 5.15: The OI as a function of fuel sensitivity (RON96) at different intake air pressures, as found through the experiments and chemical models. . . . .	83
Figure 5.16: The OI as a function of fuel sensitivity (RON91) at different intake air temperatures, as found through the experiments and chemical models. . . . .	84
Figure 5.17: The OI as a function of fuel sensitivity (RON91) at different intake air pressures, as found through the experiments and chemical models . . . . .	84
Figure 5.18: Coefficients of the variables in the response surface methodology . . . . .	86
Figure 5.19: Response Surface Methodology curve fit. . . . .	86
Figure 5.20: K plotted against a normalized end-gas temperature. . . . .	88
Figure 6.1: Chemical structures of iso-octane, n-heptane, ethanol, and toluene. . . . .	93
Figure 6.2: Chemical structures of ethane and ethylcyclopropane . . . . .	94
Figure 6.3: The chemical reduction mechanisms for (a) iso-octane and (b) n-heptane. . . . .	95
Figure 6.4: End-gas temperature plotted against CAD for different engine intake air temperatures with no chemical heat release. . . . .	97
Figure 6.5: End-gas temperature plotted against CAD for different engine intake air temperatures with chemical heat release for PRF96 . . . . .	98
Figure 6.6: End-gas temperature plotted against CAD for different engine intake air temperatures with chemical heat release for TRF96 . . . . .	98
Figure 6.7: End-gas temperature plotted against CAD for different engine intake air temperatures with chemical heat release for a RON96 ethanol blend . . . . .	99
Figure 6.8: The autoignition delay time as a function of temperature . . . . .	101
Figure 6.9: $d(\ln \tau)/d(1/T)$ plotted against temperature for fuels of varying S . . . . .	102

Figure 6.10: $d(\ln \tau)/d(1/T)$ plotted against temperature for PRF96 at varying pressures . . . .	103
Figure 6.11: The autoignition integral as a function of end-gas temperature in the RON96 test for a non-sensitive and a sensitive RON96 fuel . . . . .	104
Figure 6.12: The end-gas temperature spectrum for engine operations . . . . .	105
Figure 6.13: This flowchart shows how a stronger temperature dependence on the autoignition delay time in the transition region results a higher sensitivity. . . . .	105
Figure 6.14: The amount of hydrogen peroxide ( $H_2O_2$ ) required for a thermal explosion at different initial temperatures . . . . .	107
Figure 6.15: The maximum amount of $RO_2$ produced as an intermediate at different temperatures for different sensitivity of fuels . . . . .	108
Figure 6.16: The maximum amount of $C_2H_4$ produced as an intermediate at different temperatures for different sensitivity of fuels . . . . .	108
Figure 6.17: The maximum amount of $RCHO$ produced as an intermediate at different temperatures for different sensitivity of fuels. . . . .	109
Figure 6.18: The autoignition delay time for aldehydes as a function of temperature . . . . .	110
Figure 7.1: The required fuel octane number from 1951 to 1991. . . . .	116
Figure 7.2: The average value of K in 1951, 1961, 1971, 1981, and 1991. . . . .	117
Figure 7.3: The average value of K at each engine speed for 1951 to 1991. . . . .	117
Figure 7.4: The percentage of CRC engine tests with negative values of K. . . . .	118
Figure 7.5: The average displaced volume and compression ratios in 1951-1991. . . . .	120
Figure 7.6: Engine breathing technology in 1991. . . . .	121
Figure 7.7: Engine valve and fuel injection technology between 1985 and 1999. . . . .	121
Figure 7.8: WAVE Model for a 1951 engine and the corresponding engine map. . . . .	123
Figure 7.9: WAVE Model for a 2008 engine and the corresponding engine map. . . . .	124
Figure 7.10: WAVE Model for a future TC-DI engine and the corresponding engine map. . .	126
Figure 7.11: The statistical distribution of K values for a historic, current, and future engine. .	127
Figure 7.12: The average value of K as a function of the year, found from literature, the CRC surveys, and WAVE Models. . . . .	128
Figure 8.1: RON and MON of TRFs as a function of the percentage of n-heptane. . . . .	130
Figure 8.2: The statistical distribution of K values for current and future engines based off WAVE models . . . . .	132
Figure 8.3: The knock limited maximum pressure plotted against the average of a modified RON and the MON tests . . . . .	134
Figure A.1: The CFR Engine. . . . .	143
Figure B.1: RON and MON of different pure hydrocarbons. . . . .	145

(this page intentionally left blank)



## CHAPTER 1: INTRODUCTION

### 1.1 OVERVIEW OF KNOCK

Spark ignition (SI) engines currently power the majority of the 250 million automobiles in the US [1]. Though alternatives, such as fuel cells and advanced batteries, are becoming available, the SI engine is still posed to be the primary means of powering both consumer and commercial vehicles, especially in rapid-growing emerging markets [2]. Therefore, it is imperative that the field of ICE technology be further advanced. Since the maximum efficiency of an engine is limited by an engine phenomenon termed knock, advancing the knock limits is crucial towards advancing ICE technology.

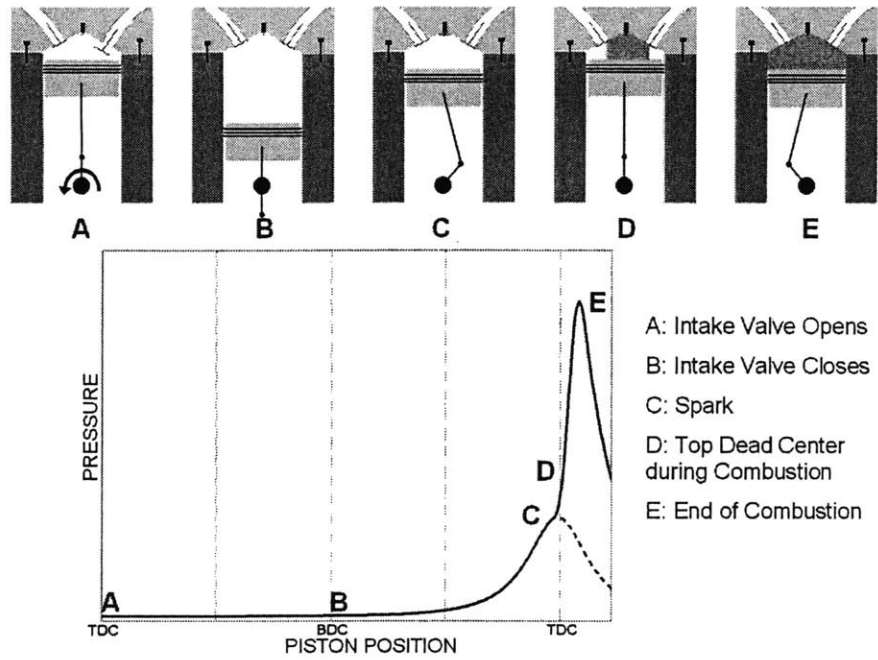
The term knock refers to the engine noise that accompanies the rapid autoignition of unburned fuel and air as the flame propagates across the chamber [3]. Figures 1.1 and 1.2 illustrate the difference between a normal engine cycle and a knocking engine cycle. In Figure 1.1, the intake valve opens at step A, allowing for fuel and air to enter into the cylinder. The downward movement of the piston draws the intake mixture through the open intake valve into the cylinder. The intake valve then closes at step B, trapping the fuel and air into the cylinder. The piston then begins to move upwards, compressing the mixture. Since the volume of the cylinder is decreasing, the in-cylinder pressure increases, and this process is often approximated as adiabatic compression. The combustion process is initiated at step C with a spark from the spark plug creating a flame kernel. The flame propagates across the chamber, increasing the pressure, from step C to step D. In Figure 1.1, the end of combustion occurs at E, and the flame is quenched on the cylinder walls. The pressure increase due to combustion pushes the piston down and generates work.

The knocking cycle, displayed in Figure 1.2, follows the same process as the normal cycle from step A to step D. However, as the cylinder pressure increases, the temperature of the end-gas, the unburned fuel and air ahead of the flame front, increases. At step E, the end-gas pressures and temperatures are high enough that the end-gas autoignites. The autoignition process is

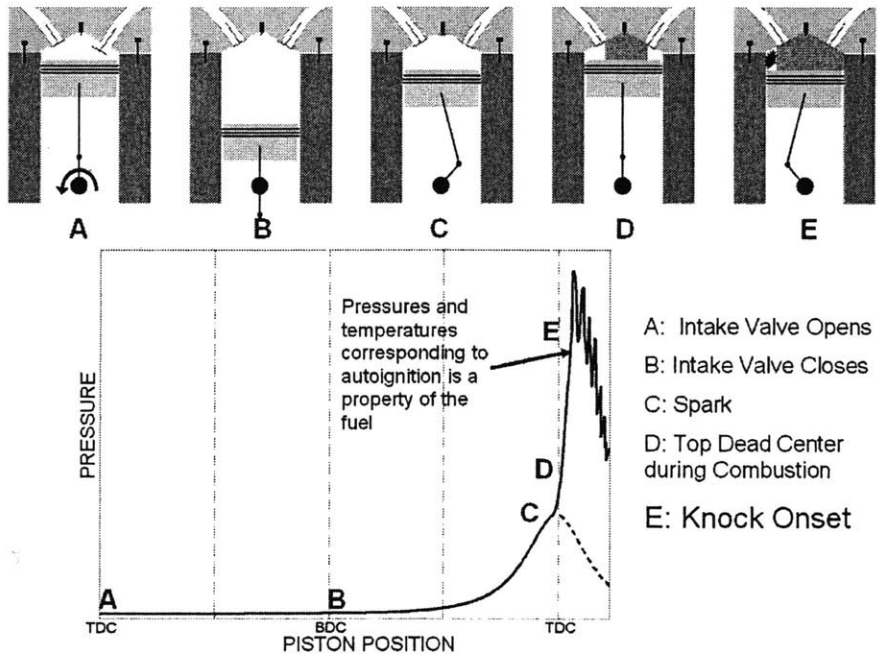
sufficiently rapid that the pressure in the autoigniting region rises faster than expansion of that region can accommodate. Thus the energy release manifests itself through a pressure rise followed by pressure oscillations at the resonant frequencies of the combustion chamber. These pressure oscillations cause the engine block to vibrate, which in turn generates engine noise, causing the engine to emit a knocking sound [4].

Figure 1.3 shows in-cylinder images from a high speed video of knock onset. This video, taken from a study by Konig and Shepherd [5], recorded the light emission from the high temperature burned gases, such that the intensity increases with increasing gas temperature. Frame 1 shows the flame moving to the left with the dark crescent-shaped end-gas region ahead of it, prior to any autoignition. Frame 2 shows the first autoigniting region in the end-gas, at the lower left of the frame. In frame 3, additional autoigniting hot spots are apparent, especially a region in the lower right corner of the end-gas crescent. This process continues into frame 4, where most of the end-gas has autoignited. The entire process is rapid; the time difference between frames 1 and 4 corresponds to 2 CAD.

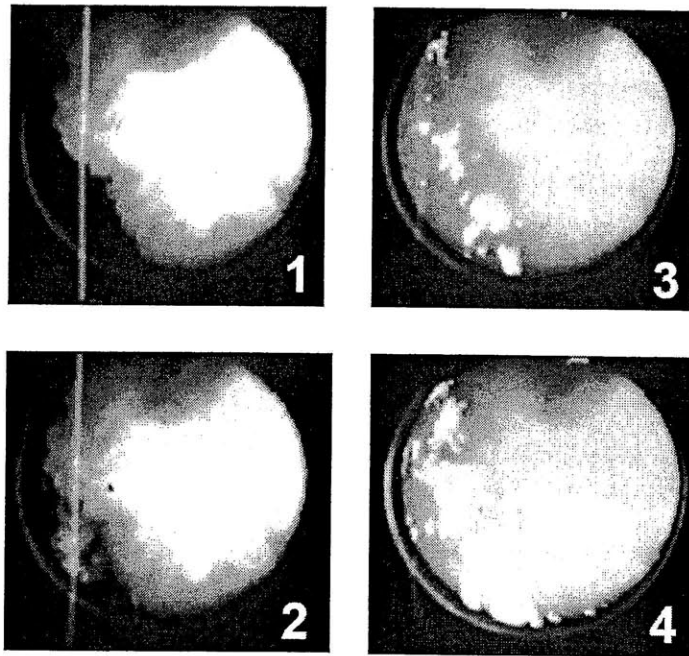
Heavier knock can be an indication that engine damage is occurring. For example, in World War I, airplane engines would knock heavily enough to destroy the pistons [6]. However, for the most part, knock in modern engines is simply considered a noise irritant [3]. Due to the noise and possible engine damage, engine manufacturers design engines to avoid knock, limiting the maximum allowable pressures and temperatures in the engines. These limits set the maximum compression ratio, which in turn sets the maximum possible engine efficiency. For example, the Model T only had a compression ratio of 4.5 in order to avoid knock [7]. Knock also limits the amount of boosting, which allows an engine to be downsized, decreasing the heat transfer and friction losses. Additionally, in modern cars, at low speeds and high loads, when knock is an issue, the spark timing is significantly retarded to decrease the maximum in-cylinder pressure hence avoiding knock. However, retarding the spark timing penalizes the efficiency and performance of the engine.



**Figure 1.1: Engine cycle under normal operation: (A) intake, (B) start of compression, (C) spark, (D) part burn, (E) end of combustion.**



**Figure 1.2: Engine cycle under knocking operation: (A) intake, (B) start of compression, (C) spark, (D) part burn, (E) knock onset.**



**Figure 1.3: Image captures from a high speed video of a knocking engine cycle [5]. The video recorded the light emission from the high temperature burned gases, and the intensity increases with increasing gas temperature. Autoignition occurs in Frame 2.**

The knock limits have been advanced through developments in both engine and fuel technology. On the engine side, engine geometries were modified in order to foster a faster burn rate. A faster burn rate gives less time for autoignition to occur during the combustion process. Early engines had little turbulence and sparked from the side, resulting in it taking the flame a long time to propagate across the chamber [3]. The burn time was further decreased by adding turbulence and by moving the spark plug to the center.

On the fuel side, different refining techniques and fuel additives have been developed to decrease a fuel's propensity to autoignite. For example, the addition of tetra-ethyl lead into fuel and the invention of catalytic cracking changed the fuel chemistry and allowed fuels to operate at higher pressures without knocking. Tetra-ethyl lead was found to poison the catalytic converter, and hence was phased out of fuels and replaced with other anti-knock additives, such as methyl tertiary butyl ether and ethanol.

## 1.2 THE OCTANE SCALE

Since knock can be avoided by using a fuel less prone to autoignite, it is necessary to quantify the antiknock properties of a fuel. The first metric to quantify the antiknock properties of a fuel was the highest useful compression ratio (HUCR), the maximum compression ratio that a fuel could operate at without knocking in a Ricardo test engine. The HUCR definition was unpopular because it was considered too abstract. On the other hand, reference fuels were considered less abstract, though they added complexity and uncertainty. Consequently, “Utopia (HUCR) gave way to the Babel of individual reference fuels, [8]” with the development of the octane index (OI).

The concept behind the OI is that a fuel’s complex autoignition chemistry can be compared to a much simpler binary fuel blend [9]. The binary blend used in these comparisons is the primary reference fuel (PRF), a blend of iso-octane and n-heptane.\* Due to its chemical structure, iso-octane is not prone to autoignite; however, n-heptane is very likely to autoignite even at low temperatures and pressures. Therefore, as the percentage of iso-octane increases in the blend, the fuel mixture is less likely to autoignite. The OI of a fuel is the volumetric percentage of iso-octane in the PRF that knocks at the same intensity at the same conditions.

The OI of a fuel changes depending on the engine operating conditions. For example, at condition 1, a fuel might behave similar to PRF96 (96 percent iso-octane and 4 percent n-heptane) and have an OI of 96. However, at condition 2, that same fuel might behave like PRF87 (87 percent iso-octane and 13 percent n-heptane) and have an OI of 87. Hence, the engine operation conditions must be standardized to allow for a proper comparison of fuels.

For fuel rating purposes, the OI is measured in the Research and Motor Octane Number (RON and MON) tests. The standards for the RON test are given in ASTM 2699 [10], and the standards for the MON test are in ASTM 2700 [11]. The tests are done in a Cooperative Fuel

---

\* The naming convention for a PRF: PRF X is a blend of X percent iso-octane and (100-X) percent n-heptane. For example, PRF96 would be a volumetric blend of 96 percent iso-octane and 4 percent n-heptane.

Research (CFR) engine which has a variable compression ratio. The inlet conditions and speed for the engine are fixed, and the compression ratio is increased until the engine knocks at a given intensity, measured by a pressure transducer. The procedure is then repeated for different PRFs until a PRF is found that knocks at the same intensity at the same compression ratio. The RON or MON of the fuel is the OI measured in the respective test.

The RON and MON tests operate at the conditions shown in Table 1.1. The two main differences between the RON and MON tests are engine speed and intake air temperature. The intake air temperature for the RON test is 52°C, which is at the upper limit for the intake air temperature of modern engines. The MON intake air temperature is 149°C, over 100°C hotter than modern engines. Additionally, 600 and 900 rpm is low for the engine speed. Most modern cars cannot run at peak load until 1200 RPM.

Since the OI depends on the operating conditions, most fuels have different RON and MON values. Typically, the RON is higher than the MON for a given fuel. The difference between the resulting RON and MON is termed the fuel's sensitivity:

$$S = \text{Sensitivity} = RON - MON \quad (\text{Eq 1.1})$$

Different fuels have different sensitivities. For example, a PRF has a sensitivity of 0. Meanwhile, most commercial gasolines have a sensitivity of 8. Leaded fuels can have sensitivities over 30. [9]

The RON and MON are simply the OI of a fuel at two fixed conditions. The OI at any condition can be interpolated from the RON and MON of the fuel using a weighing factor, K:

$$OI = (1 - K)RON + K MON \quad (\text{Eq 1.2})$$

K is assumed to be independent of the fuel, depending only on the operating condition [12, 13]. It should be noted that K = 0 corresponds to the RON test, and K = 1 corresponds to the MON test. If K is less than 0 or greater than 1, the OI is extrapolated from the RON and MON values.

When the tests were established in the 1930s, it was believed that the value of K was 1, corresponding to the MON [9]. The value of K shifted downwards and eventually a value of K = 0.5 was used to capture a fuel's "on the road" octane number. The OI at K = 0.5 is posted on

retail gasoline dispensers in the United States as shown in Figure 1.4. Kalghatgi performed tests in 2001 to determine a more accurate value of K. These tests show that K is seldom equal to 0.5. In fact, K is often negative at many engine operating conditions [12].

	RON	MON
INLET TEMPERATURE	52°C	149°C
INLET PRESSURE	ATMOSPHERIC	ATMOSPHERIC
COOLANT TEMPERATURE	100°C	100°C
ENGINE SPEED	600 RPM	900 RPM
SPARK TIMING	13° BTC	14-26° BTC
COMPRESSION RATIO	4 - 18	4 - 18

Table 1.1: The engine operating conditions for the Research and Motor Octane Number (RON and MON) tests [10], [11].



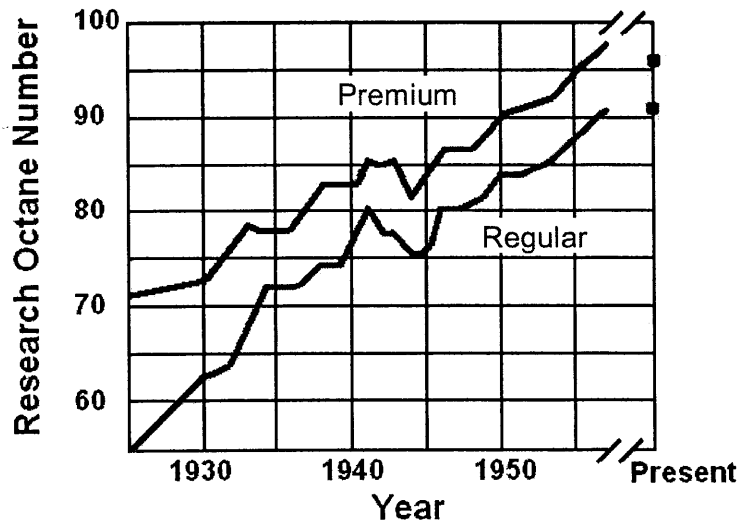
Figure 1.4: Commercial fuel pump in the United States with posted minimum octane rating. The octane rating corresponds to  $K = 0.5$ .

### 1.3 MODERN ENGINE TRENDS AND KNOCK

A century after the invention of the spark ignition engine, knock continues to be the major engine design constraint. Most cars will only knock at high loads and low speeds which occur over a small percentage of the drive cycle. These conditions are important for towing heavy loads, driving up steep inclines, and accelerating from a standstill (e.g. the 0-60 mph acceleration). However, good performance in these conditions is crucial to marketability.

Current engine trends show that engines are moving towards higher peak operating pressures due to increases in the engine compression ratio, the use of variable valve timing, and boosting. The average compression ratio in 2008 is 9.8, with a maximum value of 12.3 [14]. Variable valve timing allow for the valve opening and closing times to change to minimize the pressure drop across the valve, hence increasing the in-cylinder pressure at intake valve closing. Boosting includes both supercharging and turbocharging which increase the intake air pressure by extracting work from the crankshaft and from the exhaust respectively. It should be noted that small changes in the intake air pressure can results in large changes in the peak pressure due to the compression being approximately polytropic.

Engine boosting is typically coupled to downsizing the engine. The amount of work produced by the engine is approximately proportional to the mass of air that enters into the cylinder. Therefore, when an engine is boosted, the cylinder volume can be decreased and produce the same power. A major benefit of boosting and downsizing the engine is that the smaller engine has less friction and heat transfer losses.



**Figure 1.5: The Research Octane Number of regular (red) and premium (blue) fuels between 1925 and 1955. The number steadily increases until 1955, when it levels off to its present-day levels [7].**



Figure 1.5 shows the change in the RON for regular and premium fuels from 1930 to 1955. When the RON test was established, regular fuel had a RON of 60, and premium fuel had a RON of 72 [7]. High octane automotive fuels were seen as a niche market for race cars and aircraft. The development of catalytic cracking in World War II allowed for the widespread use of high octane fuels, and by 1955, the RON of regular and premium fuels reached their current levels of 91 and 96 respectively [15]. Post-war automobiles were made with higher compression ratios to take advantage of these high octane fuels.

Since the RON of fuels has not changed significantly in the last 50 years, the advancement in antiknock technology has come from developments on the engine side. Knock sensors have become the primary tool for combating knock. Knock sensors work by measuring the engine block vibrations associated with knock; the spark timing is retarded lowering the engine's peak pressure until the engine stops knocking.

The temperatures in engines have also been decreasing, further advancing the knock limits. Older engines used carburetors for fuel delivery; carburetors required heating the intake air to facilitate fuel vaporization. Carburetors have been replaced with fuel injectors, which do not require intake air heating. Direct injection, a more advanced form of fuel metering, further reduces the intake air temperature through the use of charge cooling. Also, advances in engine cooling technology have eliminated hot spots and lowered the temperatures of the cylinder walls, in turn lowering the in-cylinder fuel and air temperatures. With lower end-gas temperatures, an engine can operate at higher pressures without knocking.

#### **1.4 GOALS OF STUDY**

In 1961, Earl Bartholomew, a chief engineer at the Ethyl Corporation, stated, "It is remarkable that the Research and Motor Octane Number test methods, developed almost thirty years ago, are still in use [9]." His study found that the tests were out of date and did not accurately relate to engines in 1961. Almost 50 years later, the RON and MON tests are still in use with only trivial changes to characterize the antiknock properties of fuels.

This study sets out to evaluate the relevancy of the RON and MON tests for modern engines.

This investigation consisted of four parts:

- 1) Compare the physics of knock in the octane tests to that of modern engines
- 2) Determine what parameters govern K in the equation  $OI = RON - KS$
- 3) Investigate the chemical fundamentals of fuel sensitivity
- 4) Determine possible modifications to the RON and/or MON tests

Parts 1, 2, and 3 address attempt to evaluate the RON and MON tests at a fundamental level.

Part 4 then uses this fundamental understanding to look at possible modifications.

Part 1 will focus on:

- Investigating the different metrics employed for measuring knock (Chapter 3)
- Experimentally studying different phenomena that govern knock onset in both modern engines and the CFR engines (Chapter 4)

Parts 2 and 3 will involve:

- Experimentally measuring the OI over a range of conditions for different fuels (Chapter 5)
- Determining what parameters govern K (Chapter 5)
- Relating K to the engine operating conditions (Chapter 5)
- Using chemical modeling to develop a fundamental understanding of S (Chapter 6)
- Analyze the historic shift in K values (Chapter 7)

Part 4 will include:

- Evaluate the possibilities of using different reference fuels (Chapter 8)
- Suggest different RON/MON test conditions (Chapter 8)

## CHAPTER 2 EXPERIMENTAL APPARATUS AND MODELING TOOLS

Experiments and computer models were used to develop a better understanding on the physics and chemistry of knock in modern engines and in the octane tests. The experiments were performed in a single cylinder test engine. The computer models involved engine simulations and chemical kinetic models.

### 2.1 ENGINE SETUP

#### 2.1.1 TEST ENGINE AND INSTRUMENTATION

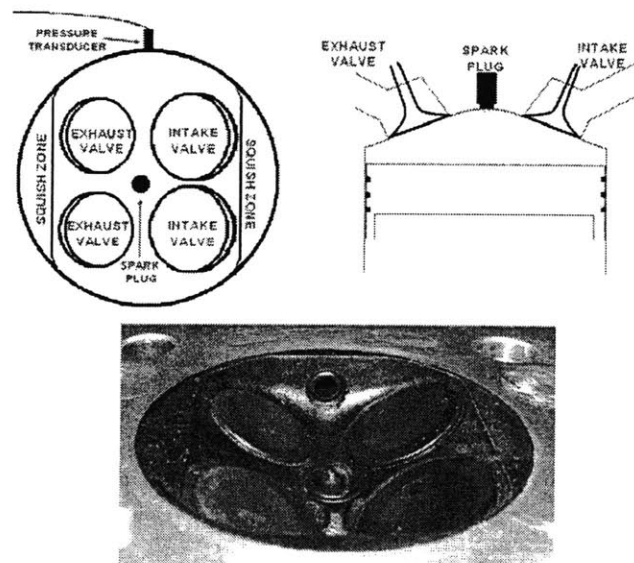
The experimental setup consists of a single-cylinder test engine, a variable speed dynamometer, and various control and test equipment. The engine used for the experiments has a Ricardo MK III base with a Volvo B5254 pent-roof, 4-valve, central spark plug cylinder head. At MBT timing, WOT, and at stoichiometric conditions, the engine has a NIMEP of approximately 10.2 bar. Other engine specifications are given in Table 2.1. Table 2.1 gives that the compression ratio of the engine is 9.8 which is the average compression ratio for a 2008 SI Engine [14]. Additionally, the valve timings and other specifications are similar to those of most modern engines. Figure 2.1 shows a photograph of the cylinder head. It identifies the center spark plug location and the location of the pressure transducer relative to the intake and exhaust valves. Not visible in Figure 2.1 is a second spark plug hole that was added opposite to the pressure transducer tapping. The second spark plug hole was added in order to change the spark location.

A schematic of the engine control systems is shown in Figure 2.2. This engine is connected via a drive shaft to an Eaton Dynamatic AF-6360 50hp dynamometer, which is controlled by an Eaton Dynamatic Adjustable Frequency Drive. This motor and drive combination is able to both motor the engine as well as absorb power when the engine was fired. The system automatically adjusts the torque output to maintain a constant speed. A MOTEC M4 engine controller controls the injector and ignition system. The injection timing is set to 385° BTC, and the dwell is set to 6 ms. The injector pulse width and spark timing can be adjusted while the engine is running. A

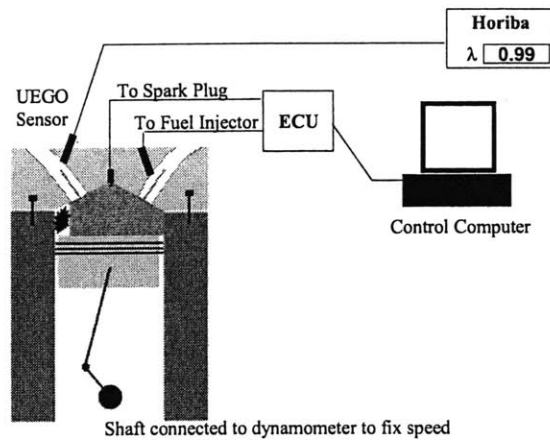
Universal Exhaust Gas Oxygen (UEGO) sensor was used to measure exhaust gas oxygen content. The UEGO sensor reading was then converted to an air-fuel equivalence ratio with the use of a Horiba Mexa-110λ analyzer.

Bore	83 mm
Stroke	90 mm
Connecting Rod Length	158 mm
Displaced Volume	487 cm <sup>3</sup>
Clearance Volume	55 cm <sup>3</sup>
Compression Ratio	9.8:1
Intake Valve Opening	0° BTC
Intake Valve Closing	60° ABC
Exhaust Valve Opening	48° BBC
Exhaust Valve Closing	12° ATC

**Table 2.1: Specifications for the engine used for this experiment**

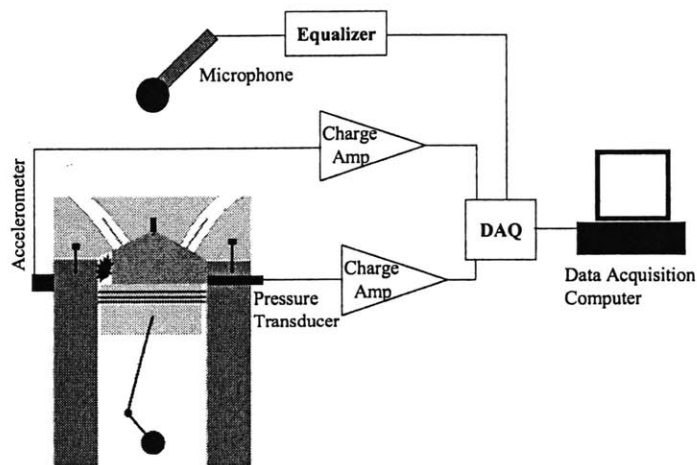


**Figure 2.1: Diagrams and picture of the pent-roof, central spark cylinder head used for the experiments**



**Figure 2.2: Schematic of engine control systems.**

Since knock is a combination of pressure waves, engine block vibrations, and audible noise, different instruments can be used to determine knock onset and knock intensity. Three different instruments—a pressure transducer, an accelerometer, and a microphone—were mounted on the engine setup, as shown in Figure 2.3, to measure and quantify knock.



**Figure 2.3: Schematic of instruments used to measure knock onset and quantify knock intensity.**

The cylinder pressure was measured using a Kistler 6125A piezoelectric pressure transducer with a flame arrester. The transducer is located on the side of the cylinder head, between the intake

and exhaust ports. The transducer was mounted such that its face was perfectly flush with the chamber wall. The current signal from this pressure transducer is converted to a voltage signal with the use of a charge amplifier.

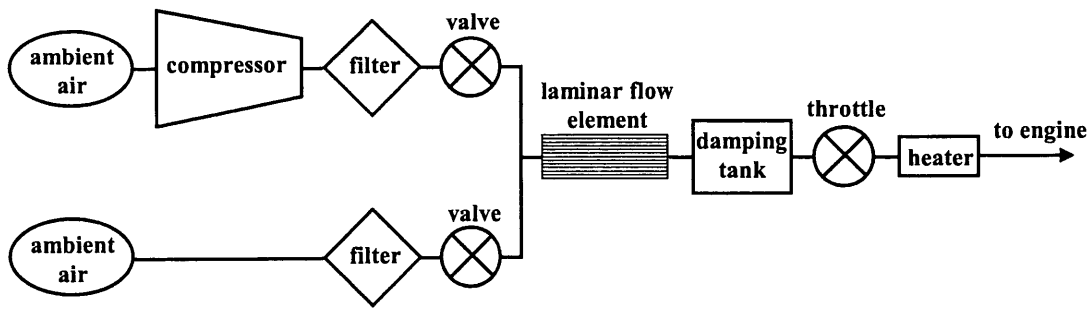
A microphone-based audible knock method was used to detect audible knock onset. The microphone was connected to an equalizer set to attenuate all frequencies except those near 6 kHz and 12 kHz. The audio signal is then passed to a set of headphones where the operator listens to the signal in order to detect knocking conditions. A raw signal bypasses the equalizer such that a non-filtered signal can be logged.

Engine block vibrations were measured by an Endevco 7259B isotron accelerometer. The accelerometer was mounted onto the engine block in line with the head bolts; this position corresponds to the location where commercial knock sensors are mounted. The 7259B model was selected because of the flat frequency response between 20 Hz and 40 kHz. The current signal from the accelerometer is converted to a voltage signal by a charge amplifier.

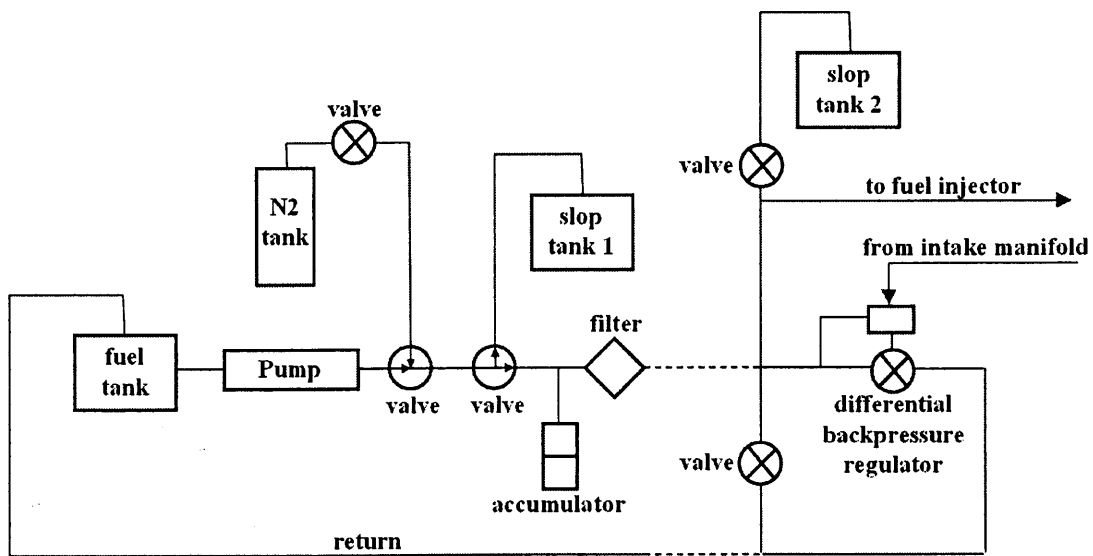
The voltage signals from the pressure transducer, accelerometer, and microphone (pre-filtered) are then collected at a rate of ten samples per crank angle degree using a National Instruments 6023E data acquisition card. Due to the limited size of the memory buffer, only 300 cycles of data, collected at a high sampling frequency, could be logged per run.

### **2.1.2 AIR AND FUEL SYSTEMS**

The engine intake air can be delivered from either ambient or a compressor, as shown in Figure 2.4. In the ambient configuration, the air is directly drawn through a filter positioned in the test cell. To allow for boosting, the intake air can be drawn from a compressor located in a separate test cell; this air is then filtered and regulated by the throttle to the desired engine intake air pressure. In both configurations, the air goes through a laminar flow element and a pulsation damping tank. The temperature of the intake air can be increased using a tape heater wrapped around the intake air line.



**Figure 2.4: Schematic of the two paths that air can take before entering the engine. The top pathway goes through a compressor and is used for boosting. The bottom pathway is used for natural aspirated operation.**



**Figure 2.5: Schematic of the fueling system. This system was used to allow for the rapid changeover of fuels.**

A schematic of the fuel system is given in Figure 2.5. At normal operating conditions, the fuel is pumped from the fuel tank through a filter to the fuel injector. A regulator maintains the pressure in the line leading to the injector at 3 bar above the average intake air pressure. This regulator returns excess fuel to the fuel tank. The fuel system was designed to allow for a rapid change-over of fuels by changing the fuel tanks. A purging system pumps nitrogen through the fuel lines to remove residual fuel, except for the small volumes of the accumulator, the regulator,

and the injector supply line. These residual fuel amounts are reduced by purging multiple times and motoring the engine with the injectors in operation.

## 2.2 WAVE MODELS

Ricardo's WAVE is an engine simulation package that "provides a fully integrated treatment of time-dependent fluid dynamics and thermodynamics by means of a one-dimensional formulation. This incorporates the general treatment of working fluids including air, air-hydrocarbon mixtures, combustion products, liquid fuels, and Freon gases [16]." The software does not have models for chemical kinetics; the combustion characteristics are specified through the user entering a burn profile. However, WAVE does include many tables and correlations for determining the emissions and losses incurred over a range of engine operating conditions.

A WAVE model was generated for the engine setup described in the previous section and is shown in Figure 2.6. The engine cylinder is the orange circle located in the center of the figure. To the left of the engine cylinder is the intake manifold and the connected plumbing, and the exhaust manifold and the accompanying plumbing are located to the right. The intake air is boosted and heated by varying the ambient air conditions located at the far left. The burn rate for the engine cycles was determined from experimental data, using a modified burn rate analysis code developed by [17]. The model was validated by comparing the peak pressures predicted by the models to experimentally-measured values.

A less complex WAVE model was created for the CFR engines based on the engine specifications from the ASTM standards [10,11]. The CFR engine is similar for both the RON and MON tests, except for the specifications given in Table 1.1 and the size of the carburetor orifice. The schematic of this model is shown in Figure 2.7. It should be noted that the CFR engines are carbureted, but WAVE does not include a carburetor model. The carburetor is modeled as an injector with heat fuel connected to an orifice. The peak pressure and endgas temperatures were validated against values in literature [18].



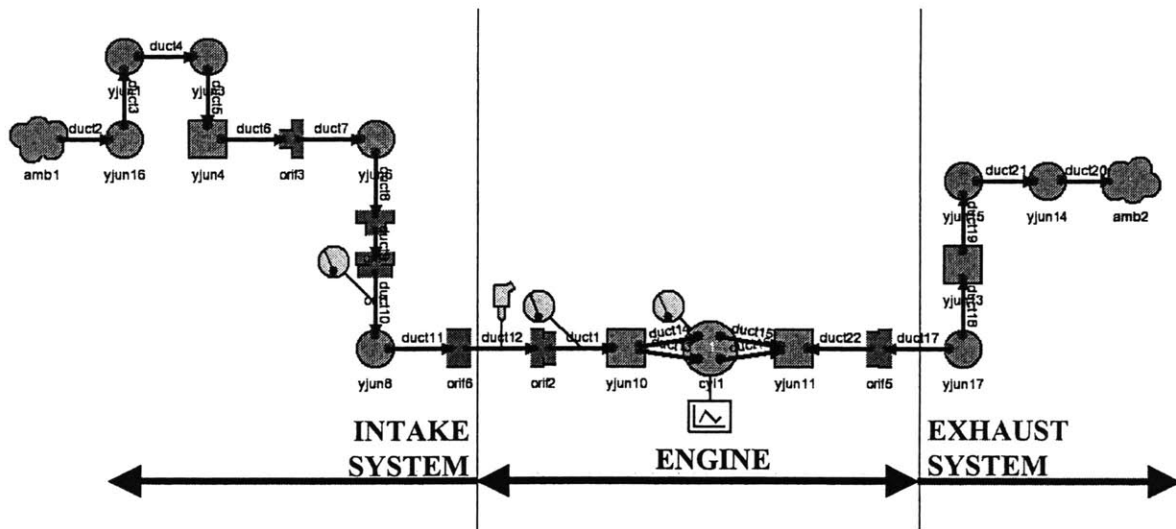


Figure 2.6: WAVE model for the Ricardo-Hydra test engine setup.

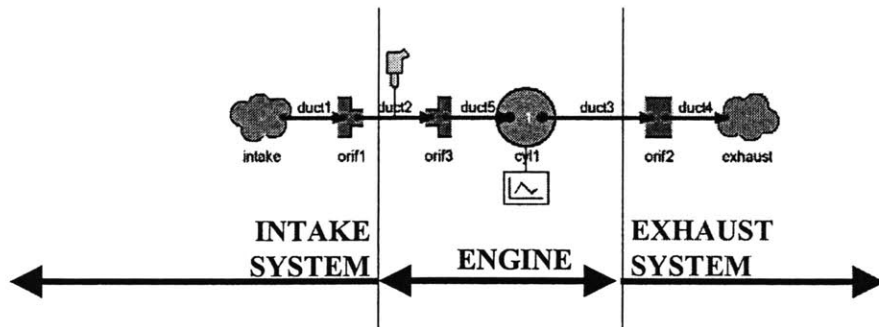


Figure 2.7: WAVE model of CFR Engine for RON and MON test

Additional WAVE models were used in Chapter 7 to model current, past, and future engines. These models are addressed in their respective sections.

### 2.3 CHEMICAL MODELS

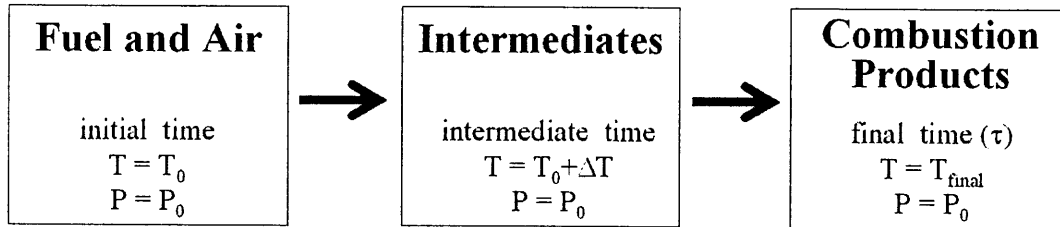
Chemical kinetic models can be used to analyze the chemistry of autoignition at different thermodynamic conditions. These models are useful in characterizing autoignition in terms of an autoignition delay time and by the chemical intermediates. The autoignition delay time is the

induction time required for a fuel and air mixture to react and autoignite. Generally, the autoignition delay time ( $\tau$ ) can be approximated to have the form:

$$\tau = c_1 p^{-c_2} \exp\left(\frac{c_3}{T}\right) \quad (\text{Eq. 4.1})$$

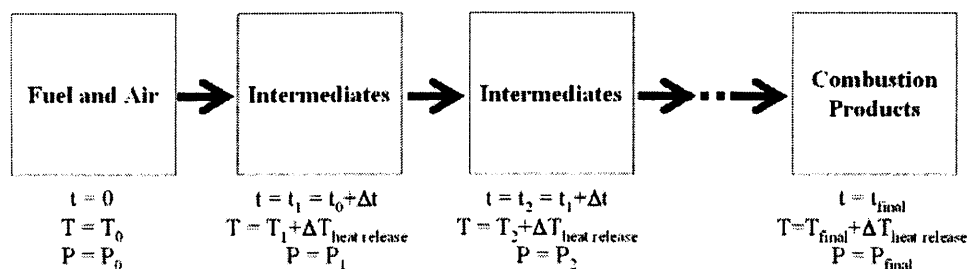
such that the value of  $\tau$  decreases as pressure and temperature increase.

The value of  $\tau$  for a fuel and air mixture at a given temperature and pressure can be determined by the constant pressure batch reactor model shown in Figure 2.8. The perfectly mixed fuel and air mixture is held at a constant pressure in the reactor, and the amount of time required for autoignition (i.e. the autoignition delay time) is measured. Though the initial temperature is fixed, the temperature is allowed to rise due to chemical heat release.



**Figure 2.8: Constant pressure batch reactor. The temperature is free to increase with chemical heat release, but the pressure remains fixed.**

The constant pressure batch reactor can be modified to be more representative of the conditions seen by the end-gas in an engine. First, a pressure and adiabatic end-gas temperature trace from a WAVE model is discretized into small finite time steps. A constant pressure batch reactor is then run for the first time step at the initial temperature and pressure. The products at the end of the time step become the reactants for the next time step. The initial temperature of the next time step includes the temperature increase from both compression and the chemical heat release. The reactor is then set to run again with this concentration and temperature at the pressure of the next time step. This process repeats until autoignition occurs, as shown in Figure 2.9.



**Figure 2.9: Model used to simulate changing pressures and temperatures inside of an engine. At each time step, the pressure and temperature are increased.**

Different sets of chemical kinetic mechanisms were used to look at the autoignition of different fuel blends. The fuel blends used in this thesis were composed of iso-octane, n-heptane, toluene, and ethanol; these chemicals are described in detail in Chapter 6. The first mechanism is the reduced chemical kinetic mechanism for iso-octane and n-heptane, developed by Tanaka [19]. This mechanism has 67 reactions with 32 species. The reduced mechanism was used to look at larger trends and to validate the modeling code. The second mechanism is the detailed chemical kinetic mechanism developed by Andrae [20] to look at the autoignition of iso-octane, n-heptane, and toluene blends. This mechanism was merged with the mechanism developed by Marinov [21] for ethanol, to produce a mechanism with 4465 reactions and 1050 species. The final mechanism was developed by Sakai [22] and looks at the chemistry of iso-octane, n-heptane, toluene, and ethanol. This mechanism contains 2877 reactions and 807 species.

Both detailed mechanisms, the combined Andrae/Marinov mechanism and the Sakai mechanism, gave similar results. However, the ethanol blend results from the Sakai mechanism matched the experimental mechanisms better. Since the Andrae/Marinov mechanism was the combination of two mechanisms, the mechanism does not include the cross-reactions between the intermediates of the ethanol combustion and the products of the iso-octane, n-heptane, and toluene combustion. Therefore, for the chemical analysis in this study, the Sakai mechanism was used.

(this page intentionally left blank)

## CHAPTER 3: EVALUATION OF DIFFERENT KNOCK METRICS

A proper characterization of knock onset requires that a knock metric must be properly defined. Several different metrics can be used to quantify knock, and these metrics are evaluated and compared.

### 3.1 COMMONLY USED KNOCK METRICS

Since knock is caused by the coupling between pressure oscillations, block vibrations, and noise, there are several different metrics that are used to measure knock onset and to quantify knock intensity. These metrics, with their advantages and disadvantages, are listed in Table 3.1. The most fundamental tool for quantifying knock is the in-cylinder pressure transducer. In-cylinder pressure transducers measure the initial pressure rise and the pressure oscillations due to the autoignition of fuels. Though very accurate, pressure transducers are expensive and are often difficult to mount due to the coolant passages surrounding the cylinder. A less intrusive tool for quantifying knock is an accelerometer mounted to the engine block. Accelerometers measure the block vibrations associated with knock and tend to be inexpensive. Perhaps the most important and oldest metric for quantifying knock is audible noise. To remove the slightly arbitrary nature of quantifying knock audibly, microphones can be placed around an engine to record the sounds. These recordings can be processed to get numerical values for the knock intensity. [23]

All three metrics are commonplace in modern automobiles. Due to its fundamental nature, the in-cylinder pressure is used in most research studies. However, due to the price, they cannot be implemented in on-the-road engines. The accelerometer, which is much cheaper, is used as the knock sensor in modern engines. When the accelerometer measures engine vibrations at a certain frequency, the spark timing is retarded to stave off knock. Finally, noise is used to detect knock during engine calibration. [24]

These three metrics are also used in the octane tests. The original octane number tests used a “bouncing pin” which was effectively a low-frequency accelerometer. However, later octane

number tests used pressure transducers with the signals conditioned to correspond to the bouncing-pin [25]. The on-the-road octane tests performed between 1947 and 1996 used audible noise as an indication of knock. [26]

These three metrics—pressure oscillations, block vibrations, and audible noise—are all used to quantify knock in both modern engines and in the octane tests. Therefore, it is necessary to determine how these metrics relate to each other.

Instrument	Advantage	Disadvantage	Usage in Modern Engines
Pressure Transducer	Accurate and fundamental	Expensive and difficult to mount	Characterize knock in most engine studies
Accelerometer	Easy to mount and cheap	Less accurate and not fundamental	To determine knock onset (knock sensors)
Microphone (audible noise)	Cheap	Arbitrary	To determine knock onset (engine calibration)

**Table 3.1: Different instruments used to quantify knock onset**

### 3.2 EXPERIMENTAL PROCEDURE

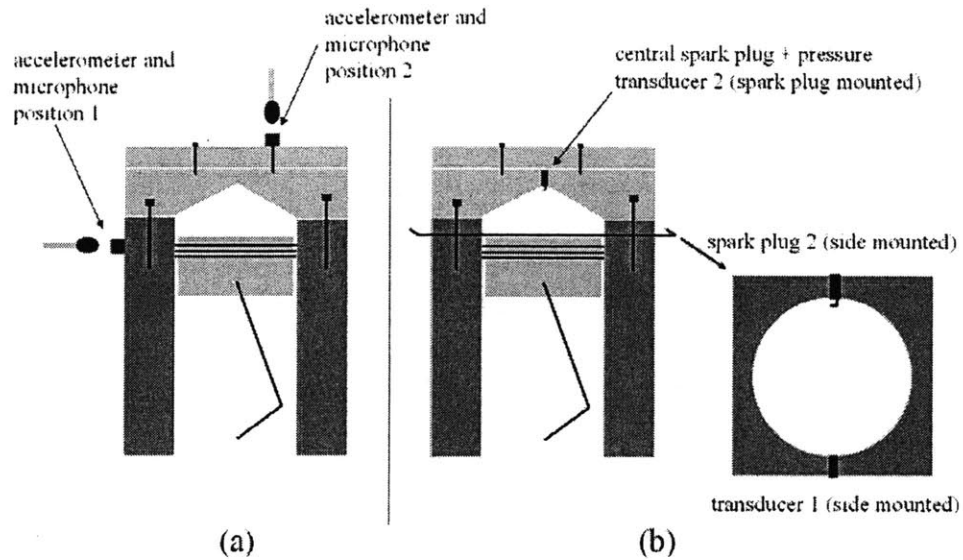
The engine detailed in Chapter 2 was slightly modified to allow for the moving of the different instruments as shown in Figure 3.1. A second accelerometer mounting hole was added to the top of the valve cover to allow for the measurement of engine block vibrations at two different locations. A second pressure transducer was added to the engine, allowing for synchronized pressure measured from transducers at two different locations. The second transducer, a Kistler 6117 piezoelectric pressure transducer, was located in a specialty spark plug. The sparking mechanism was moved to the side, allowing room for a pressure transducer to be mounted completely flush with the spark plug tip.

The engine was set to run at a base condition of stoichiometric, WOT, unheated (intake air temperature = 30°C), and at 1500 rpm with UTG91\*. At this base condition, the spark plug was

---

\* UTG91 is an unleaded test gasoline produced by Chevron Phillips Chemical Company LLC. It has a RON of 91 and a MON of 83. It is a standardized test fuel that is representative of commercial regular-grade gasoline.

located at the apex of the pent-roof. This test condition was chosen to be representative of a typical knocking condition for a modern naturally aspirated SI engine.



**Figure 3.1: Different sampling positions for different instruments for detecting knock onset: (a) microphone, accelerometer, and (b) pressure transducer.**

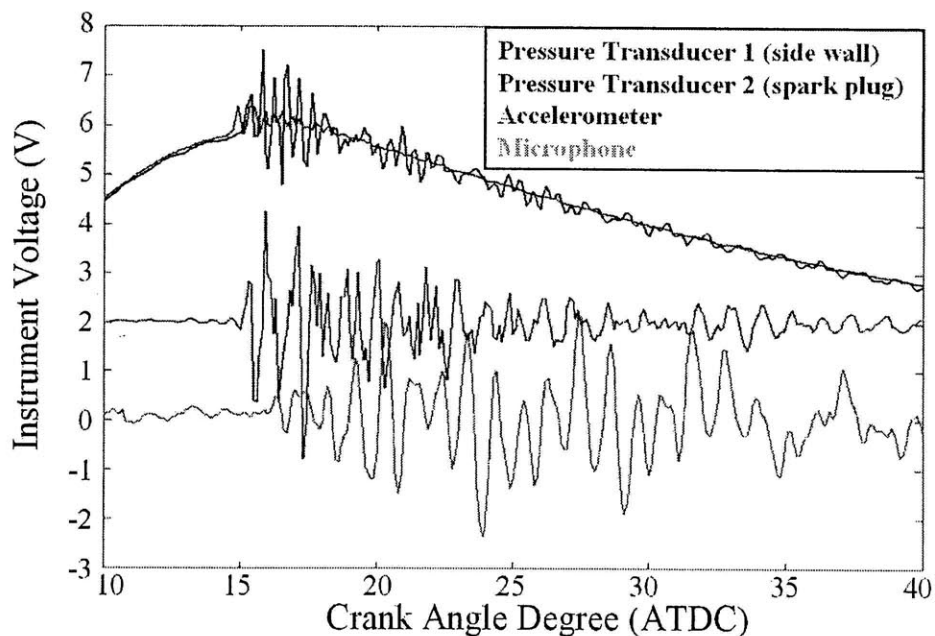
At this operating condition, the spark timing for knock onset was determined to be at  $1^\circ\text{BTDC}$ . Data was collected at this spark timing at a sampling rate of 90 kHz, corresponding to 10 points per CAD at 1500 rpm. This sampling rate meets the Nyquist criterion for the major frequencies corresponding to knock. At this spark timing, 300 cycles of pressure, accelerometer, and microphone data were recorded. The process was repeated with the accelerometer and microphone in different positions.

### 3.3 RESULTS AND DISCUSSION

Figure 3.2 shows the raw output from the two pressure transducers, the accelerometer, and the microphone for a cycle at borderline knock. The accelerometer was mounted on the side of the engine block, and the microphone was located at the side of the engine, 1 cm away from the block. The plot shows that autoignition occurs at  $15^\circ\text{ATDC}$ , corresponding to the pressure rise noted by both pressure transducers. The accelerometer begins to measure vibrations

approximately 0.1 ms after the pressure transducers begin recording the pressure oscillations in the cylinder. The microphone begins to pick up noise at 0.2 ms after the accelerometer begins to measure vibrations. The travel time for a sound wave from the block to the microphone is 0.02 ms, so the time delay between the block vibrations and noise is only partially due to the speed of sound.

The instrument readings in Figure 3.2 explain the development of audible knock. Autoignition causes the pressure of the gas in the cylinder to oscillate; these oscillations are picked up by the pressure transducers. The oscillations of the gas in the cylinder cause the entire engine block to vibrate. These vibrations, which are detected by the accelerometer, build up and decay much slower than the pressure oscillations. The engine block vibrations emit a noise that is picked up by the microphone.



**Figure 3.2: The synchronized raw instrument voltage from the two pressure transducers, the accelerometer, and the microphone for a cycle at borderline knock.**

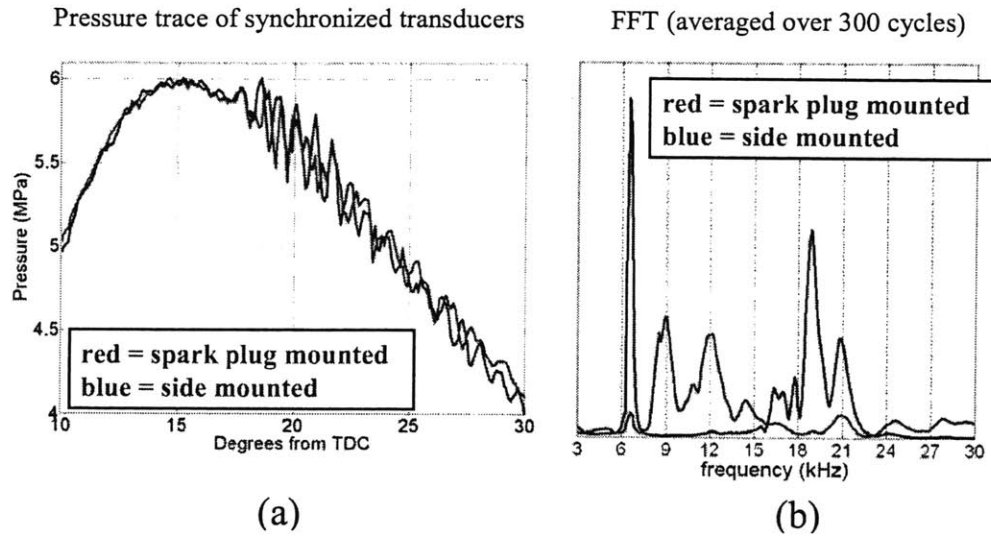
The pressure measurements in Figure 3.2 show that the different pressure transducers measure pressure oscillations of different frequency and intensity. Experiments were performed to determine more exactly how the location of the pressure transducer relates to the oscillations



recorded by the instruments. Figure 3.3a shows the simultaneous pressure trace for a borderline knocking cycle measured by the side mounted and spark plug mounted pressure transducers. The pressure traces match until 17°ATDC, approximately at knock onset. Following knock onset, both transducers record strong oscillations in the in-cylinder pressure.

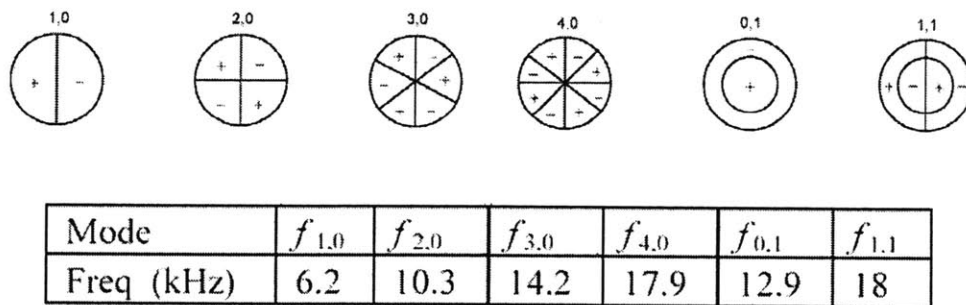
The FFTs of the two signals, averaged over 300 cycles, are shown in Figure 3.3b. The side mounted pressure transducer has oscillations in the 6 kHz range and in the 15-22 kHz range. The spark plug mounted pressure transducer records oscillations in the 9 kHz and 12 kHz range. The excited frequencies correspond to the different resonant modes in the chamber. Draper [27] calculated and experimentally measured the different resonant modes of a combustion chamber, and the results are shown in Figure 3.4. Other studies have found similar results [28,29]. The combustion chamber in Draper's study was cylindrical, so it has a different geometry and hence different frequencies from the one used in this study. However, the results from Draper's study are still relevant, in that the different geometries should only create major changes in the axial modes, which Draper neglected.

The 6.2 kHz signal recorded by the side mounted transducer corresponds to the first circumferential mode. This mode has a node point at the location of the spark plug transducer, hence why that transducer did not record that frequency. The 15-22 kHz frequency range could correspond to several different modes. The range of frequencies hints that these frequencies might correspond to the first axial mode, which changes with the piston position. Since the 6 kHz mode's length scale is the bore of the engine (83 mm), a simple scaling analysis would give that the fundamental axial mode is approximately 15.8 kHz, which is in the range of higher frequencies excited in the test engine. Since the engine has a pent-roof design, calculating the exact axial modes cannot be done analytically and can only be determined through a finite element routine. Alternatively, Draper [27] states that multiple higher-order circumferential and radial frequencies fall within this range also.



**Figure 3.3: (a) Sample pressure trace of engine at borderline knock using a side-mounted pressure transducer and a spark plug pressure transducer. (b) Frequency spectrum of pressure measurements at two different instrument locations averaged over 300 cycles.**

The frequencies measured by the spark plug pressure transducer are not as well defined as the 6.2 kHz frequency from the side-mounted pressure transducer. However, they are better defined than the 15-22 kHz frequency range. According to Figure 3.4, the 9 kHz signal corresponds to the second circumferential mode, and the 12 kHz signal corresponds to the first radial mode.

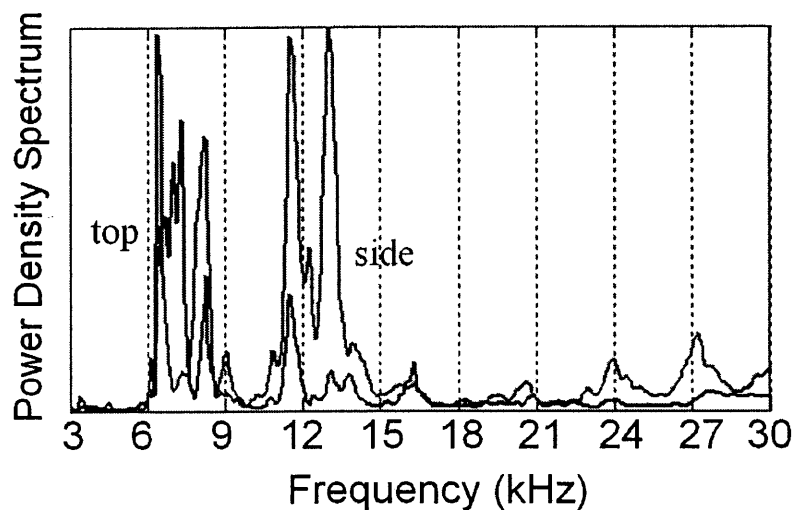


**Figure 3.4: The different radial and circumferential modes of a cylinder at 2000 K, as calculated and measured by Draper [27].**

Since the pressure transducers measured different oscillations at different measuring locations, it follows that the accelerometer should measure different block vibrations depending on its

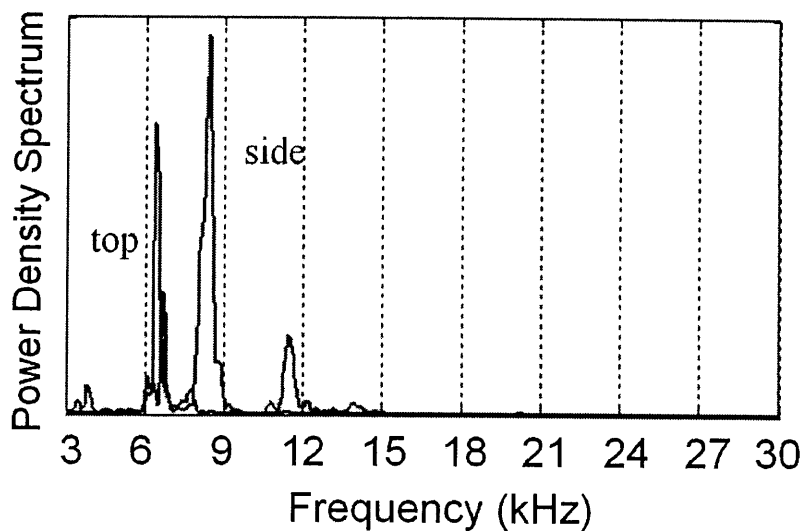
measuring location. Figure 3.5 displays the average FFT of 300 cycles of accelerometer data measured at the two different instrument positions at borderline knock. The FFT of the block vibrations show many more excited frequencies than that of the pressure oscillations. These additional frequencies are excited because the block has many resonance frequencies due to its complicated geometry. However, the prominent geometric feature in the block is the cylinder, so the major frequencies that are excited should correspond to the resonance frequencies of the cylinder.

The accelerometer mounted on the valve cover recorded vibration frequencies primarily in the 6-8 kHz range. Though the side mounted accelerometer also recorded these frequencies, it also recorded large components in the 11-13 kHz range. These frequencies correspond to some of the frequencies measured by the pressure traces. Accelerometer measurements were also taken at normal non-knocking conditions to verify that these frequencies were not excited at non-knocking conditions.



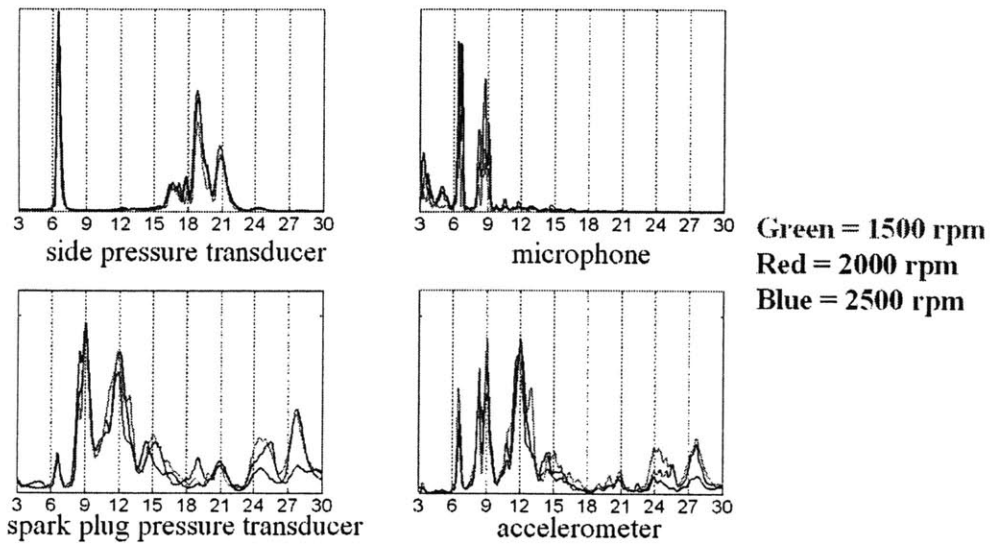
**Figure 3.5: Frequency spectrum of accelerometer signals (averaged over 300 cycles) for an accelerometer mounted on the side of the block (red) and on top of the valve cover (blue) at heavy knock.**

Similarly, the microphone signals were recorded with the microphone in the two different locations shown in 3.1. The average FFT of 300 cycles is shown in Figure 3.6 for the two microphone positions. The audible noise picked up by the microphone when it was positioned above the valve cover was at approximately 6 kHz. When the microphone was moved to the side, it picked up a 6 kHz signal, an 8 kHz signal, and a 12 kHz signal. When the engine was not knocking, the microphones did not pick up any noise in these frequency ranges. It should be noted that regardless of the location, both signals pick up a 6 kHz signal.

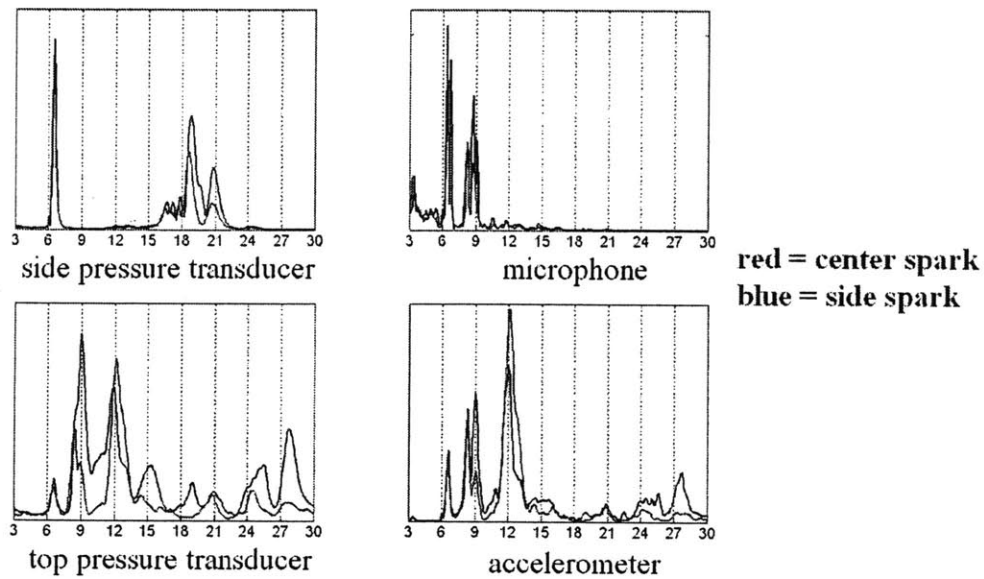


**Figure 3.6: Frequency spectrum of microphone signal (averaged over 300 cycles) for a microphone mounted on the side of the block (red) and on top of the valve cover (blue) at heavy knock**

The experiments were performed at borderline knock for an engine operating with a central spark plug at 1500 rpm. The experiments were repeated at 2000 rpm and 2500 rpm, and the results are shown in Figure 3.7. The knock limited spark advance for UTG91 at 2000 rpm is 11° BTDC, and 14° BTDC at 2500 rpm. The results show that the only frequencies with a speed dependence are the higher frequencies measured by the spark-plug pressure transducer and the accelerometer. However, even these changes are small, and hence the results are independent of speed.



**Figure 3.7: Frequency spectrum of the side pressure transducer, the spark plug pressure transducer, the microphone, and the accelerometer (averaged over 300 cycles) at different engine speeds.**



**Figure 3.8: Frequency spectrum of the side pressure transducer, the spark plug pressure transducer, the microphone, and the accelerometer (averaged over 300 cycles) at different sparking locations.**

The experiments were also repeated with the spark plug moved to the side wall, similar to the sparking position in the octane number tests. The spark-plug pressure transducer was kept at its position at the apex of the pent-roof head. With a central spark-plug, the end gas can be at any location on the circumference of the cylinder; however, with a side spark, autoignition should theoretically occur on the opposite end of the cylinder wall. The location of the autoignition should cause different modes to be excited. The results, displayed in Figure 3.8, show that the location of the spark does not significantly change the frequencies excited. This trend can only occur if the end-gas location does not depend on the spark-location, which can be due to the presence of large turbulent eddies. The only significant difference appears in the higher frequencies picked up by the spark-plug pressure transducer.

### **3.4 CONCLUSIONS**

The experimental investigation into knock metrics indicates the following:

- For the three different metrics tested, the knock intensity and excited frequencies depend on the instrument location.
- However, for the accelerometer and microphone, it was found that the 6 kHz frequency was picked up at all tested instrument locations.
- The range of frequencies picked up, and their variability with location creates a large amount of complexity in quantifying knock.
- Therefore, though it might be arbitrary, the use of audible knock as the knock onset metric, is perhaps the most reliable.

## **CHAPTER 4: PHYSICS OF KNOCK IN MODERN SI ENGINES COMPARED TO THAT OF THE OCTANE NUMBER TESTS**

Engine geometries and operating conditions have changed significantly since the development of the octane tests; thus the physical properties of knock must have similarly changed. For the octane number tests to still be relevant, they must capture the important physical phenomena of knock in modern engines. The physics of knock in a modern SI engine was studied and compared to that of the octane number tests.

### **4.1 PHENOMENA THAT GOVERN KNOCK ONSET IN MODERN SI ENGINES**

#### **4.1.1 DEPENDENCE OF KNOCK ONSET ON IN-CYLINDER PRESSURE**

It is well known that the fundamental knock variables are the end-gas temperature, pressure, and the flame propagation rate and travel distance (the time for the flame to move from the spark plug to the cylinder walls). The highest end-gas mixture temperature occurs at the crank-angle of peak pressure, due to piston motion and combustion produced end-gas compression. Thus, cylinder pressure development in an individual engine cycle is a useful source of information on the evolution of these basic knock variables and how knock then occurs.

Different cycles have been found to show substantial variability in the knock phenomenon. This is largely due to cycle-to-cycle variations in the burn rate, which result in variations in the cylinder pressure and end-gas temperature profiles. In general, faster burning cycles produce higher peak pressures and end-gas temperatures that are more likely to knock at a higher intensity [30]. Flame geometry also varies cycle-by-cycle, so the end-gas location and shape varies accordingly. With the engine geometry used for this study, the circumferential location of the end-gas region is unclear, and may vary significantly cycle-by-cycle [31, 32]. In addition, end-gas composition and temperature non-uniformities are thought to be significant. All of these factors result in the cycle-by-cycle variability in the knocking phenomenon being substantially

larger than the cycle-by-cycle combustion variability. This has made understanding what determines the onset of audible knock especially difficult.

As detailed in Chapter 3, the quantitative interpretation of the pressure signal depends on the pressure transducer location relative to the acoustic modes excited by the autoigniting end-gas. Since, knock is fundamentally a noise, the relevant frequency is the 6 kHz frequency, the major frequency in the audible range. Since the spark-plug transducer is at a node for this frequency, it cannot adequately capture the physical properties of knock onset. However, the side pressure transducer found a very strong 6 kHz signal, and hence this transducer is used for this analysis. Additionally, the instrument location corresponds to the location of the pressure transducer for the CFR Engine.

#### **4.1.2 EXPERIMENTAL PROCEDURES**

Experiments were performed in the test engine described in Chapter 2 to build a better understanding of the knock onset phenomena. The engine was set to run at a base condition of stoichiometric, WOT, unheated (intake air temperature = 30°C), and at 1500 rpm. These experiments were run with TRF95, which has a RON of 95 and a MON of 83.4. The steps taken to complete a spark timing sweep are as follows:

1. Set the engine to run at 1500 RPM, stoichiometric, and unthrottled.
2. Run engine at steady state until the coolant temperature is at 100°C.
3. Find the spark timing corresponding to audible knock onset.
4. Retard the spark timing by 3° CA.
5. Record conditions and cylinder pressure data at a sampling rate of 90 kHz.
6. Advance the spark timing in increments of 1° CA, repeating Step 5 for each increment until the spark timing is 3° CA advanced from the knock onset timing.

All of the experiments were run in one day to minimize the changes in the engine intake conditions. The intake air temperature deviated less than 0.2°C from 36°C. The average intake pressure was 0.988 bar with deviations less than .002 bar. These deviations in intake conditions are small enough to not play a significant role in knocking behavior.



From the cylinder pressure data, two techniques are typically employed to quantify knock intensity [33]. The first technique involves integrating across a frequency range of the FFT of the cylinder pressure trace. This integral spans a range corresponding to the frequencies of interest, typically any frequency greater than 2 kHz. This threshold is set to remove the low frequencies that are present at non-knocking engine conditions. Another technique is to determine the peak-to-peak amplitude of the filtered pressure signal. Again, a high-passed signal is typically used, though a bandpassed signal around a certain frequency range is often employed. The knock intensities from these two techniques correlate linearly with each other. Both techniques are used in this study.

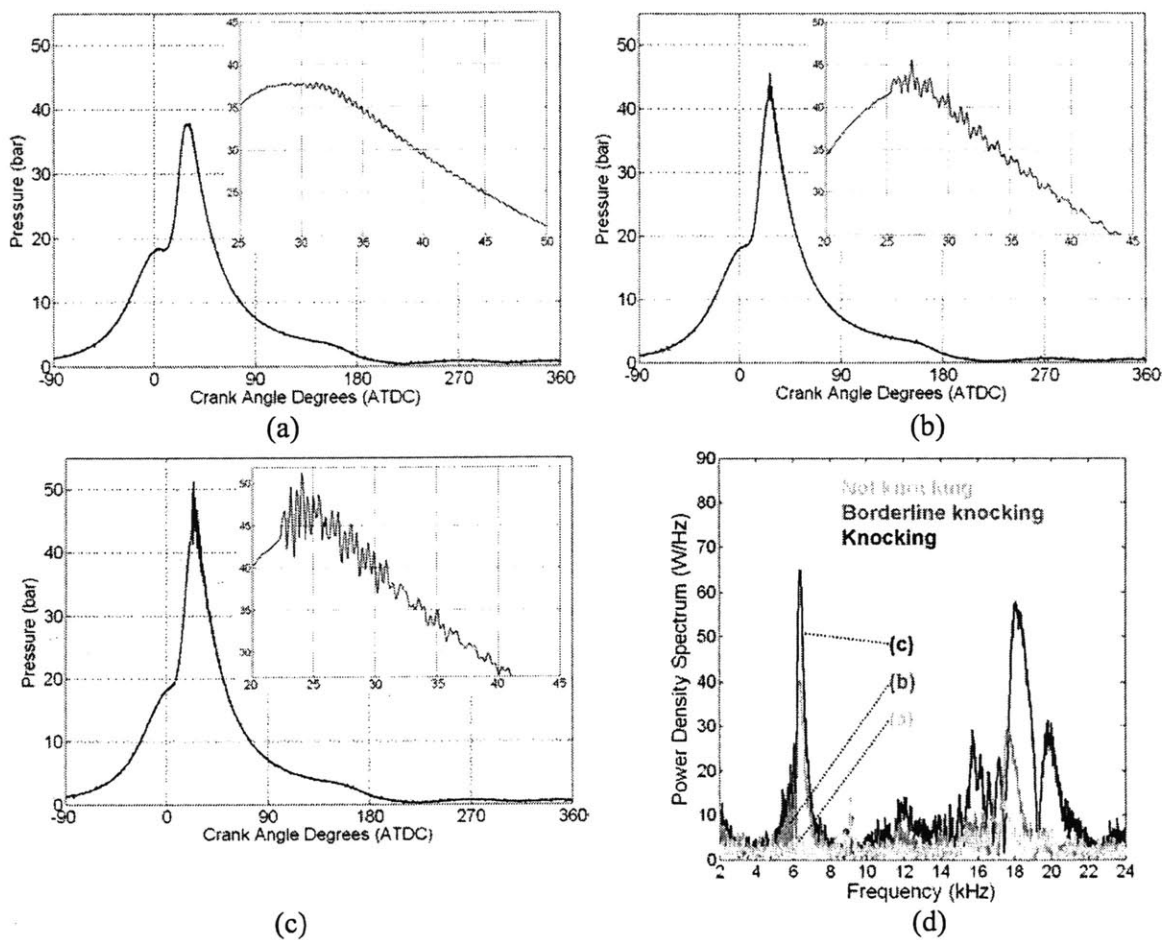
#### 4.1.3 RESULTS AND DISCUSSION

Figure 4.1 shows examples of the cylinder pressures for individual cycles at different spark timings. These cycles were chosen by averaging the pressure trace for 100 cycles at that spark timing and finding the cycle with the closest value and location of maximum pressure. Figure 4.1(a) shows a cycle at a spark timing  $2^\circ$  retarded from borderline knock, Figure 4.1(b) shows a cycle at borderline knock, and Figure 4.1(c) is at a spark timing  $2^\circ$  advanced from borderline knock. Figure 4.1(d) shows an overlay of the FFTs of these 3 cycles.

The FFT shows that as the engine transitions through borderline knock, two ranges of frequencies are excited. The lower frequency is around 6 kHz and corresponds to the first circumferential frequency of the combustion chamber as detailed in Chapter 3. The single peak at this frequency is well defined. A second range of frequencies is observed between 15 and 22 kHz, which could correspond to a number of different modes as detailed in Chapter 3. Regardless, these higher modes are above the threshold of human hearing and hence do not contribute to the audible noise associated with knock.

Figure 4.1(a) shows a cycle when the engine is not audibly knocking. However, pressure oscillations are still visible, starting at  $30^\circ$  ATDC, showing that small amounts of the end-gas are autoigniting. The FFT shows that the oscillations are primarily in the higher frequencies, with

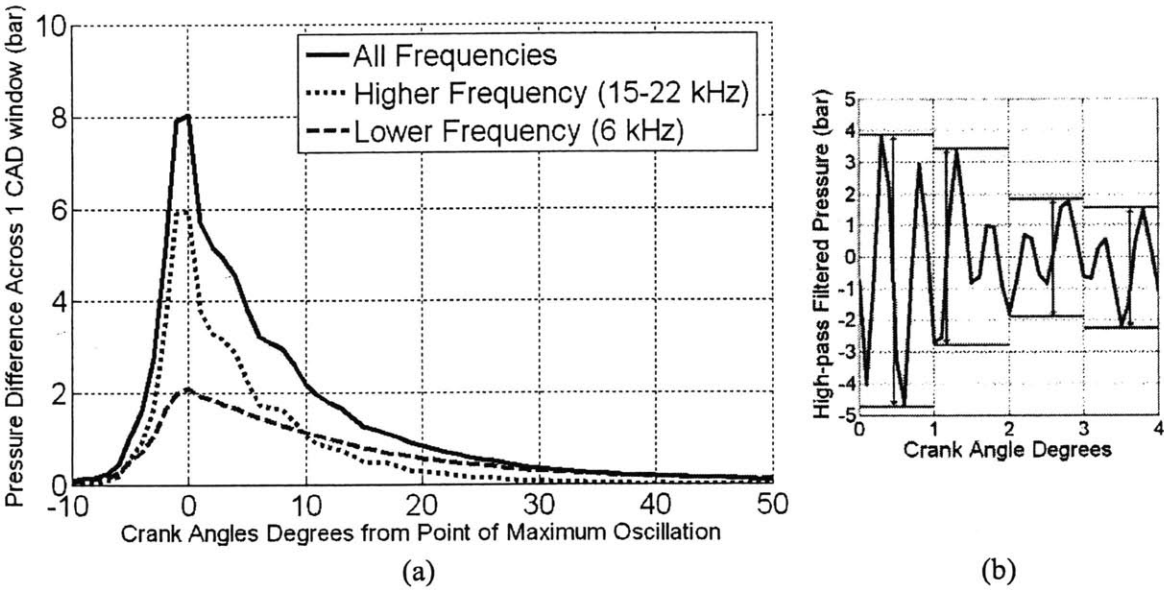
little contribution from the first circumferential mode. As the engine transitions through borderline knock, the amplitude of the pressure oscillations increases, as shown in Figure 4.1(b). This increase in amplitude corresponds to increases in both the lower and higher frequency. However, the transition into the knocking regime appears to be characterized by the rapidly increasing presence of the 6 kHz signal. As the engine continues past knock onset into the knocking regime, the amplitudes of the oscillations at both the lower and higher frequencies continue to increase as shown in Figure 4.1(c).



**Figure 4.1: Pressure traces for a typical cycle for an engine operating at a spark timing corresponding to borderline knocking (b), and with the spark retarded and advanced by  $2^\circ$  such that the engine is not knocking (a) and knocking (c) respectively. The region around TDC for each cycle was enlarged to show the pressure oscillations. Additionally, the FFTs (d) for the three cycles are displayed.**

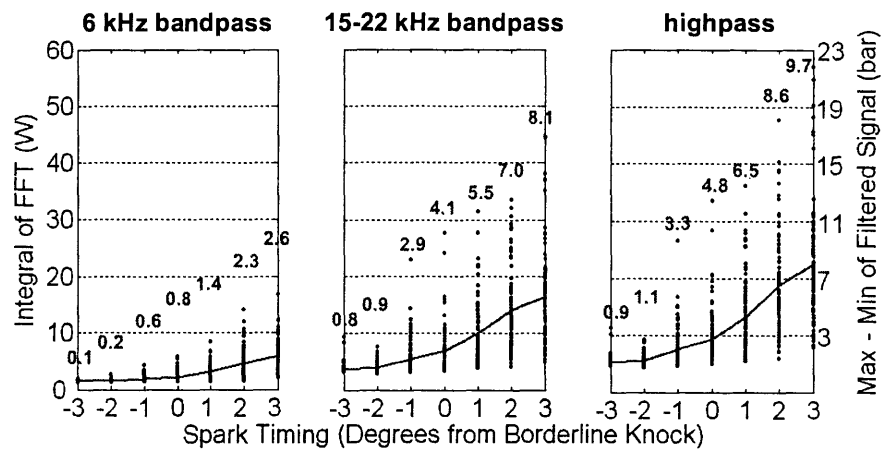
To look at the variation in knock intensity, each cycle was put through low-order bandpassed filters, which isolated the lower and higher frequency components of the signal. Additionally, each cycle was put through a highpass filter to remove the non-autoigniting component of the pressure trace and get the basic “knocking” signal. The threshold for this highpass filter was set at 2.5 kHz.

The filtered pressure data shows that the higher, non-audible frequency dominates the early oscillations but decay more rapidly than the audible 6 kHz mode. Figure 4.2 plots the pressure difference, maximum to minimum, in a 1 CAD window of a filtered signal as a function of crank angle degrees from the point of the maximum oscillation for the average heavily knocking cycle. The plot shows that at 10 degrees from maximum KI, the lower frequency becomes the dominant frequency.



**Figure 4.2:** The pressure difference across a 1 CAD window (b) plotted against crank angle from the point of maximum pressure oscillation (a). The engine was operating at heavily knock. The plot is averaged over 100 cycles.

As stated previously, knock intensity varies significantly from cycle to cycle. For example, at borderline knock, some cycles have both higher and lower frequency modes excited, a single mode excited, or neither mode excited. The knock intensity calculated by integrating the FFT is plotted against the spark timing for each individual cycle in Figure 4.3. The corresponding amplitude of the oscillation is given on the right hand axis. The average knock intensity in terms of the oscillation amplitude is given by the red line, and the standard deviation is given above it.



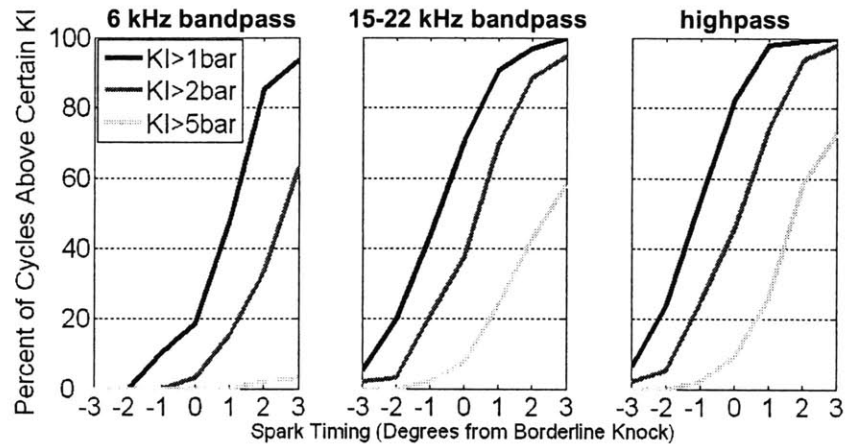
**Figure 4.3: The knock intensity for an individual cycle (black dots) and the average knock intensity (red line) plotted against the spark timing for the 6 kHz bandpass signal, the 15-22 kHz bandpass signal, and the highpass signal. The knock intensity is defined as the integral of the FFT (the right hand axis gives the corresponding amplitude of the pressure oscillation). The number in red above each data set is the standard deviation (in W) of the 100 cycles at that spark timing.**

Figure 4.3 shows that as an engine transitions from non-knocking to knocking, the average knock intensity and standard deviation increase for all three frequency ranges. At heavy knocking conditions, several percent of the cycles have significantly high knock intensities. However, some of the cycles have knock intensities lower than some of the cycles at non-knocking spark timings. Due to cycle-by-cycle variability, there is significant overlap.

Figure 4.4 displays the percent of cycles that have knock intensities greater than 1 bar, 2 bar, and 5 bar. For all three frequency ranges, the same general trend is seen. As the spark timing is

advanced from non-knocking to knocking, the number of cycles above a given knock intensity increases rapidly at borderline knock.

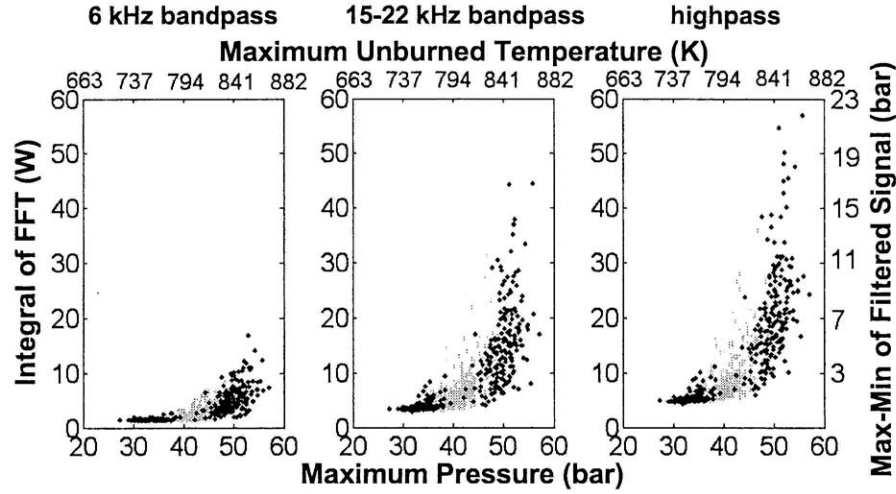
For the highpass filter, approximately 80 percent of cycles have a total knock intensity greater than 1 bar at borderline knock, 50 percent above 2 bar, and 10 percent above 5 bar. As the spark is retarded by 2°, these values drop to 20 percent, 5 percent, and 1 percent. Note that for the 6 kHz frequency mode, a knock intensity of about 2 bar separates the non-knocking cycles from the knocking cycles.



**Figure 4.4: Percent of cycles with a knock intensity greater than 1 bar (black), 2 bar (dark gray), or 5 bar (light gray) plotted against the spark timing for the 6 kHz bandpass signal, the 15-22 kHz bandpass signal, and the highpass signal. The knock intensity used in this definition is the difference between the maximum and minimum of the filtered signal.**

This variability in knock intensity is caused by the cycle variability in the maximum pressure in a cycle, which depends on a range of parameters. Figure 4.5 plots the knock intensity against the maximum pressure of the individual cycle. The value of the maximum pressure is taken from a low-pass pressure trace to remove the contribution from the oscillations. The corresponding maximum end-gas temperature was also calculated through isentropic compression and is shown on the horizontal axis on the top of the figure. The middle three spark timings were plotted in a

lighter color in order to show the transition region between non-knocking and knocking. The regions are distinct though there is some overlap between the three regimes.



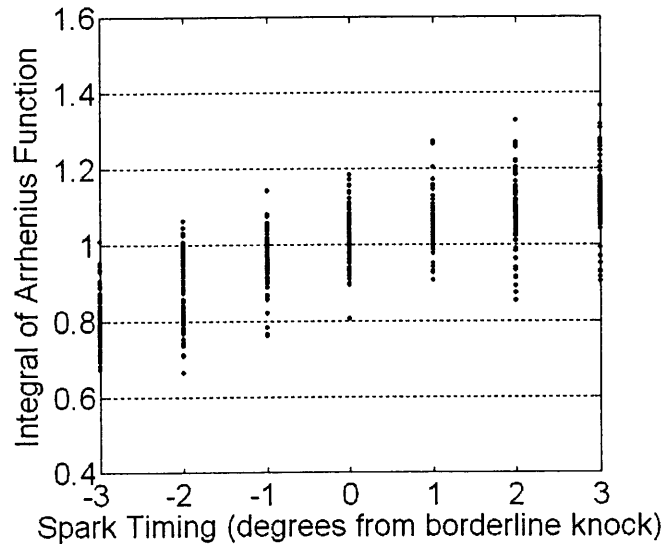
**Figure 4.5: The knock intensity for an individual cycle for the 6 kHz bandpass signal, the 15-22 kHz bandpass signal, and the highpass signal plotted against the maximum pressure of the cycle. On the left hand axis, the knock intensity is defined as the integral of the FFT. The right hand axis gives the corresponding amplitude of the pressure oscillation. Cycles from a borderline knocking engine are plotted in light gray.**

The plots show that as the maximum pressure increases in the cycle, the knock intensity increases. As the maximum cycle pressure increases above 40 bar, the knock intensity rapidly increases. However, the knock intensity changes little at peak pressures below 40 bar (unburned mixture temperatures below about 820 K).

An autoignition integral of the Livengood-Wu/Arrhenius form, as developed by Douaud and Eyzat [34], estimates the fuel-air mixture’s chemical induction time. When this chemical induction time is compared to the elapsed time in the engine, it can be used to indicate when autoignition occurs. This autoignition integral is defined by:

$$\tau_{\text{autoign.}} = \int_{t_{\text{IVC}}}^{t_{\text{max } p}} \left[ 17.68 \left( \frac{ON}{100} \right)^{3.402} p^{-1.7} \exp \left( \frac{3800}{T_u} \right) \right]^{-1} dt \quad (\text{Eq. 4.1})$$

The values of this integral are plotted in Figure 4.6 at each spark timing. According to this correlation, when the integral reaches a value close to 1, the end-gas autoignites. Figure 4.6 shows that the average cycle at borderline knock has an autoignition integral of approximately 1.

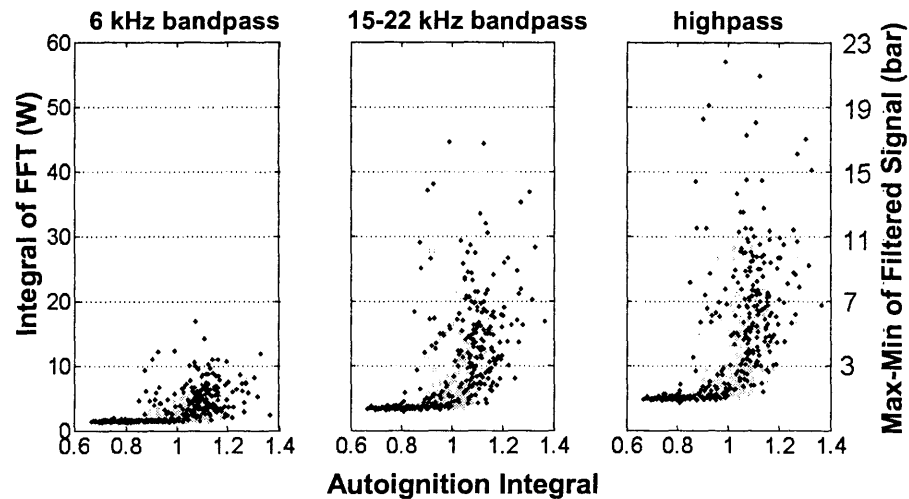


**Figure 4.6:** The autoignition integral (from intake valve closing to CAD of maximum pressure) plotted against the spark timing. The integral was empirically developed by Douaud and Eyzat [34], such that as the integral approaches 1, autoignition occurs.

At higher maximum pressures the integral goes to 1 faster, causing autoignition to occur with a larger quantity of end-gas, in turn causing a larger energy release, resulting in higher amplitude pressure oscillations. Figure 4.7 plots the knock intensity against the values of the autoignition integral from Figure 4.6. The data shows that there is a correlation between the integral value and the knock intensity. The knock intensity is low and stays fairly constant until the integral reaches a value of 1. At approximately 1, the knock intensity rapidly increases, though there is a substantial amount of scatter in the plots. This is consistent with autoignition chemistry correlations developed by Douaud and Eyzat [34].

The autoignition of the end-gas releases a large amount of energy, which manifests itself as a rapid rise in pressure. As the maximum rate of change of pressure in the cycle increases, the knock intensity also increases. Figure 4.5 demonstrated that cycles that have a higher maximum

pressure tend to have a higher knock intensity; cycles that have a higher maximum pressure would also have a higher rate of change in pressure even without the autoignition oscillations. These two trends augment to give a strong correlation between the rate of change of pressure ( $dp/dt$ ) and the knock intensity. Figure 4.8 shows a clear relationship between the maximum value of  $dp/dt$  and the knock intensity.



**Figure 4.7:** The knock intensity for the 6 kHz bandpass signal, the 15-22 kHz bandpass signal, and the highpass signal plotted against the autoignition integral for each cycle. On the left hand axis, the knock intensity is defined as the integral of the FFT. The right hand axis gives the corresponding peak-to-peak amplitude of the pressure oscillation. The data colored in gray correspond to the borderline knocking cycles.

The relationship between the maximum value of  $dp/dt$  and the knock intensity is essentially linear, especially for the higher frequency range. The relationship is still apparent though with larger data scatter for the lower frequency. It follows that the maximum value of  $dp/dt$  is a good indicator for engine vibration, and a potential indicator for audible knock.

The mass fraction burned at the point that the autoignition integral goes to 1 was determined and plotted against knock intensity in Figure 4.9. As the percentage of end-gas autoigniting increases up to 20 percent (or 80 percent mass fraction burned), the knock intensity increases. However, when autoignition occurs with less than 80 percent mass fraction burned, the knock intensity



decreases. With large amounts of end-gas, the rate of pressure rise during the autoignition process decreases [29], hence decreasing the knock intensity.

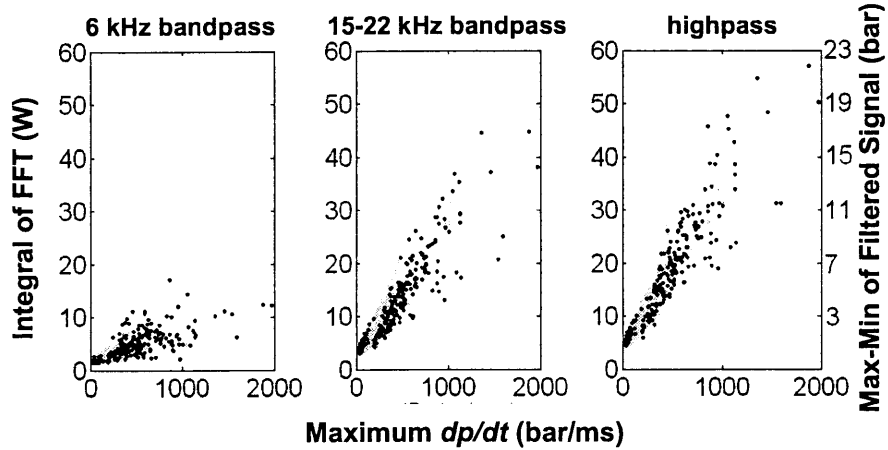


Figure 4.8: The knock intensity for the 6 kHz bandpass signal, the 15-22 kHz bandpass signal, and the high-pass signal plotted against the maximum value of  $dp/dt$ . On the left hand axis, the knock intensity is defined as the integral of the FFT. The right hand axis gives the corresponding amplitude of the pressure oscillation. Cycles at borderline knock are plotted in gray.

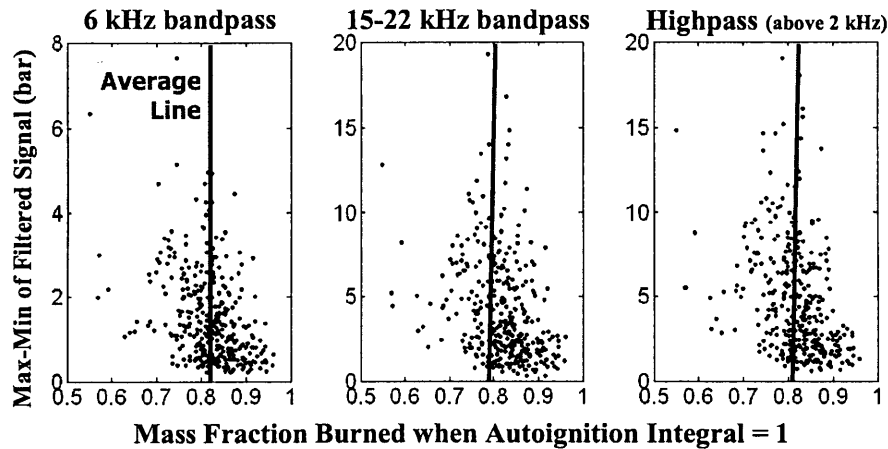


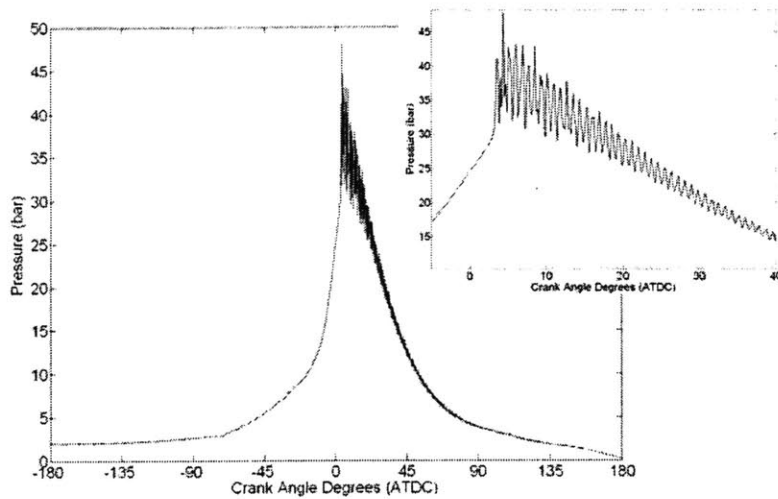
Figure 4.9: The knock intensity for the 6 kHz bandpass signal, the 15-22 kHz bandpass signal, and the highpass signal plotted against the mass fraction burned when autoignition integral (Eq 4.1) goes to 1 for each cycle. Maximum knock intensity is achieved when the mass fraction burned at knock onset is 80 percent.

## 4.2 PHENOMENA THAT GOVERN KNOCK IN OCTANE NUMBER TESTS

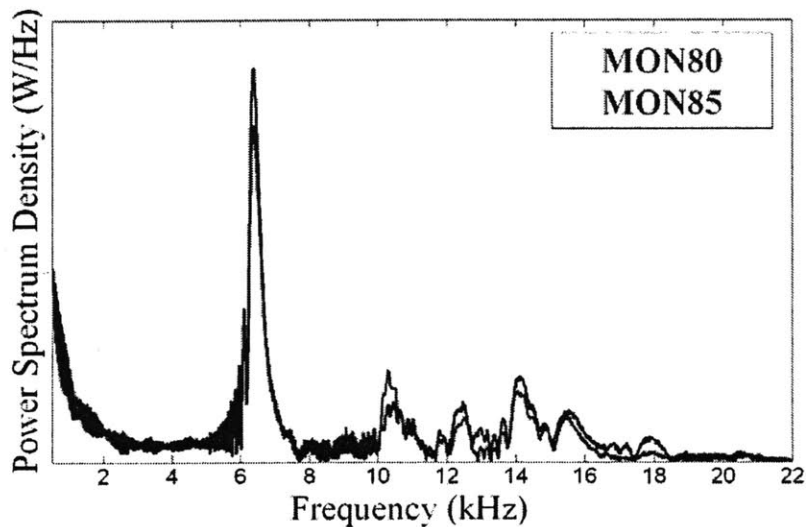
The study on knock in the octane number tests is limited due to the lack of available data, since the octane number tests are performed in very specialized Cooperative Fuel Research (CFR) engine. Waukesha Engine Corporation, the manufacturer of the CFR engine, provided a small sample of pressure traces for knock in a CFR Engine at MON test condition [35]. These pressure traces are considered representative of the average pressure trace for a given condition. The pressure transducer was located at the side wall in the cylinder, as shown in Appendix A; this location is similar to the side-mounted pressure transducer used in the test engine from the previous section.

Figure 4.10 gives the sample pressure trace for the MON80 test condition with PRF80. The trough-to-crest amplitude of the knocking signal is 15 bar, which corresponds to heavy knock. The corresponding mass fraction burned at the point of autoignition is between 60 and 70 percent [36]. Hence, knock onset occurs very early with a large amount of end-gas. When this large end-gas volume autoignites, it releases a large amount of pressure, which then manifests itself as large pressure oscillations.

Figure 4.11 gives the FFTs of the MON80 and MON85 test for the corresponding PRF. The FFT shows that for both tests, there are two ranges of excited frequencies. The first range of excited is around 6 kHz. This frequency corresponds with the first circumferential mode, similar to what was seen for the test engine in the previous section. The second range of excited frequencies is between 10 and 18 kHz. The magnitudes of these oscillations are much less than the 6 kHz frequency; additionally, they are above the threshold of human hearing. These frequencies are listed in Figure 3.3 as corresponding to different radial and circumferential modes. The analysis in the earlier section shows that the block vibrates at the frequencies measured by the pressure transducers. The block vibrations then generate noise at these frequencies. Thus, the higher frequency oscillations would cause noise that is above the threshold of human hearing. However, the 6 kHz frequency range is within the range of human hearing and generates the noise associated with knock.



**Figure 4.10: Pressure trace for a typical cycle for a CFR engine operating at the MON80 test conditions.**



**Figure 4.11: Frequency spectrum for an average cycle in the MON80 (blue) and MON85 (red) test**

At the time of the publication, Waukesha was not able to provide similar traces for RON tests. However, the physics of knock for the RON test should be similar since the tests are performed in the same engine. Additionally, over the relevant range of RON and MONs for modern

engines, the compression ratio does not change significantly between the tests for a given octane number.

However, the temperature and speed differences between the tests could affect the physics of knock. The acoustic modes inside of an engine are proportional to the speed of sound, which in turn is proportional to the square root of temperature. Decreasing the temperature from 2200 K to 2000 K would only result in a 5 percent change in the frequencies. The speed plays a significant role in the cycle-to-cycle variability in the engine. Due to the design of the CFR engine, there are substantial standing waves in the mixture stream. The strength of the standing wave increases with the engine speed, such that these waves are negligible in the RON test but prominent in the MON test. These standing waves could increase or decrease the intake mixture pressure depending on the valve timing, increasing the cycle-to-cycle variability. [35]

#### **4.3 DIFFERENCES BETWEEN KNOCK IN MODERN SI ENGINES AND CFR ENGINES**

Several key differences between the octane tests and modern engines can be noted from the previous two sections in regards to the physics of knock. First, the octane tests operate at heavily knocking conditions, which are typically avoided by modern engines due to the inclusion of knock sensors. Second, heavy knock in modern engines corresponds to 20 percent of fuel charge autoigniting; in the octane tests, almost twice as much of the charge autoignites. Third, the MON test has significantly high cycle-to-cycle variability due to pressure waves in the intake system; modern engines operate are tuned to correct for these pressure waves. The most significant difference in terms of the physics of knock is the differences in engine geometry between the CFR engine and modern engines, which cause the engine cylinders to resonate at different frequencies.

For the RON and MON tests to properly capture the properties of knock in modern engines, the physical phenomena must be similar. The physical properties of knock are tied to the engine geometry. However, the engine geometries for the two engines are quite different. Modern

engines have pent-roof combustion chambers similar, while the CFR Engine has a pancake shaped combustion chamber. Both engine geometries are shown in Figure 4.11.

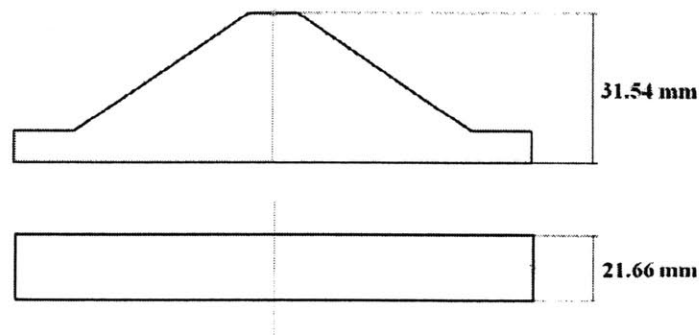
Draper's analysis, discussed in Section 3.3, neglects the axial modes, which were not excited in a CFR Engine. This follows from the wave equation:

$$\frac{\partial^2 P}{\partial t^2} = c^2 \nabla^2 P \quad \text{where } c = \sqrt{\gamma RT} \quad (\text{Eq. 4.2})$$

which can be solved with Dirichlet boundary conditions to get the resonant frequencies equal to

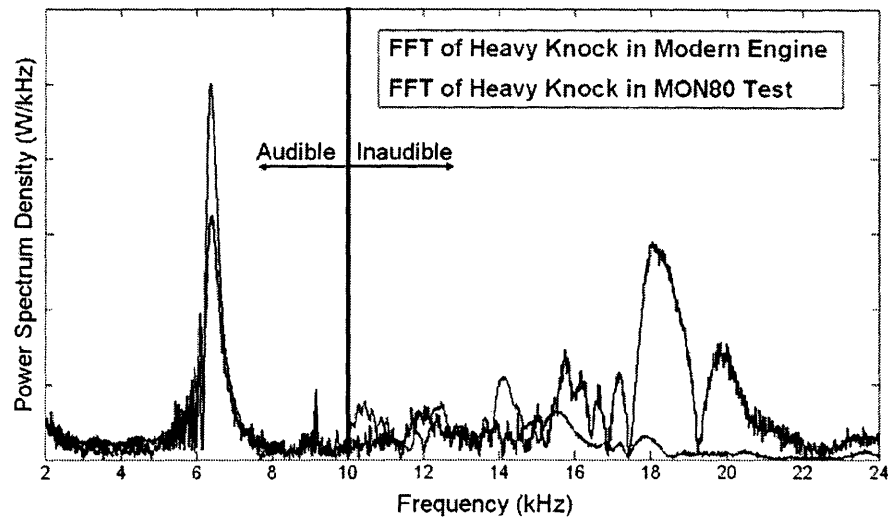
$$f_{m,n,p} = \alpha_{m,n,p} \frac{c}{\pi L_{m,n,p}} \quad (\text{Eq. 4.3})$$

where  $\alpha_{m,n,p}$  is the wave number determined from the Bessel Equation and  $L_{m,n,p}$  is the relevant length scale. A plot that compares the relevant axial length scales for a CFR engine and the test engine at knock onset is given in Figure 4.12. The CFR Engine, which was used in Draper's analysis, has a pancake shaped combustion chamber. For this engine at the MON80, the axial distance between the cylinder head and the piston at knock onset is 21.66 mm. The test engine's combustion chamber is shaped like a pent-roof and hence has a distance of 31.54 mm. According to Draper [27], the very high axial frequencies in a CFR engine would be difficult to excite. However, since the axial length is much larger for the modern engine, the corresponding axial frequency in the test engine is lower, and hence can potentially be excited.



**Figure 4.12: Cross section of the engine geometries for a modern pent-roof engine (top) and the CFR engine (bottom) at knock onset.**

Figure 4.13 shows that two ranges of frequencies are excited when either engine is in a heavily knocking regime. The first set of frequencies for both engines is around 6 kHz. This frequency corresponds to noise within the range of human hearing and is related to the first circumferential mode of both engines, since both engines have similar size bores. The second sets of frequencies for both engines are above the range of human hearing. These correspond to higher circumferential or radial modes and perhaps axial modes.



**Figure 4.13: Frequency spectrum for an average cycle in the MON80 (red) test and for an average of 300 cycles in a modern engine at heavy knock (red).**

Though the higher frequencies could contribute to engine damage, the lower frequencies are more important because knock is typically considered a noise issue. Wards Database gives that the typical bore for an SI engines in 2008 is 87 mm, which is within 5% of the bore of the CFR engine. The maximum temperatures at WOT for modern naturally aspirated engines is also on the same order of the CFR Engine. However, these temperatures increase as engines get boosted, hence causing an increase in the circumferential frequency. Therefore, the CFR Engine captures the important physical characteristics of knock in modern naturally aspirated engines. However, these physical phenomena no longer match as engines move towards being boosted.

#### 4.4 CONCLUSIONS

These analyses on the physics of knock in a modern SI Engine operation compared to knock in the octane tests indicate the following:

- In the test engine, the pressure waves associated with autoignition excite two ranges of frequencies. The lower frequency at about 6 kHz corresponds to the first circumferential acoustic mode of the combustion chamber. The higher range of frequencies is broader (15-22 kHz) and may correspond to the first axial acoustic mode.
- For the modern SI engine, at the audible knock limit, individual cycle knock intensities above about 2 bar (maximum value of peak-to-peak pressure oscillations) start to occur in a few percent of the cycles at 6 kHz, the oscillation frequency within the audible range. As spark timing is advanced, knock intensity increases, and the fraction of cycles with intensity above this threshold at 6 kHz increases rapidly.
- The CFR engine showed a similar 6 kHz mode. However, a range of higher frequencies between 11 kHz and 18 kHz are also excited, corresponding to different radial and circumferential modes. The difference in geometries between the CFR engine and modern engines result in different high frequencies being excited. These high frequencies are above the audible threshold (~10 kHz).
- Since knock is fundamentally an engine noise, only the 6.2 kHz frequency is relevant. Therefore, the octane tests capture the physics of *audible* knock in modern engines.

(this page intentionally left blank)



## **CHAPTER 5: THE DEPENDENCE OF K VALUES ON DIFFERENT ENGINE PARAMETERS**

Since the Research and Motor Octane Numbers are the Octane Indices of a fuel at two fixed conditions, the Octane Index can be interpolated using a weighing factor K:

$$OI = K \text{ MON} + (1-K) \text{ RON} = \text{RON} - K S \quad (\text{Eq. 5.1})$$

For example, commercial premium fuels have a RON of 96 and MON of 87. If the tests properly bracketed the knock limited regime in modern engines, this fuel would be expected to have the same autoignition characteristics of a PRF containing between 87 and 96 percent iso-octane. In this case, K is between 0 and 1. However, when K is negative, the engine condition is outside of that bracketed by the RON and MON tests. At a condition with a negative K, this fuel would behave like a PRF blend containing more than 96 percent iso-octane. Hence, it would have better antiknock performance than what its octane numbers predict.

This study sets out to determine how the parameter K depends on different engine operating conditions. The results are then used to develop a fundamental meaning for this term.

### **5.1 EXPERIMENTAL STUDY**

#### **5.1.1 EXPERIMENTAL PROCEDURES**

The test engine described in Chapter 2 was set up to run under steady state at the conditions listed in Table 5.1. These operating conditions were chosen because they are representative of the knock-limited condition of modern engines. The intake air temperature and intake air pressure are at the EPA values for standard conditions for temperature and pressure. Engines are normally constrained to operate around stoichiometric to limit emissions. The compression ratio and spark location are consistent with modern SI engines. The knock limited range of engine speeds is between 1000 and 2500 rpm, and hence 1500 is approximately in the middle.

The engine was allowed to warm up, such that the coolant temperature would be stable at 100°C. The spark timing was highly retarded to ensure that the engine was not knocking. Keeping the other conditions in the table fixed, one condition was varied at a time. The spark timing was then advanced through the knock limit. At each spark timing, pressure, microphone, and accelerometer data was taken at 90 kHz for 400 cycles. This spark timing sweep was then repeated for a range of PRFs, at each test condition, to determine their knock limited spark advances. The OI for each fuel was then determined by comparing the fuel's knock limited spark advance to that of the PRFs. This technique for determining the OI follows the Modified Borderline Research Technique [37].

Air Fuel Ratio	$\lambda = 1$
Speed	1500 RPM
Compression Ratio	9.8
Intake Air Temperature	25°C
Intake Air Pressure	1.0 bar
Spark Location	Central

**Table 5.1: Base engine operation conditions**

The results from Chapter 4 described knock onset as corresponding to the spark timing where more than 50% of the cycles had 6 kHz pressure oscillations greater than 2 bar. For this study, knock onset was determined both audibly and through this metric. The two techniques had good agreement. The accelerometer and microphone data were used to validate knock onset.

Experiments to determine the knock limited spark advance for a range of fuels, including PRFs, were conducted by Gerty [38] in the same test engine. The experiments in that study measured the knock limited spark advance audibly. Experimental data from that study was included in this study.

### 5.1.2 EXPERIMENTAL FUELS

The goal of this study is to gain a better understanding of the role of a fuel's sensitivity in its antiknock performance. Accordingly, appropriate sets of test fuels were chosen for this study.

The first set of fuels is presented in Table 5.2, and has a constant RON of approximately 96, corresponding to US premium grade gasoline. However, the MON ranged from 79 to 96, allowing for a spread of sensitivities from 0 to 17. The fuels included a PRF, a toluene reference fuel (mixture of toluene and n-heptane)\*, toluene/PRF blends, a standard test gasoline (UTG96), an olefinic (diisobutylene) mixture, and an ethanol blend. The fuels chosen have very different compositions and, as a consequence, different auto-ignition chemistry processes.

Fuel	RON	MON	(R+M)/2	S
PRF96	96.0	96.0	96.0	0.0
11% n-heptane, 53% iso-octane, 36% toluene	96.2	91.3	93.8	4.9
16% n-heptane, 28% iso-octane, 56% toluene	96.1	88.4	92.3	7.7
22% n-heptane, 0% iso-octane, 78% toluene	96.1	84.5	90.3	11.6
63.5% ethanol, 36.5% n-heptane	96.0	79.0	87.5	17.0
25% diisobutylene, 61% iso-octane, 14% n-heptane	96.0	89.0	92.5	7.0
UTG96	96.1	87.0	91.6	9.1

**Table 5.2: Fuel Set 1. These fuels all have a RON of approximately 96, but varying MON.**

The second set of fuels is less extensive and is presented in Table 5.3. The RON was fixed at 91, and the MON was varied from 79 to 91. This set is primarily to verify that the results from the first fuel set also hold for a fuel set at the U.S. regular gasoline RON value.

Both UTG91 and UTG96 are standard unleaded test gasolines produced by Chevron-Phillips. These fuels are representative of regular and premium on-the-road gasolines.

The tests performed by Gerty [38] used toluene reference fuels with RONs of 85, 90, 95, and 100. The corresponding MON values for these fuels are 74.1, 78.6, 83.4, and 88.5.

\* The naming convention for a TRF: TRF X is a blend of toluene and n-heptane that has a RON of X. For example, TRF96 has a RON of 96 and contains 78 percent toluene and 22 percent n-heptane.

Since the premise behind the OI is to compare fuels to blends of PRFs, this experiment also included a range of PRFs from PRF80 to PRF105. PRFs with values below 100 are blends of iso-octane and n-heptane; PRFs with values above 100 are blends of iso-octane and tetra-ethyl lead. The blending volumes for these PRFs are given in the ASTM standards [10, 11].

Fuel	RON	MON	(R+M)/2	S
PRF91	91	91	91	0.0
16% n-heptane, 53% iso-octane, 31% toluene	90.7	86.4	88.6	4.3
21% n-heptane, 28% iso-octane, 51% toluene	90.9	83.6	87.3	7.3
28% n-heptane, 0% iso-octane, 72% toluene	90.8	79.3	85.0	11.5
UTG91	90.8	83.0	86.9	7.8

**Table 5.3: Fuel Set 2. These fuels all have a RON of approximately 91, but varying MON.**

### 5.1.3 HOW SENSITIVITY AFFECTS KNOCK LIMITS

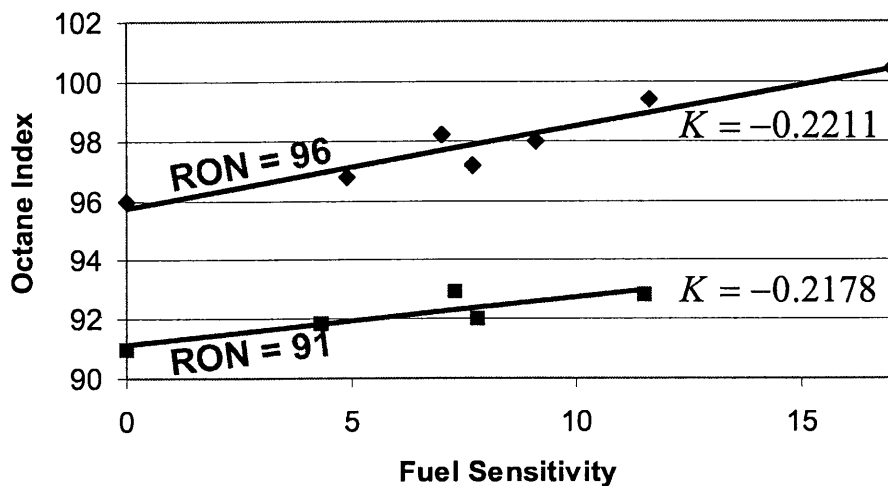
For a fixed RON, a negative K implies that the OI increases as the sensitivity of the fuel increases. To explore this trend, the OI was experimentally measured for the fuels described in Tables 5.2 and 5.3 at the base test conditions given in Table 5.1. The results show that the OI increases linearly with the sensitivity of the fuel as shown in Figure 5.1. K was determined to be -0.22 for both fuels. These results show that K is independent of RON and MON, verifying the form of equation:  $OI = RON - KS$ .

As the OI of the fuel increases, the knock limited spark advance is earlier. This trend occurs because as the OI increases, the fuel's antiknock characteristics behave similar to a PRF containing more iso-octane. As a binary mixture, a PRF follows the simple trend that as the percentage of iso-octane (i.e. the octane number) increases, its anti-knock quality also increases. The plot of fuel sensitivity versus knock-limited spark advance is shown in Figure 5.2 for both

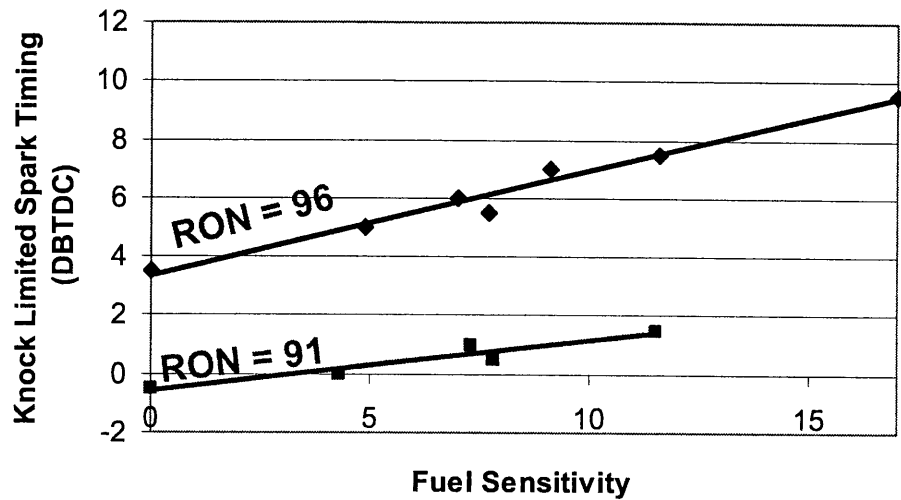
fuel sets. These results show clearly that fuels with a higher sensitivity have less retarded knock limited spark timings. The two fuel sets appear to have different slopes. This occurs because the RON91 fuel set requires a high amount of spark retarding.

The knock limited spark advance is directly related to the maximum operating pressure as shown in Figure 5.3. Figure 5.3 shows that if the knock limited spark advance is earlier, the maximum operating pressure increases linearly. The values shown in Figure 5.3 were measured with PRF105 to avoid knocking at the advanced spark timings.

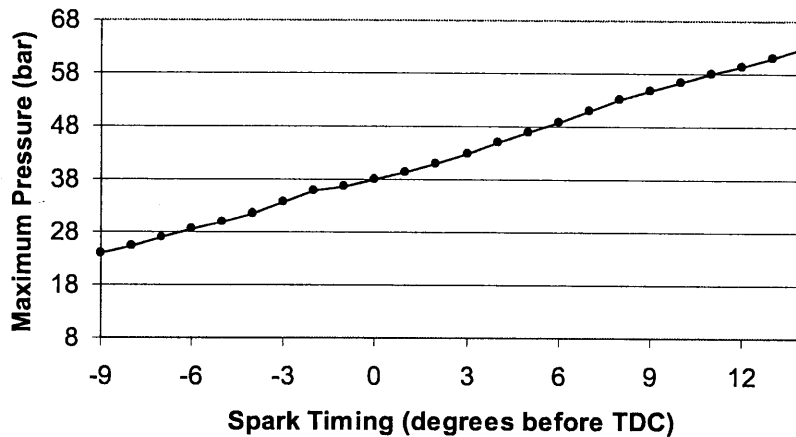
Figure 5.4 displays the data from Figure 5.2 as a function of knock-limited maximum pressure. Figure 5.4 shows that fuels with a higher sensitivity, but a fixed RON can operate at a higher peak pressure without knocking.



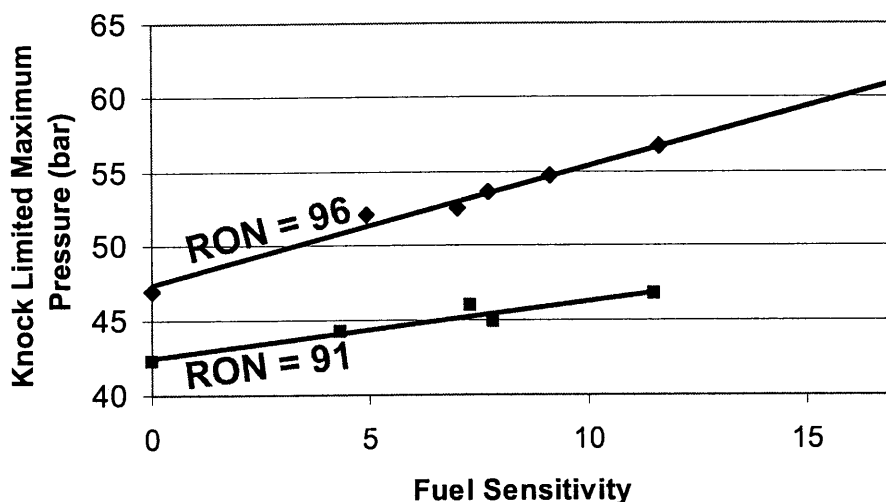
**Figure 5.1: The OI plotted against fuel sensitivity for both fuel sets. The operating conditions are those listed in Table 5.1. The plot clearly shows that the OI increases with fuel sensitivity, and that K is independent of RON and MON.**



**Figure 5.2:** The knock limited spark timing plotted against fuel sensitivity for both fuel sets. The operating conditions are those listed in Table 5.1. For both fuel sets, the more sensitive fuels can operate at earlier spark timings than the less sensitive, for a fixed RON.



**Figure 5.3:** The peak pressure plotted against spark timing at the base operating conditions (Table 5.1). These values were calculated by measuring the peak pressure over a range of spark timings with PRF105, which avoids knock at the advanced spark timings.



**Figure 5.4: Knock Limited Maximum Pressure vs Fuel Sensitivity for both fuel sets at the base operating conditions (Table 5.1). This plot shows that for a fixed RON, a more sensitive fuel can operate at a higher maximum pressure.**

It should be noted that the most sensitive fuel in the RON91 fuel set has the same maximum operating pressure as the least sensitive fuel in the RON96 fuel set. Hence, a fuel with an  $(R+M)/2$  of 85 has the same antiknock performance as a fuel with an  $(R+M)/2$  of 96.

The data clearly shows that for a fixed RON, fuels with a higher sensitivity have better anti-knock performance at this condition. It should be noted that the test fuels contained very different chemicals. These chemicals include iso-octane (paraffin), toluene (aromatic), diisobutylene (olefin), and ethanol (alcohol). Further the test fuels included UTG91 and UTG96 which are blends of numerous different chemicals. This trend appears independent of the differences in the chemistry of the fuel, and relies solely on the fuel sensitivity.

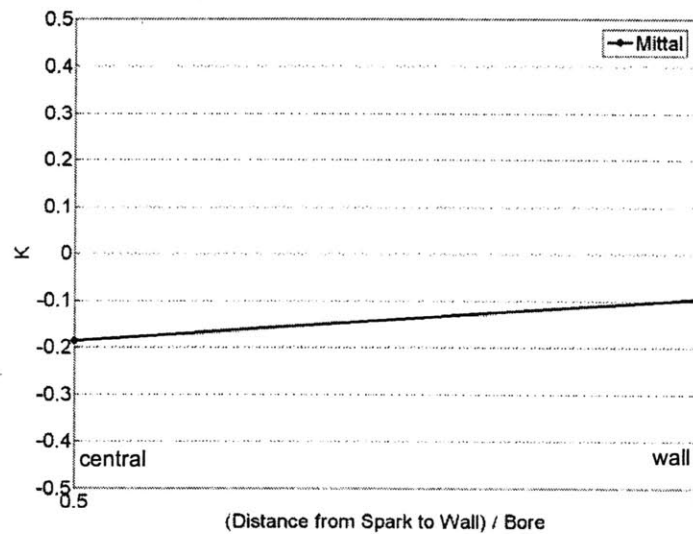
#### **5.1.4 THE DEPENDENCE OF K ON DIFFERENT PARAMETERS**

Knock depends on several engine operating and design parameters. Engines are designed to maximize efficiency while avoiding knock. Accordingly, the spark location and the compression ratio are crucial design parameters. The operating parameters important for avoiding knock include the relative air/fuel ratio, the engine speed, the intake air temperature, and the intake air

pressure. Experiments were performed to determine how  $K$  depends on each of these parameters, as detailed in Section 5.2.1.

#### 5.1.4.1 SPARK LOCATION

The schematic in Appendix A shows that a spark plug for a CFR Engine is located on the cylinder wall. However, most modern engines have spark plugs that are located at the apex of a pent-roof in the center of the chamber. Therefore, the OI was measured at the base test conditions with the side spark and with the central spark.  $K$  was then determined from the OI and the respective fuel RON and MON. Figure 5.5 shows the relationship between  $K$  and the spark location.



**Figure 5.5:  $K$  as a function of the spark location. The spark plug was moved from the center to the side-wall. All other test conditions are those given in Table 5.1.**

The spark location plays an important role in the flame development and burn rate. The side spark has a burn duration (defined as 10% – 90% mfb) of 20 CAD. The central spark has a burn duration of approximately 12 CAD. The experiments showed that the longer burn time (i.e. more time for autoignition) is offset by the lower pressures inherent with longer burn times.



The change in spark location and burn time has only a modest effect on K. At the central spark location, K is -0.18. At the side spark location, K is -0.10. K is not significantly dependent on the spark location. Hence, it can be assumed that the discrepancy in spark location between the CFR Engine and modern engines plays a minor role in why K is negative.

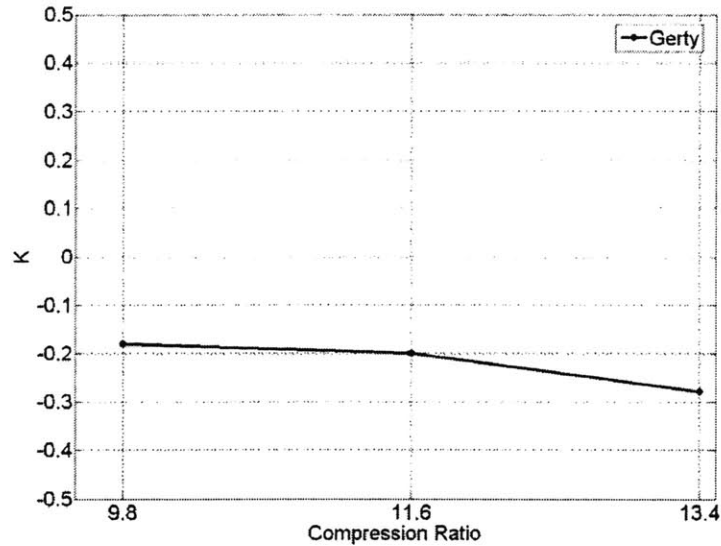
#### **5.1.4.2 COMPRESSION RATIO**

The parameter K is expected to be independent of the RON and MON of the fuel, only depending on the engine operating conditions. At the RON conditions, K is by definition 0, and at the MON conditions, K is 1, regardless of the actual RON and MON values. Since the RON and MON values are determined by changing the compression ratio of the engine, K should ideally be independent of compression ratio.

The compression ratios for the RON and MON tests are lower than what modern engines use. The RON90 and MON90 tests have compression ratios of 6.64 and 6.76, respectively. However, the average compression ratio for a 2008 engine is 9.8.

The OI was measured at the base set of test conditions with varying compression ratios. These experiments were conducted in 2004 by Gerty [38] on the same test engine. The compression ratios were increased by using pistons with different head geometries. The results are shown in Figure 5.6. There is a weak dependence of K on the compression ratio. As the compression ratio increases from 9.8 to 11.6 to 13.4, K decreases from -0.17 to -0.20 to -0.28. This decreasing trend of K with increasing compression ratio is also seen in literature [12,39].

This relationship is weak, thus K is essentially independent of compression ratio. This finding does not agree with those presented in a study by Kalghatgi [12,39]. This discrepancy could be caused from a differing methodology for measuring the OI. This study determined the OI by directly comparing its knock limited spark advance to that of a PRF at the same condition, which differs from the methodology in [12,39]. The tests show that a change in compression ratio resulted in approximately the same change in knock limited spark advance for a PRF as it did in any test fuel. Hence, the compression ratio did not have a large effect on K.



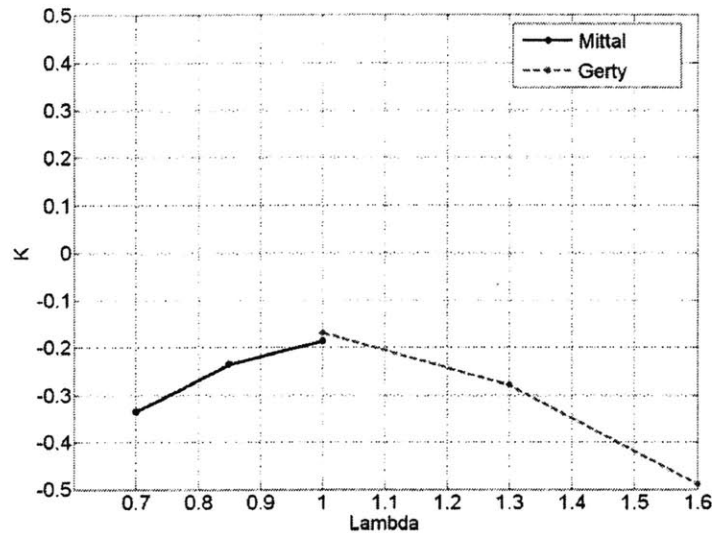
**Figure 5.6: K as a function of compression ratio. The pistons were changed to increase the compression ratio. All other test conditions are those given in Table 5.1.**

#### 5.1.4.3 RELATIVE AIR/FUEL RATIO

The relative air-fuel ratio is not actually measured in the RON and MON tests. The test procedures state that the air/fuel ratio is adjusted to maximize the knock intensity. Maximum knock tends to occur close to stoichiometric at a  $\lambda$  of about 0.95 [3,35]. For the most part, modern engines tend to run stoichiometric due to requirements of three-way catalysts. However, at high loads, the engine tends to run at  $\lambda \approx 0.75$  to avoid knock.

Figure 5.7 shows how K depends on the relative air-fuel ratio. The data set includes experiments conducted for this analysis, and experiments conducted on the same engine by Gerty [38]. The value of K is highest at stoichiometric, which was also noted by Kalghatgi [12].

Though K does depend on  $\lambda$ , especially at very lean conditions, modern engines seldom operate lean. Additionally, engines do not usually operate below values of  $\lambda = 0.75$ . Over the practical  $\lambda$  operating range, K changes from -0.18 at stoichiometric to approximately -0.3 at  $\lambda = 0.75$ .



**Figure 5.7: K as a function of  $\lambda$ . The results presented are both from this study and from a study by Gerty [38]. Though the results show a strong dependence, it should be noted that for typical engines, the practical operating range is between  $\lambda = 0.75$  and 1.**

#### 5.1.4.4 ENGINE SPEED

The RON and MON tests operate at speeds of 600 rpm and 900 rpm, respectively. Therefore, engine speed should play a key role in a fuel's sensitivity. It should be noted that these speeds are lower than the speeds at which modern engines operate. While engines idle at about 600 rpm, high load operation is rare at engine speeds below 1200 rpm. Due to increased turbulence and correspondingly reduced flame travel time, knock is not usually an issue above 2500 rpm.

The results, which are presented in Figure 5.8, show that K has a strong dependence on engine speed. At a speed of 1200 rpm, K is -0.48; as the speed increases to 2500 rpm, K is 0.08.

This trend follows what is expected from the RON and MON tests. The RON test with an engine speed of 600 has a value of  $K = 0$ . The MON test with an engine speed of 900 has a value of  $K = 1$ . Therefore, K should increase with engine speed, as is shown by these experimental results. This trend is also clearly shown throughout literature [12,39,40].

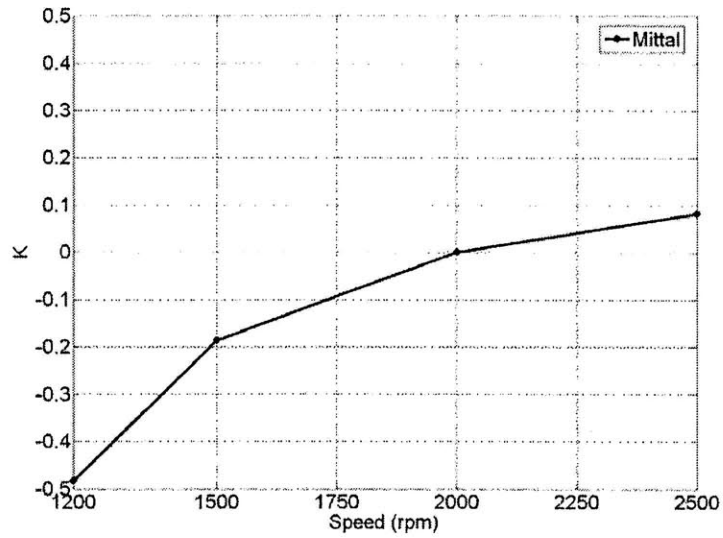


Figure 5.8: K as a function of engine speed. The results show a strong dependence K and engine speed.

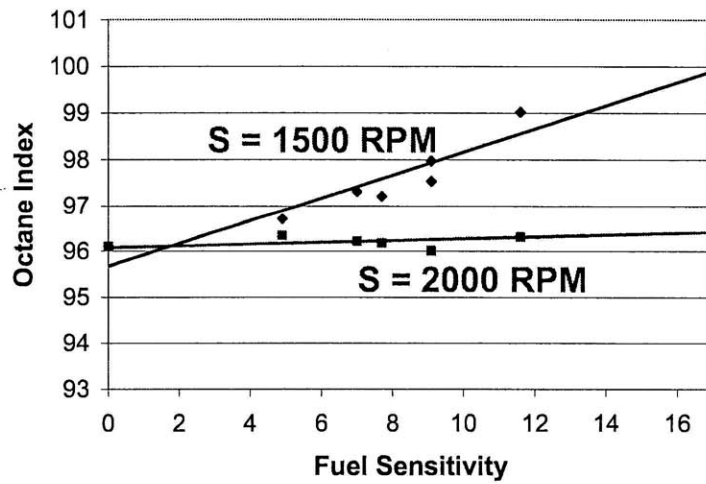


Figure 5.9: OI plotted against fuel sensitivity for engine speeds of 1500 rpm and 2000 rpm for fuel set 1. It should be noted that the slope of the trend line decreases as the speed increases.

Figure 5.9 plots the OI for the individual fuels for 1500 rpm and 2000 rpm. At a speed of 2000 rpm, the OI appears to be independent of sensitivity. This occurs because at this speed,  $K = 0$ . As the speed decreases, the OI increases linearly with sensitivity due to  $K$  being negative.

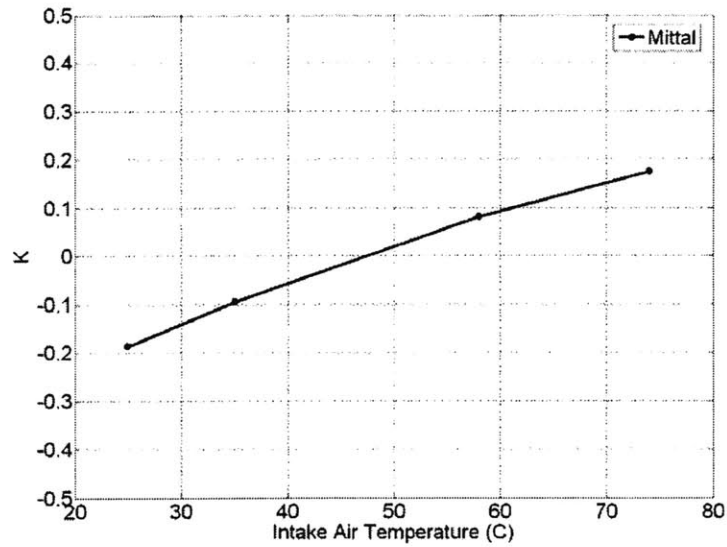
#### 5.1.4.5 INTAKE AIR TEMPERATURE

Perhaps the largest difference between the RON and MON tests is the intake air temperature. The RON test has an intake air temperature of  $52^{\circ}\text{C}$ , while the MON test has an intake air temperature of  $149^{\circ}\text{C}$ . The tests operate at high temperatures to compensate for the poor cooling systems of on-the-road engines in 1928. Additionally, the use of carburetors required some heating of the intake air. Modern engines use fuel injectors, so heating the intake air is not necessary and the intake air temperature is maintained at about ambient. Additionally, the cooling systems on modern cars are more effective than those in the CFR engine.

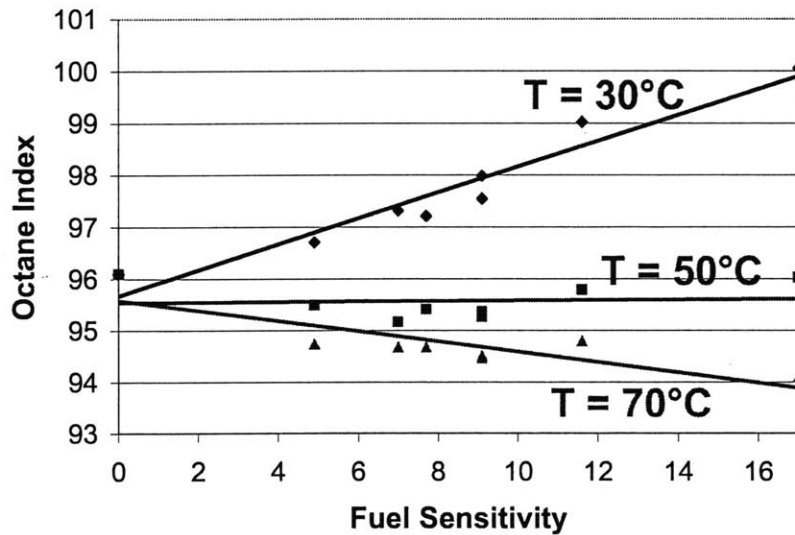
The OI was measured at a variety of intake air temperatures ranging from  $25^{\circ}\text{C}$  to  $74^{\circ}\text{C}$ . The results are presented in Figure 5.10, which shows a linear relationship between  $K$  and the intake air temperature.  $K$  increases from  $-0.18$  to  $0.18$  as the intake air temperature is increased by  $49^{\circ}\text{C}$ .

The RON and MON tests show a similar trend. As the intake air temperature is increased from  $52^{\circ}\text{C}$  to  $149^{\circ}\text{C}$ ,  $K$  increases from  $0$  (RON) to  $1$  (MON). Therefore,  $K$  should increase with the intake air temperature, as is shown from these experimental results.

Figure 5.11 plots the OI for the individual fuels for 3 different intake air temperatures. At an intake air temperature of  $30^{\circ}\text{C}$ , the OI increases linearly with fuel sensitivity. This trend implies that at typical intake air temperatures, fuels with a higher sensitivity, but a fixed RON, have better anti-knock performance. At these conditions, the OI is greater than that predicted by the RON or MON tests, showing that the RON and MON tests do not adequately bracket the knock limited region for modern engine intake temperatures.



**Figure 5.10: K as a function of intake air temperature. The results show a very linear relationship between K and intake air temperature**



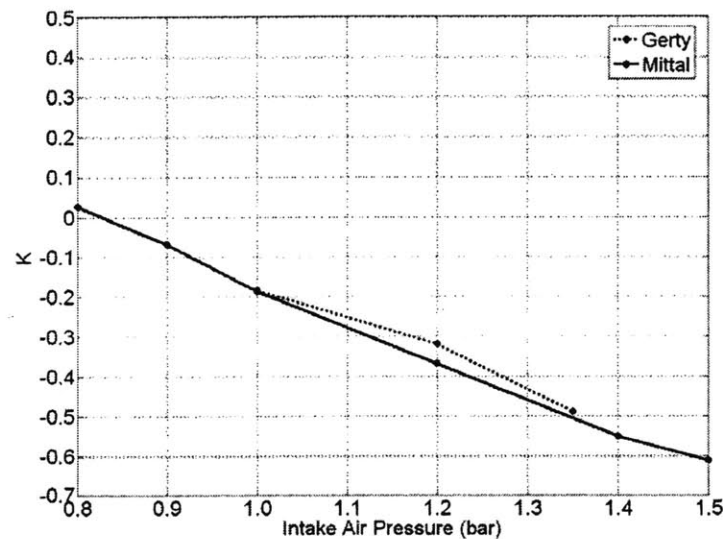
**Figure 5.11: OI plotted against fuel sensitivity for intake air temperatures of 30°C, 50°C, and 70°C for fuel set 1. It should be noted that the slope of the trend line decreases as the temperature increases.**

As the intake air temperature is increased to 50°C, the OI is independent of sensitivity. This trend occurs because at this intake air temperature,  $K = 0$ . At an intake air temperature of 70°C,

the OI decreases linearly with sensitivity due to  $K$  being positive. This trend corresponds to what the RON and MON tests would predict. Since the RON is fixed, a higher sensitivity implies a lower MON, which theoretically relates to worse anti-knock performance. At this temperature, the RON and MON values bracket the OI.

#### 5.1.4.6 INTAKE AIR PRESSURE

The MON and RON tests run unthrottled. Leppard [18] states that the MON test has a slightly lower intake air pressure because of higher throttling losses due to higher speeds. The WAVE models of the engine found that these differences are minimal, so the RON and MON tests have essentially the same intake air pressure. Therefore,  $K$  should be independent of intake air pressure.

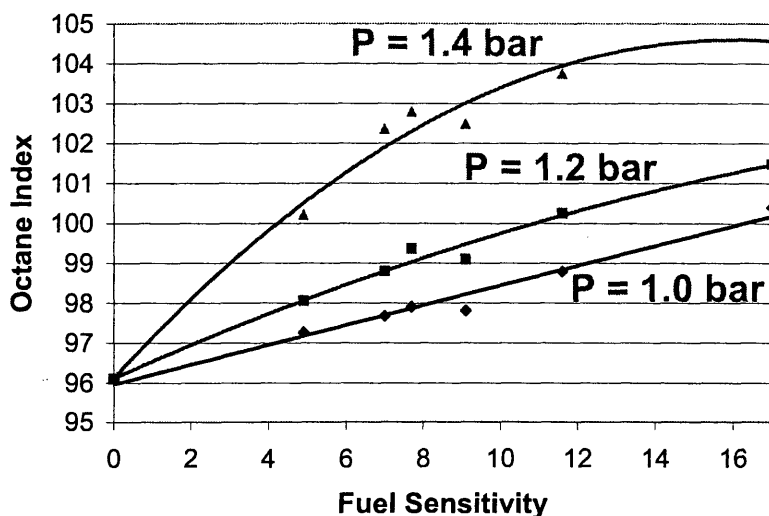


**Figure 5.12:  $K$  as a function of boosting percentage. The results presented are both from this study and from a study by Gerty [38]. The results show that as the intake air pressure increases,  $K$  becomes more negative**

However, modern engines are moving towards boosting with inter-coolers. In such engines, the intake air pressure is higher than those in the RON and MON tests. Experiments were conducted to determine the relationship between  $K$  and boosting. The results are combined with the

experiments conducted by Gerty [38] and presented in Figure 5.12. At an intake air pressure of 1.5 bar, the transition into heavy knock is rapid, increasing the chances of engine damage. Therefore, tests were not conducted at higher boost levels.

Figure 5.12 shows that as the amount of boosting increases,  $K$  becomes more negative. As the engine is boosted to an intake air pressure of 1.5 bar,  $K$  is approximately -0.6, as compared to -0.2 at WOT. Figure 5.13 plots the OI for the individual fuels for 3 different boosting pressures. The relationship between OI and sensitivity is linear for intake air pressures of 1 bar and 1.2 bar. This follows from  $K$  being independent of RON and MON. However, at 1.4 bar, this relationship is not linear, which suggests that at these pressures, the OI cannot be accurately extrapolated from RON and MON.



**Figure 5.13: OI plotted against fuel sensitivity for intake air pressures of 1 bar (WOT), 1.2 bar, and 1.4 bar for fuel set 1. The linear relationship between OI and sensitivity is not present at higher boosting levels.**

### 5.1.5 SUMMARY

This section shows that of the different engine operating parameters,  $K$  appears to be almost independent of compression ratio and spark location.  $K$  has a slight dependence on  $\lambda$ , which gets



greatly amplified at very rich and very lean operating conditions.  $K$  depends very strongly on engine speed, intake air temperature, and intake air pressure.

Additionally, the tests show that over the range of tested operating conditions,  $K$  is usually negative, between 0.2 and -0.5.  $K$  never reaches the value of 0.5, corresponding to the  $(R+M)/2$  value shown on retail gasoline dispensers. It can therefore be concluded that the knock-limited operating range of modern engines is outside of the range bracketed by the RON and MON tests.

The engine operating parameter that mostly clearly shows this trend is the intake air temperature. The intake air temperature of modern engines is lower than those used in the RON and MON tests. As the intake air temperature is increased,  $K$  also increases. As the intake air temperature approaches the RON intake air temperature ( $53^{\circ}\text{C}$ ),  $K$  becomes positive. At intake air temperatures above  $53^{\circ}\text{C}$ , the fuel behaves similarly to how it behaves in an octane test.

## **5.2 WAVE MODELS AND CHEMICAL SIMULATIONS**

Engine simulations were performed in WAVE with the model of the test engine detailed in Section 2.2. These simulations were used to generate pressure and end-gas temperature traces at different spark timings for different conditions. The intake air conditions chosen for these simulations are given in Table 5.4 and correspond to the experiments performed in the previous section. The models were validated at each spark timing by comparing the pressure traces to experimental pressure traces. These pressure and temperature traces were used in the chemical models detailed in Section 2.3 to determine the knock-limited spark advance for the fuel blends of iso-octane, n-heptane, toluene, and ethanol detailed in Tables 5.2 and 5.3.

Figures 5.14 and 5.15 plot the OI against fuel sensitivity for the experimental results (left) and chemical modeling results (right) for the RON96 fuels at different intake air temperatures and intake air pressures. Figures 5.16 and 5.17 display the similar plots for the RON91 fuels.

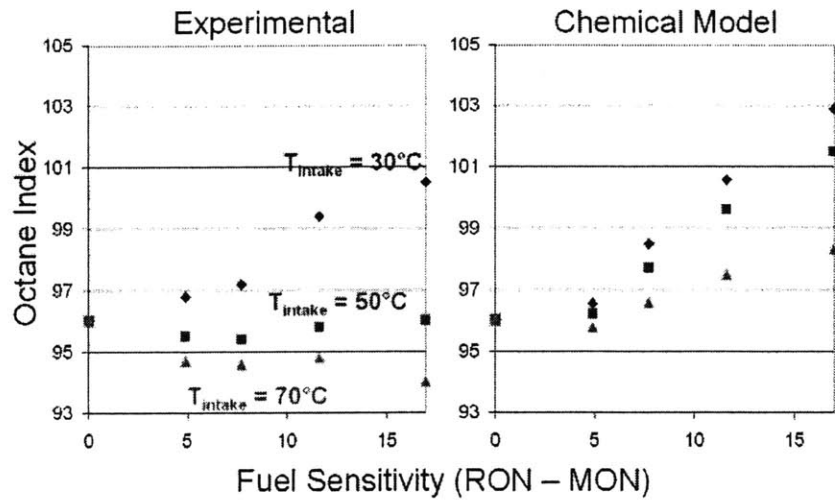
$T_{\text{intake}} (^{\circ}\text{C})$	$P_{\text{intake}} (\text{bar})$
30	1.0
50	1.0
70	1.0
30	1.2
30	1.4

**Table 5.4: The intake air conditions for the engine simulations used for the chemical models.**

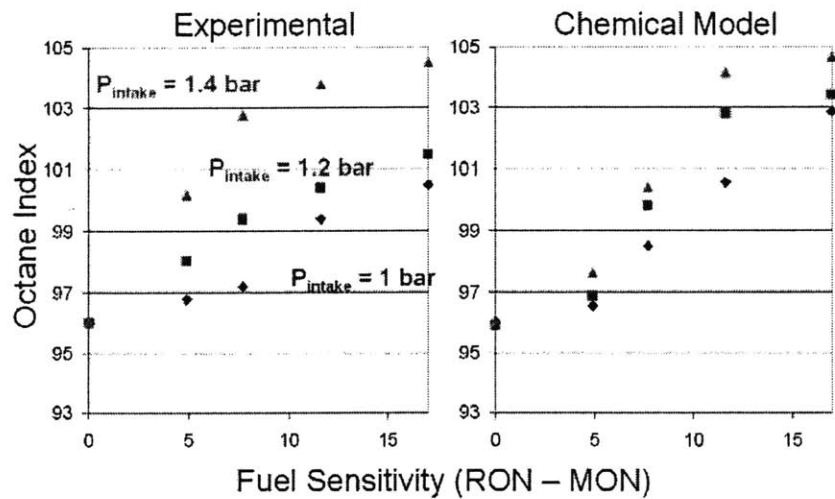
Though the values of the OI determined by the chemical models did not match the experimental values, the trends matched. The chemical models found that at the base test condition, more sensitive fuels have better anti-knock performance than less sensitive fuels. This trend can be observed through the positive slope of the OI vs S curve; the slope of the line corresponds to values of  $-K$ . As the intake air temperature increases, the chemical models found that the slope decreases, corresponding to an increase of  $K$ . Similarly, as the intake air pressure increases, the chemical models found that  $K$  increases.

The WAVE models coupled with chemical kinetics generate a significant amount of error in the calculations. The chemical models have a significant amount of uncertainty already built into the mechanisms. Further, the end-gas temperatures predicted by WAVE assume isentropic compression with a certain amount of heat loss. This model for the end-gas temperature is an approximation and hence carries a large amount of uncertainty.

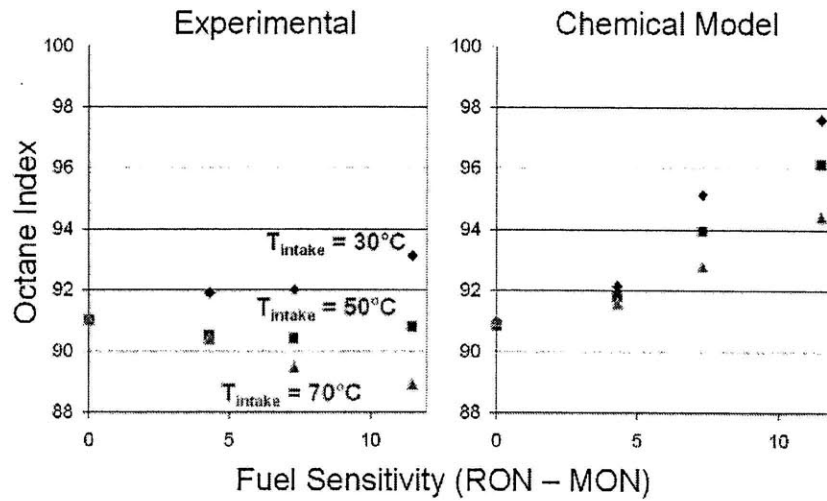
The experimental research in the previous section showed that  $K$  is negative and hence for a fixed RON, fuels with a lower MON have better antiknock performance. Despite their large uncertainty, the chemical models also show this trend. Therefore, this trend can be explained by looking at the underlying chemical kinetics, which will be explored in Chapter 6.



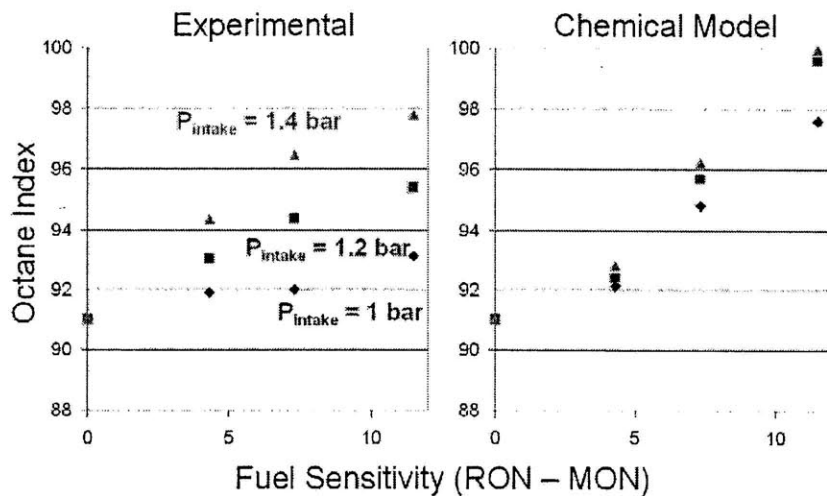
**Figure 5.14:** The OI of a fuel as a function of fuel sensitivity at different intake air temperatures, as found through the experiments (left) and chemical models (right). These plots are for 5 fuels with RONs of 96, but sensitivities varying from 0 to 17.



**Figure 5.15:** The OI of a fuel as a function of fuel sensitivity at different intake air pressures, as found through the experiments (left) and chemical models (right). These plots are for 5 fuels with RONs of 96, but sensitivities varying from 0 to 17.



**Figure 5.16:** The OI of a fuel as a function of fuel sensitivity at different intake air temperatures, as found through the experiments (left) and chemical models (right). These plots are for 4 fuels with RONs of 91, but sensitivities varying from 0 to 12.



**Figure 5.17:** The OI of a fuel as a function of fuel sensitivity at different intake air pressures, as found through the experiments (left) and chemical models (right). These plots are for 4 fuels with RONs of 91, but sensitivities varying from 0 to 12.

### 5.3 CORRELATING K WITH KEY ENGINE OPERATING CONDITIONS

The results in the previous section show that K depends on intake air temperature, engine speed, intake air pressure, and the relative air-fuel ratio. A Response Surface Methodology study was conducted with these variables following the methodology outlined in [41]. The initial results showed that the dependence on  $\lambda$  was an order below that of the other tests. Therefore, the study was redone without  $\lambda$ , in order to decrease the complexity of the analysis.

The data set used for this study includes the data presented in the previous section, the data collected by Gerty [38], and the RON and MON tests. The data set included many different tests, including 14 different fuels. The engine speed includes values from 1200 to 2500 rpm. The intake air temperature was varied from 25°C to 74°C. The intake air pressure varies from WOT to 50% boost. Additionally, the relative air/fuel ratio is within 25% of stoichiometric (the extremely lean and rich conditions were not included). Three different compression ratios and two different spark locations were also used. Altogether, this study included over 100 different sample points.

The dependent variables—engine speed, intake air pressure, and intake air temperature—were each normalized to be between -1 and 1. These normalized variables are denoted as T (intake air temperature), P (intake air pressure), and N (engine speed). K did not need to be normalized because it already spanned the range of -1 and 1. These normalized values were then entered into matrices of the form:

$$\begin{bmatrix} \dots \\ \mathbf{K} \\ \dots \end{bmatrix} = \begin{bmatrix} x_1 \\ x_2 \\ \dots \\ x_8 \end{bmatrix} \begin{bmatrix} c & T & P & N & TP & TN & NP & TNP \\ & & & & \dots & & & \\ & & & & & \dots & & \end{bmatrix} \quad (\text{Eq. 5.2})$$

where c is a constant. The variables TP, TN, NP, and TNP denote the products of different combinations of T, N, and P. Equation 5.2 is then solved for the x-matrix using a least-squares fit. The results are shown in Figure 5.18. The value of each term in the x-matrix shows how much K depends on the corresponding variable. For example, the small value of  $x_3$  relative to

the other terms indicates a weak relationship between K and the intake air pressure. However, the intake air pressure coupled with engine speed ( $x_7$ ) has a large contribution to K.

Figure 5.18 shows that K has a strong dependence on temperature ( $x_2$ ); speed ( $x_4$ ); the product of temperature and speed ( $x_6$ ); the product of speed and pressure ( $x_7$ ); and the product of temperature, speed, and pressure ( $x_8$ ).

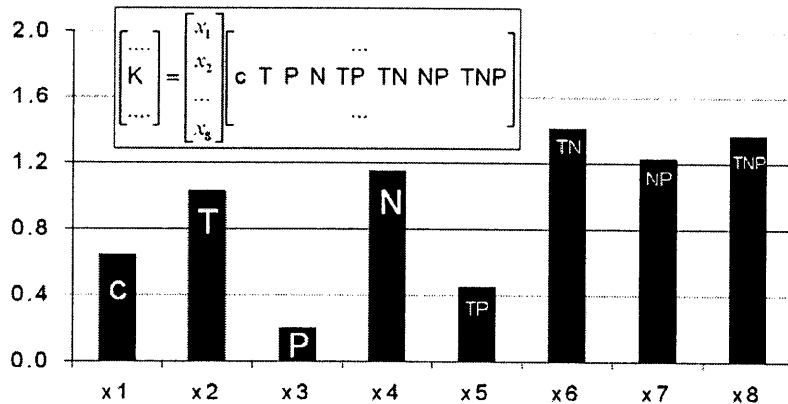


Figure 5.18: Coefficients of the variables in the response surface methodology.

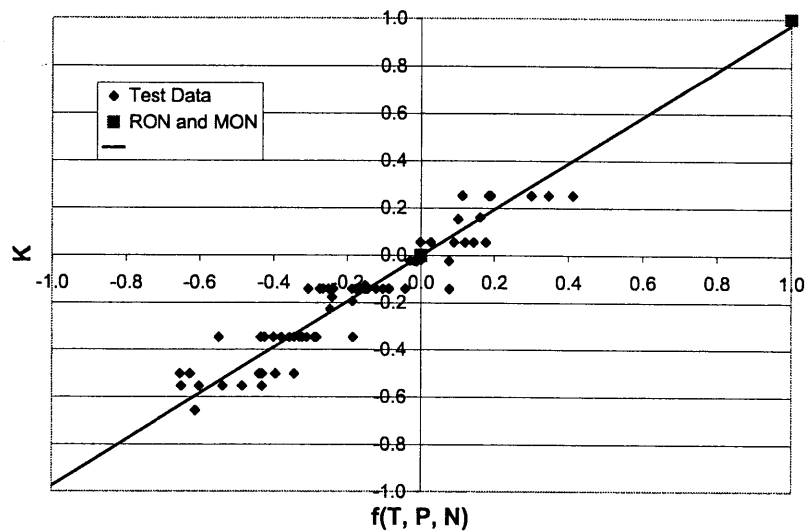


Figure 5.19: Response Surface Methodology curve fit. The methodology determines the least squares approximation of K as a function of temperature, pressure, and speed.

The predicted values of K from the least-squares fit for the x-matrix in Equation 2 are plotted against the experimental values in Figure 5.19. The predicted values of K are within 0.05 of the measured value.

#### 5.4 CORRELATING K WITH FUNDAMENTAL ENGINE PARAMETERS

The trends found in the previous section gives that K increases with increasing intake air temperature, increasing engine speed, and decreasing intake air pressure. The maximum end-gas temperature also follows the same trends as K, as explained by the autoignition integral:

$$\begin{aligned}
 \int_0^{t_{ignite}} \frac{1}{\tau} dt &= 1 \\
 \rightarrow c_1 \int_{\theta_{IVC}}^{\theta_{autoignite}} \frac{1}{N\tau} d\theta &= c_1 \int_{\theta_{IVC}}^{\theta_{autoignite}} \frac{P^{c_2}}{N \exp(c_3/T)} d\theta = 1 \\
 \rightarrow c_1 \int_{\theta_{IVC}}^{\theta_{autoignite}} \frac{P^{c_2}}{N \exp(c_3/T)} d\theta &= 1
 \end{aligned} \tag{Eq. 5.3}$$

and from the polytropic relationship:

$$T = T_0 \left( \frac{P}{P_0} \right)^{(\gamma-1)/\gamma} \tag{Eq. 5.4}$$

As the intake air temperature increases, the maximum end-gas temperature would also increase. As engine speed increases, Equation 5.3 gives that the engine must operate at higher pressures and temperatures for autoignition to occur. Therefore, the maximum end-gas temperature would increase. Equation 5.4 gives that an increase in the intake air pressure, which causes the engine to operate at higher pressures, will have a lower end-gas temperature at autoignition.

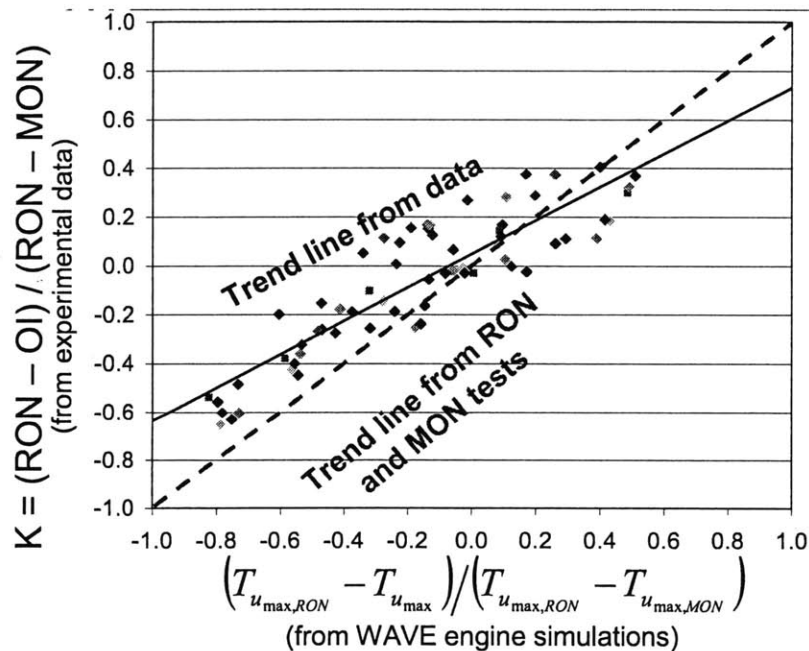
The end-gas temperature was normalized to have the same form of K:

$$\left( T_{u_{max, RON}} - T_{u_{max}} \right) / \left( T_{u_{max, RON}} - T_{u_{max, MON}} \right)$$

and plotted against K in Figure 5.20. The end-gas temperatures were calculated through WAVE simulations and the K values were measured in the experiments detailed earlier in this chapter.

The red dashed line in the figure corresponds to the expected trend from the normalization used for the end-gas temperature. This line would go through (0,0) and (1,1) corresponding to the points of the RON and MON tests. The black line corresponds to the trend line from the data. Though the measured trend line does not match the expected trend line, a definite trend clearly exists. This trend gives that K relates the maximum end-gas temperatures in the engine to those of the RON and MON test.

The discrepancies between the two trendlines in Figure 5.20 comes from the systematic error built into the tests coupled with the error in WAVE approximations. The end-gas temperatures are unknown and cannot be measured directly. The approximations assume adiabatic compression with a certain amount of heat transfer. However, the error in these values can be substantial.



**Figure 5.20: K, as measured from experimental data, plotted against a normalized end-gas temperature, calculated from WAVE). The red dashed line corresponds to the expected trend based off the normalizations used, and the black line corresponds to the trend from the data.**



## 5.5 CONCLUSIONS

This analysis on how K relates to different engine parameters found that:

- When the octane tests were first established, K was believed to be between 0 and 1, values corresponding to the RON and MON tests respectively. However, experimental results and chemical models both showed that in modern engines, K is typically between -0.75 and 0.25.
- K was found to be strongly dependent on intake air temperature, engine speed, and intake air pressure. These trends agreed with the results from chemical kinetic models. Though K depends on the relative air-fuel ratio, this relationship is weak over the practical operating range. K was also found to have a weak dependence on compression ratio and spark plug location.
- A Response Surface Methodology was used to determine how K relates to intake air temperature, engine speed, and intake air pressure.
- The experimental data showed that K relates the maximum end-gas temperatures in the engine to those of the RON and MON tests.

(this page intentionally left blank)

## CHAPTER 6: FUNDAMENTALS OF FUEL SENSITIVITY


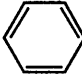
Studying the chemical kinetics of fuels provides valuable insight into the autoignition process. In particular, it allows for the comparison of different fuels to determine why certain fuels have higher sensitivities than other fuels. Therefore, chemical kinetic models were used to relate fuel sensitivity to the autoignition delay time and to chemical intermediates

### 6.1 PROPERTIES OF INDIVIDUAL FUEL COMPONENTS

#### 6.1.1 CHEMICAL BOND ENERGIES

The first step in the autoignition process is typically the extraction of a hydrogen atom from the hydrocarbon chain, since a C-H bond is much weaker than a C-C bond. However, certain hydrogen atoms on the hydrocarbon chain are more prone to be extracted than others. The bond between a hydrogen atom and a primary carbon ( $\text{RCH}_3$ ) is the hardest C-H bond to break. These hydrogens, termed as primary hydrogens, are found in methyl groups. Secondary hydrogens, which are bonded to a secondary carbon ( $\text{RCH}_2$ ), are easier to break. Finally, tertiary hydrogens, those that are bonded to tertiary carbons ( $\text{RCH}$ ), are the easiest to break. This trend comes from the strong bonds between carbons atoms; as the number of C-C bonds increase, the strength of the corresponding C-H bonds decrease.

The amount of energy required to break the bond at  $25^\circ\text{C}$  is called the bond dissociation energy. The bond dissociation energy provides insight into the autoignition resistance of the different fuel molecules used in these chemical models. Table 6.1 gives the bond energies for the relevant bonds in hydrocarbon combustion [42]. It should be noted that these bond energies are not necessarily relevant to engine combustion since they relate to the dissociation of molecules at  $25^\circ\text{C}$ . However, these values show the general trend that primary hydrogens are more difficult to extract than secondary hydrogens.

$\text{RCH}_2 - \text{H}$	: 420 kJ/mol
$\text{RCH} - \text{H}$	: 401 kJ/mol
$\text{RC} - \text{H}$	: 390 kJ/mol
$\text{RCH}_2 - \text{OH}$	: 380 kJ/mol
$\text{RCH}_2\text{O} - \text{H}$	: 436 kJ/mol
 -H	: 464 kJ/mol
 -CH <sub>2</sub> -H	: 368 kJ/mol

**Table 6.1: Bond dissociation energies of different bonds common in hydrocarbon fuels [42]**

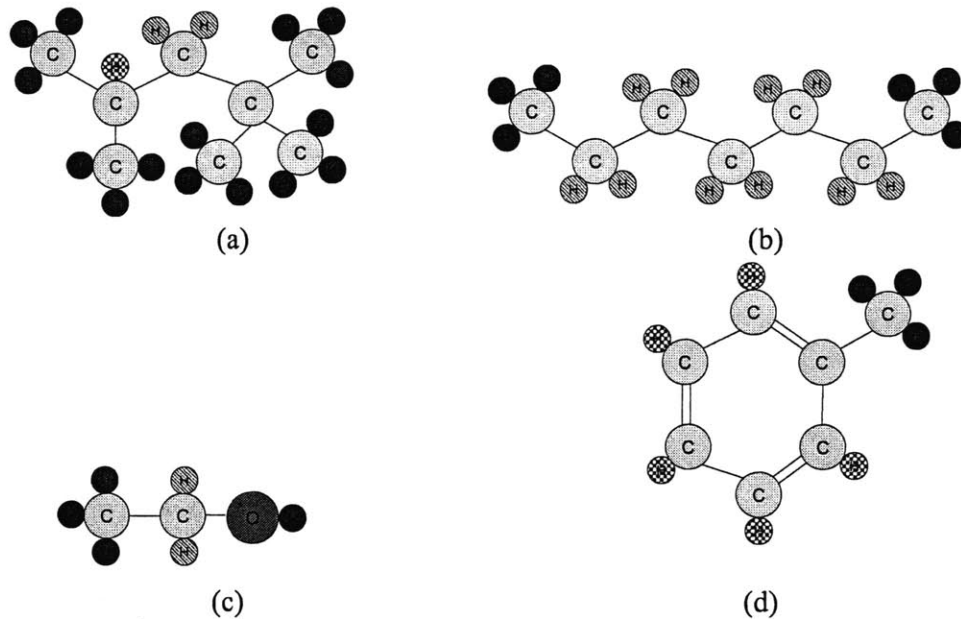
The fuels used in this study are taken from the lists of fuels used in the experiments in Chapter 5. However, only the fuel with detailed chemical kinetic models could be used for this study, and hence the blends of iso-octane, n-heptane, toluene, and ethanol were used.

Figure 6.1a shows the chemical structure of iso-octane ( $\text{C}_8\text{H}_{18}$ ). Iso-octane has a RON and MON of 100, corresponding to good antiknock properties. The chemical structure shows that iso-octane is composed of five methyl groups with fifteen primary hydrogens. The fuel molecule only has two secondary hydrogens and one tertiary hydrogen. In a simplistic view, the large number of primary hydrogens makes it difficult to extract hydrogens from an iso-octane molecule, hence the high octane number. This trend is complicated by the presence of a tertiary hydrogen and will be addressed in a later section.

On the other hand, n-heptane ( $\text{C}_7\text{H}_{16}$ ) has poor antiknock performance with a RON and MON value of 0. The chemical structure, displayed in Figure 6.1b, consists of six primary hydrogens and ten secondary hydrogens. The numerous secondary hydrogen bonds are readily broken, hence causing n-heptane to have a low octane number.

The chemical structures for ethanol ( $\text{C}_2\text{H}_5\text{OH}$ ) and toluene ( $\text{C}_6\text{H}_5\text{CH}_3$ ) are given in Figure 6.1c and 1d. The addition of oxygen, double bonds, and ring structures into the hydrocarbon chain complicates the fuel chemistry. For ethanol ( $\text{C}_2\text{H}_5\text{OH}$ ), the weakest bond is the C-O bond, which

causes the corresponding to C-H bond to have a higher bond energy. The double bonds of the aromatic toluene also complicate the fuel chemistry. The second bond in each double bond is a  $\pi$  bond, which is weak; thus a double bond has less bond energy than twice that of a single bond. Therefore, these carbons have a stronger bond with the hydrogens and methyl groups attached to it. Also, the carbon in toluene's methyl group has a weaker bond with its hydrogens, which are therefore the first to be extracted.

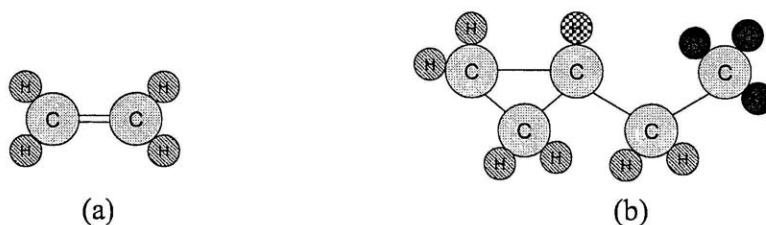


**Figure 6.1: Chemical structures of (a) iso-octane, (b) n-heptane, (c) ethanol, and (d) toluene**

### 6.1.2 MOLECULAR STRUCTURE OF HIGHER SENSITIVITY MOLECULES

The RON and MON tests were designed such that blends of iso-octane and n-heptane would have no sensitivity; since iso-octane and n-heptane are paraffins, other paraffins should have a low sensitivity. Appendix B gives a list of pure hydrocarbons with their corresponding RON and MON values [40]. The table indeed shows that the low-sensitivity fuels tend to be paraffins, while the higher sensitivity fuels tend to be olefins, aromatics, diolefins, and naphthenes. Alcohols, which are not listed in Appendix B, also tend to have higher sensitivities. For example, ethanol has a sensitivity of 21 and methanol has a sensitivity of 30 [40].

A more exact relationship between sensitivity and the fuel's chemical structure is not apparent. High sensitivity fuels can have vastly different chemical structures. For example, ethylene and ethylcyclopropane have similar RON, MON, and sensitivity values. However, they have very different chemical structures as shown in Figure 6.2. While ethylene is a two carbon chain connected by a double bond, ethylcyclopropane has a ring structure and no double bonds. Regardless, the two hydrocarbons both have a sensitivity of 20, which indicates that a fuel's sensitivity does not necessarily relate to the fuel's molecular structure. However, most fuels with high sensitivities have complex structures when compared to that of branching paraffins.



**Figure 6.2: Chemical structures of (a) ethane and (b) ethylcyclopropane.**

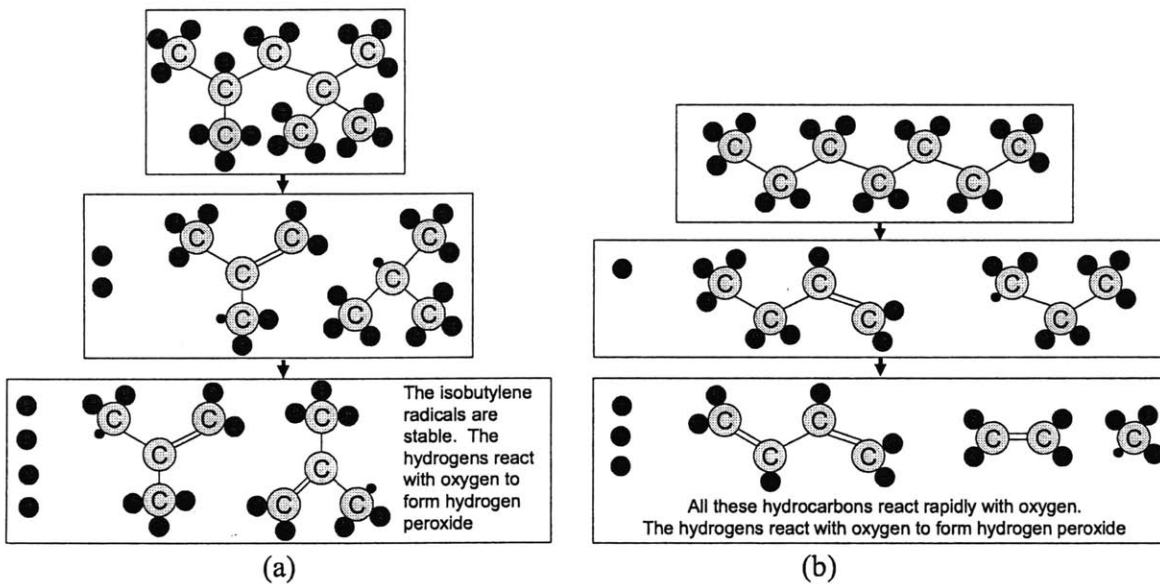
### 6.1.3 INITIAL CHEMICAL STRUCTURE VS INTERMEDIATES

The previous section shows that the initial structure of the fuel molecule only has a weak relationship with the fuel's sensitivity. This weak relationship occurs because the molecular structures of the intermediates in a chemical process are more important than the initial chemical structure. For example, iso-octane has a tertiary hydrogen which can be readily extracted. However, it is less likely to autoignite than n-heptane, which only has secondary and primary hydrogens. This discrepancy can be explained through looking at how the two fuel molecules break down into intermediates.

Iso-octane follows the chemical pathway shown in Figure 6.3a. The intermediate hydrocarbons for iso-octane are non-reactive; however, the reaction moves forward slowly because the hydrogen radicals bond with oxygen and forms hydrogen peroxide. When a critical amount of hydrogen peroxide is formed, it dissociates into hydroxyl radicals releasing large amounts of chemical energy.

N-heptane follows the pathway in Figure 6.3b and breaks up into ethylene, 1-3 butadiene, and a methyl group, as well as hydrogens. All three of these hydrocarbons are reactive with oxygen, causing a degenerative branching process. Meanwhile, the hydrogen atoms are forming hydrogen peroxide similar to the iso-octane molecule.

Even though iso-octane's initial chemical structure is less stable than n-heptanes, iso-octane's intermediates are more stable than n-heptane's intermediates. This example serves to illustrate the initial chemical structure of a fuel molecule can be deceiving.



**Figure 6.3: The chemical reduction mechanisms for (a) iso-octane and (b) n-heptane. The products for iso-octane include two radicals that are resonance forms of each other and four hydrogens. The hydrogens form hydrogen peroxide. The products for n-heptane include three hydrocarbons that are reactive with oxygen, as well as hydrogens that form hydrogen peroxide.**

## 6.2 EFFECTS OF TEMPERATURE ON FUEL CHEMISTRY

In the equation,  $OI = RON - K \times S$ , the value  $K \times S$  gives the difference between the OI and the RON. Chapter 5 found that the parameter  $K$  correlates the end-gas temperatures in an engine to

that of the RON and MON test. It follows that the fuel sensitivity should capture how a given fuel will respond to these changes in temperature.

### 6.2.1 ENGINE MODELS

The RON96 test was modeled in WAVE, and the end-gas pressure and temperature profiles were validated against those given in literature [39]. The model was then rerun at different intake air temperatures, ranging from 5°C to 155°C in 10°C increments. The end-gas temperatures are plotted against the piston position in Figure 6.4 for the 16 intake air temperatures, with the red curve corresponds to the RON96 test.

These pressure and end-gas temperatures from WAVE assume no chemical heat release. The end-gas temperature and pressure profiles were then used to analyze the autoignition for three different fuels using the chemical kinetic models detailed in Section 2.3. The three different fuels all have RON96 but with varying sensitivities—PRF96, TRF96 ( $S=11$ ), and an ethanol/n-heptane blend ( $S=17$ ). The CAD corresponding to autoignition ( $CAD_{\text{autoignite}}$ ) can be determined by finding the CAD where 20 percent of the chemical energy has been released.

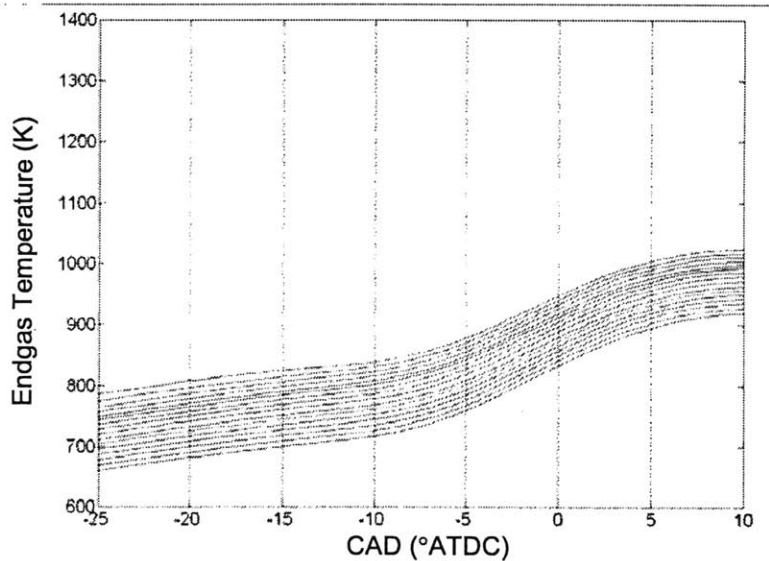
Figure 6.5 plots the temperature histories for the PRF96 at the 16 different intake air temperatures. PRF96 has a two-stage ignition process which becomes more evident at lower temperatures. The similar plots for TRF96 and the ethanol blend are shown in Figures 6.6 and Figures 6.7 respectively. All three fuels are expected to have the same  $CAD_{\text{autoignite}}$  for the RON96 test; otherwise, they would have different RON values. The temperature profiles for the RON96 test (marked as red in the plots), all appear to have autoignition occur around 3° ATDC, which is close to the value given in literature [39].

At lower temperatures, autoignition occurs later for the more sensitive fuels. For an intake air temperature of 5°C,  $CAD_{\text{autoignite}}$  goes from 7° to 8° to 9° as the sensitivity increases from 0 to 11 to 17. This trend reverses at higher temperatures; for an intake air temperature of 155°C,  $CAD_{\text{autoignite}}$  goes from 2.5° to 1.5° to 0° as sensitivity increases.

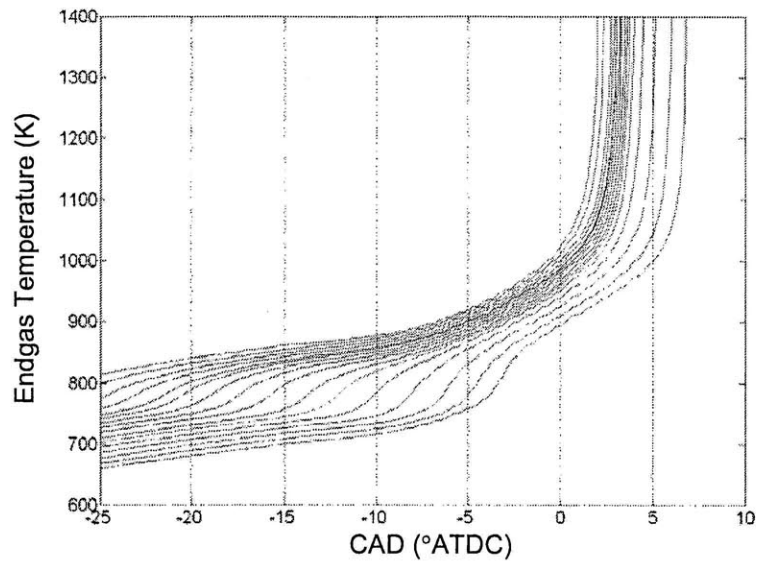


The general trend shown in the plots is that as the intake air temperatures increase,  $CAD_{autoignite}$  advances. However, for PRF96, as the intake air temperature increases from 55°C to 135°C,  $CAD_{autoignite}$  only changes from 2° to 3° ATDC. The other two fuels also show a decreased dependency of  $CAD_{autoignite}$  on the intake air temperature in this region. At the lower end of this temperature region, all three fuels have autoignition occurring at 3°. However, at the upper limit of this temperature spectrum,  $CAD_{autoignite}$  goes from 2° for PRF96, 1.2° for TRF96, to 0.5° for the ethanol blend.

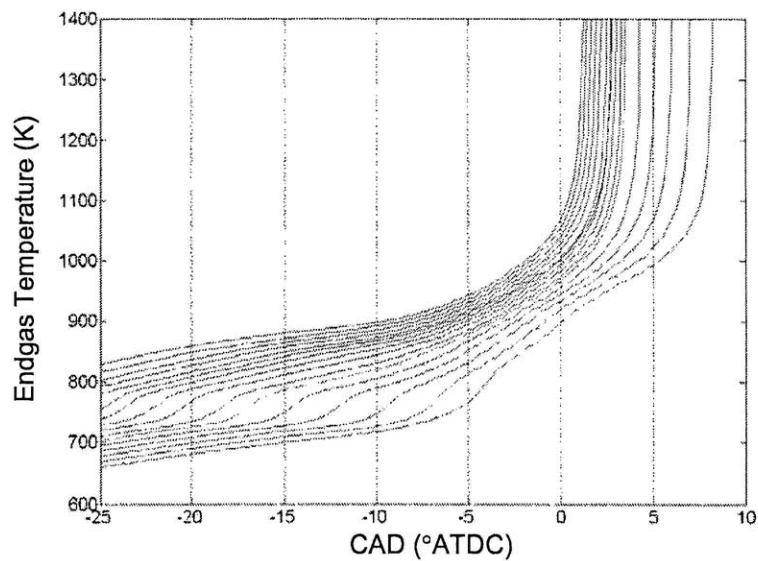
This set of plots show that the more sensitive fuels have  $CAD_{autoignite}$  values that are more sensitive to the intake air temperature. In particular, this trend is more apparent over the intermediate temperature ranges, where the  $CAD_{autoignite}$  has a decreased dependence on the intake air temperature.



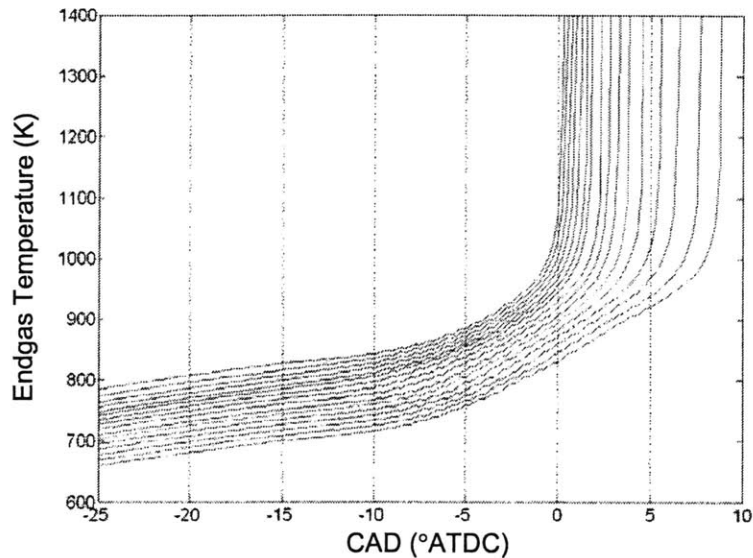
**Figure 6.4: End-gas temperature plotted against CAD for different engine intake air temperatures with no chemical heat release. The plots were generated from a WAVE model for a CFR Engine operating at WOT, stoichiometric, at 600 rpm, and a compression ratio corresponding the RON96 test. The intake air temperatures were increased from 5°C to 155°C in increments of 10. The red line corresponds to the RON96 test.**



**Figure 6.5: End-gas temperature plotted against CAD for different engine intake air temperatures with chemical heat release for PRF96 (96% iso-octane, 4% n-heptane). The plots were generated from chemical kinetic models from the temperature traces in Figure 6.4. The red line corresponds to the RON96 test.**



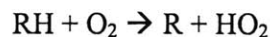
**Figure 6.6: End-gas temperature plotted against CAD for different engine intake air temperatures with chemical heat release for TRF96 (78% toluene, 22% n-heptane). The plots were generated from chemical kinetic models from the temperature traces in Figure 6.4. The red line corresponds to the RON96 test.**



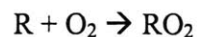
**Figure 6.7: End-gas temperature plotted against CAD for different engine intake air temperatures with chemical heat release for a RON96 ethanol blend (63.5% ethanol, 36.5% n-heptane). The plots were generated from chemical kinetic models from the temperature traces in Figure 6.4. The red line corresponds to the RON96 test.**

### 6.2.2 DIFFERENT COMBUSTION REGIMES

Over the range of end-gas temperatures in an engine, the combustion process can be broken up into three distinct regions. In all three regions, the fuel oxidation process begins by the removal of a hydrogen from the hydrocarbon (RH)<sup>\*</sup> resulting in the formation of hydroperoxyl radical (HO<sub>2</sub>):



However, the next step in the process varies depending on the temperature. At temperatures below 775 K, an oxygen (O<sub>2</sub>) molecule fills the spot vacated by the hydrogen molecule, forming a hydroperoxy alkyl radical (RO<sub>2</sub>).

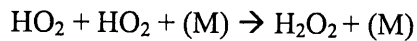
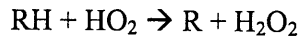



---

<sup>\*</sup> The letter R is used to denote the rest of the hydrocarbon chain. For example, ethanol (C<sub>2</sub>H<sub>5</sub>OH) can be written as ROH where R denotes the hydrocarbon chain C<sub>2</sub>H<sub>5</sub>.

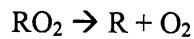
This radical then undergoes a chain of reactions that results in the production of hydroxide and partially oxygenated hydrocarbons. This process continues until the temperature arises above a certain threshold, at which point high temperature combustion begins.

At temperatures above 900 K, the hydroperoxyl radicals form hydrogen peroxide ( $\text{H}_2\text{O}_2$ ).



The production of hydrogen peroxide continues until the concentration reaches a critical amount, causing a “thermal explosion” associated with the disassociation of the hydrogen peroxide into hydroxide (OH). [19]

In the transition region, the hydroperoxy alkyl radical disassociates:

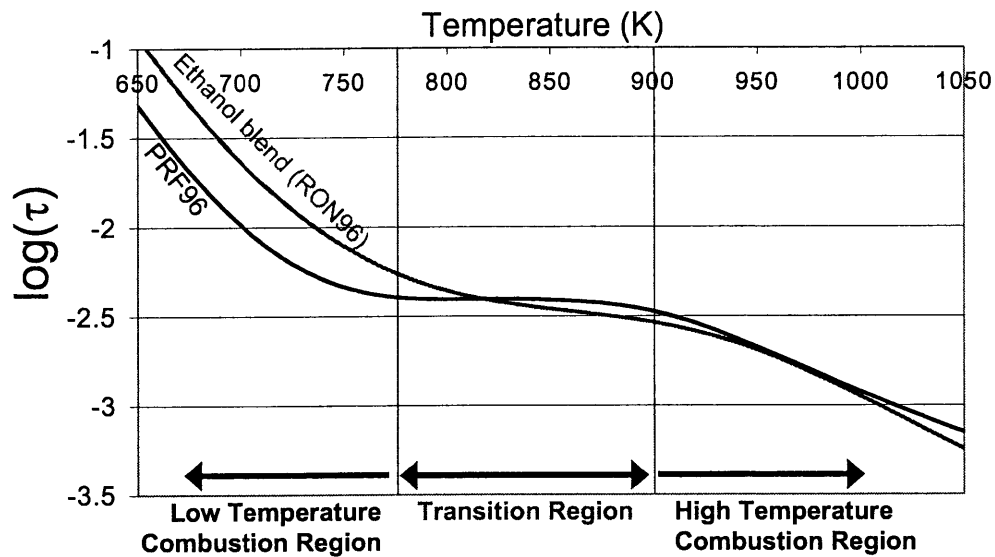


This disassociation results in the closing of the low temperature pathway. The temperatures are high enough to produce hydrogen peroxide; however, the temperatures are low enough that the hydrogen peroxide cannot disassociate.

The three regions are important because they span the end-gas temperature range of different engine operating conditions. The maximum end-gas temperatures for modern engines tend to be 850 and 950 K for naturally aspirated engines and 820 and 920 K for turbocharged engines. Therefore, much of the autoignition chemistry in modern engines occurs during the transition combustion regime. The maximum end-gas temperature for the RON96 test is approximately 950 K, and much of its autoignition chemistry also occurs during the transition region. However, the maximum end-gas temperature for the MON96 test is significantly higher (1030 K) and higher temperatures cause much more of the chemistry to occur in the high temperature regime.

The autoignition delay time ( $\tau$ ) was found for the different fuels as a function of different initial temperatures and pressures through the use of the constant pressure batch reactor models detailed in Chapter 2. Figure 6.8 shows a plot of  $\tau$  versus temperature for the non-sensitive PRF96 and the sensitive ethanol blend at a pressure of 50 bar. At other pressures, the plots were similar though translated vertically.

Figure 6.8 shows that both fuels have a low-temperature, transition, and high-temperature regions. The slope of the  $\tau$ -T curve is similar for both fuels in the low temperature and high temperature regions. However, in the transition region, the most relevant region for autoignition in modern engines, the slope for the low-sensitivity fuel is less than that of the high-sensitivity fuel.



**Figure 6.8:** The autoignition delay time as a function of temperature for a pressure of 50 bar, for a non-sensitive RON96 fuel (PRF96,  $S = 0$ ) and for a sensitive RON96 fuel (ethanol/n-heptane blend,  $S = 17$ ). The plots for both fuels can be divided into three different regions—low temperature combustion, high temperature combustion, and transition regions.

### 6.2.3 TRANSITION REGION

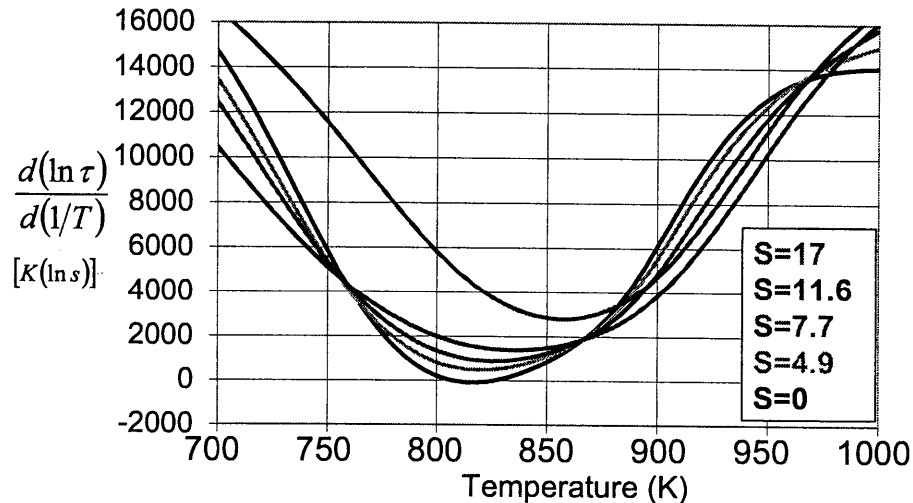
For modern engines and fuels, much of the autoignition process occurs during the transition region. In this region, the relationship between  $\tau$  and temperature ( $T$ ) is a property of the fuel. Due to the form of  $\tau$ , the derivative to  $\tau$  in regards to  $T$  would carry strong temperature terms. These terms can be nullified by taking the derivative of  $\ln(\tau)$  in regards to  $1/T$ :

$$\tau = c_1 p^{-c_2} \exp(c_3/T) \rightarrow \ln(\tau) = c_1 - c_2 \ln(p) + \frac{c_3}{T}$$

$$\frac{\partial}{\partial(1/T)}(\ln(\tau)) = \text{Dependence of } \tau \text{ on } T \quad (\text{Eq. 6.1})$$

As this variable gets smaller,  $\tau$  becomes less dependent on temperature. This term is the appropriate metric for comparing  $\tau$ 's dependence on temperature for different fuels.

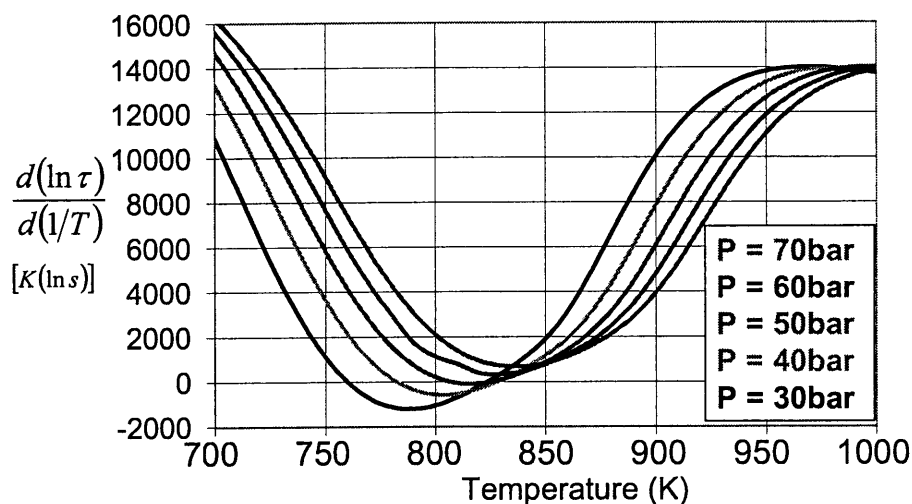
A plot of this derivative at a pressure of 50 bar is given in Figure 6.9. As the temperature increases, the value of the derivative decreases until it reaches a minimum value in the transition region. The derivative then increases as it goes through high temperature combustion. As the sensitivity of the fuel increases, the minimum value of the derivative also increases. Hence,  $\tau$  for more sensitive fuels has a higher dependence on temperatures in the transition region than less sensitive fuels. This trend provides useful insight into the fundamentals of sensitivity.



**Figure 6.9:**  $d(\ln \tau)/d(1/T)$  plotted against temperature to determine the autoignition delay time's dependence on temperature in a constant pressure batch reactor (50 bar). The plots show five different RON96 fuels with varying sensitivities. As sensitivity increases, the curves shift upwards and to the right.

Equation 6.1 gives that  $d(\ln \tau)/d(1/T)$  should be independent of pressure. Figure 6.10 shows a plot of  $d(\ln \tau)/d(1/T)$  at different pressures for PRF96. The other four RON96 fuels showed

similar plots, where the curve shifts upwards and to the right as the pressure increases. The plot shows that as pressure increases, a fuel's autoignition delay time has a stronger temperature dependence in the transition region. Additionally, the transition region spans a smaller range of temperatures.

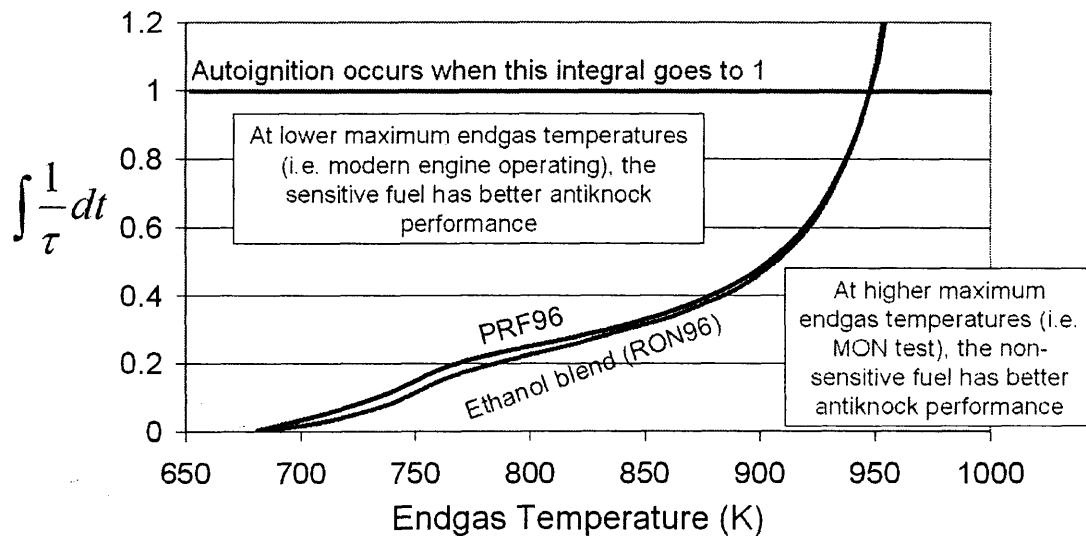


**Figure 6.10:**  $d(\ln \tau)/d(1/T)$  plotted against temperature to determine the autoignition delay time's dependence on temperature in a constant pressure batch reactor for PRF96 over a range of pressures. As the pressure increases, the curves shift upwards and to the right. The similar plots for the other RON96 fuels showed similar results.

The maximum end-gas temperature in the RON96 test is on the border between the transition region and the high-temperature combustion region. However, most of the chemistry occurs in the transition region. Since more sensitive fuels have a higher dependence of  $\tau$  on  $T$  in the transition region, they have slower autoignition chemistry at lower temperatures and faster autoignition chemistry at higher temperatures. On the other hand, the autoignition speed for non-sensitive fuels is roughly independent of temperature.

The autoignition integrals for the RON96 test were determined for a sensitive and non-sensitive fuel and are displayed in Figure 6.11. Since both fuels have a RON of 96, the integrals go to 1 at the same point. Figure 6.11 shows that the autoignition integral increases steadily for the non-sensitive fuel. However, the sensitive fuel initially has slow autoignition chemistry, which gets

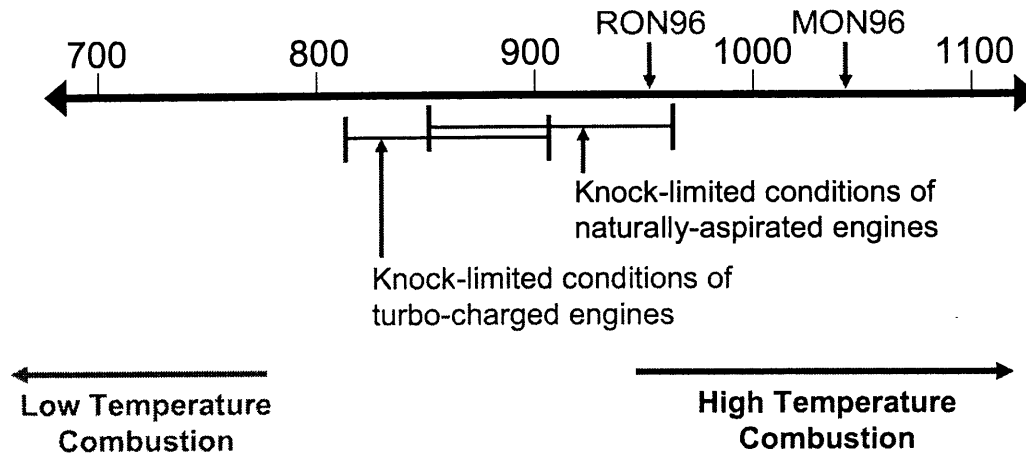
faster at higher temperatures, corresponding to a higher temperature dependence. If the autoignition chemistry for the RON96 test is compared to a race between a sensitive fuel and a non-sensitive fuel, both would finish the race at the same time (otherwise, they would have different RON values). The less sensitive fuel would run the race at a relatively steady pace. On the other hand, the more sensitive fuel would run the first portion of the race slowly, but pick up the pace so that the two fuels can finish at the same time. If the race was shortened, the sensitive fuel would not catch up to the non-sensitive fuel, and hence the sensitive fuel would have better antiknock performance. Meanwhile, if the race is extended, the sensitive fuel, which is already going at a faster pace, would beat the non-sensitive fuel, causing the non-sensitive fuel to have better antiknock performance.



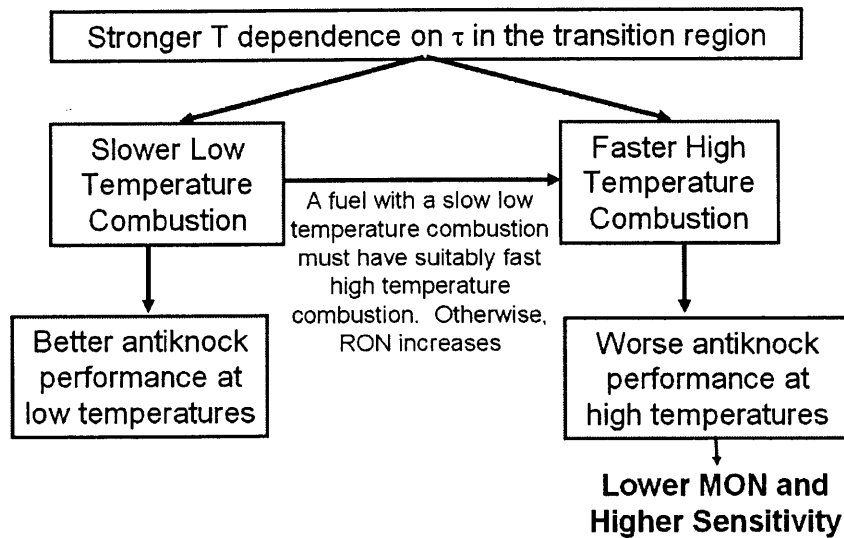
**Figure 6.11: The autoignition integral as a function of endgas temperature for the RON96 test, for a non-sensitive RON96 fuel (PRF96,  $S = 0$ ) and for a sensitive RON96 fuel (ethanol/n-heptane blend,  $S = 17$ ).**

Figure 6.12 shows the spectrum of maximum end-gas temperatures for different engine conditions. The plot shows that the maximum end-gas temperature for the RON96 is at the upper range of what modern naturally aspirated engines operate at. However, as engines get boosted, the range of temperatures shifts downwards. Meanwhile, the MON96 test is almost 100°C above the RON test and is well into the high temperature combustion regime.





**Figure 6.12: The end-gas temperature spectrum for engine operations. The maximum end-gas temperature for the RON96 and MON96 tests are at 950 K at 1030 K. Modern naturally aspirated engines have maximum end-gas temperatures between 850 and 960 K. That range shifts downwards as engines become turbo-charged. The maximum end-gas temperatures for modern naturally aspirated and boosted engines are in the transition range between high temperature and low temperature combustion.**



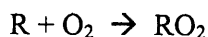
**Figure 6.13: This flowchart shows how a stronger temperature dependence on the autoignition delay time in the transition region results in a fuel having a lower MON value, hence having a higher sensitivity.**

This spectrum of end-gas temperatures is then used in Figure 6.13 to show the implications of the temperature dependence on  $\tau$  in the transition region. Since the high sensitivity fuel has slower autoignition at lower temperatures, these fuels should have better antiknock performance over most of the knock-limited conditions that engines tend to operate at. However, since the MON test is well into the high temperature combustion region, it has a bias towards fuels with slower high-temperature autoignition; hence why more sensitive fuels have lower MONs.

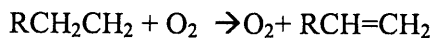
### 6.3 CHEMICAL FUNDAMENTALS

#### 6.3.1 HYDROGEN PEROXIDE, HYDROPEROXY ALKYL RADICALS, ETHYLENE, AND ALDEHYDES

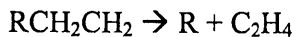
The analysis in the previous section found that higher sensitivity fuels have autoignition delay times with a stronger temperature dependence in the range of temperatures between 775 K and 900 K. The underlying chemistry can be explained through looking at the chemical intermediates formed during the autoignition process. The autoignition pathways of fuels with alkyl groups are different in the three temperatures ranges. The first steps in all of the pathways are similar; the weakest C-H bond is broken forming a radical. In low temperatures, an O<sub>2</sub> atom fills the valence previously occupied by the hydrogen, and the  $\pi$  bond in the O<sub>2</sub> atom then breaks:



However, at medium temperatures, the fuel produces HO<sub>2</sub> and an alkene:

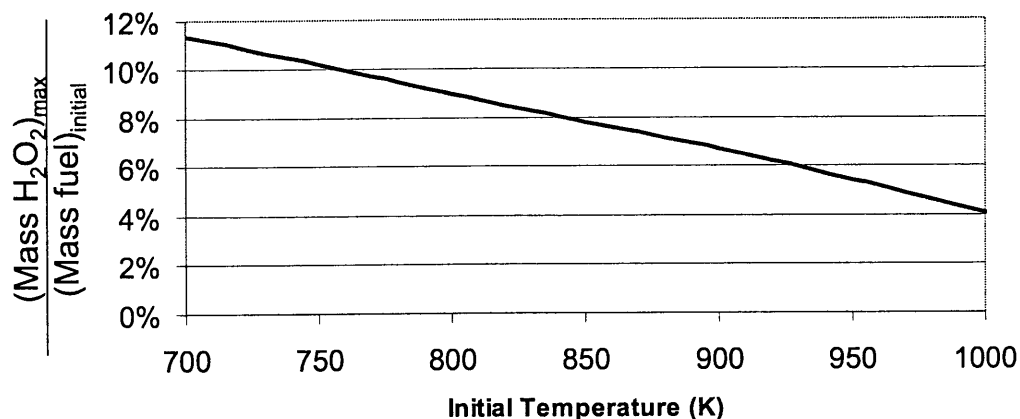


At high temperatures, the reduction mechanism produces a radical and an ethylene molecule.



The important underlying intermediate in hydrocarbon combustion is hydrogen peroxide (H<sub>2</sub>O<sub>2</sub>). A critical amount of hydrogen peroxide is required before it disassociates into hydroxyl radicals, initiating a thermal explosion [19]. This dissociation of hydrogen peroxide is fundamentally responsible for much of the energy release for an autoignition reaction.

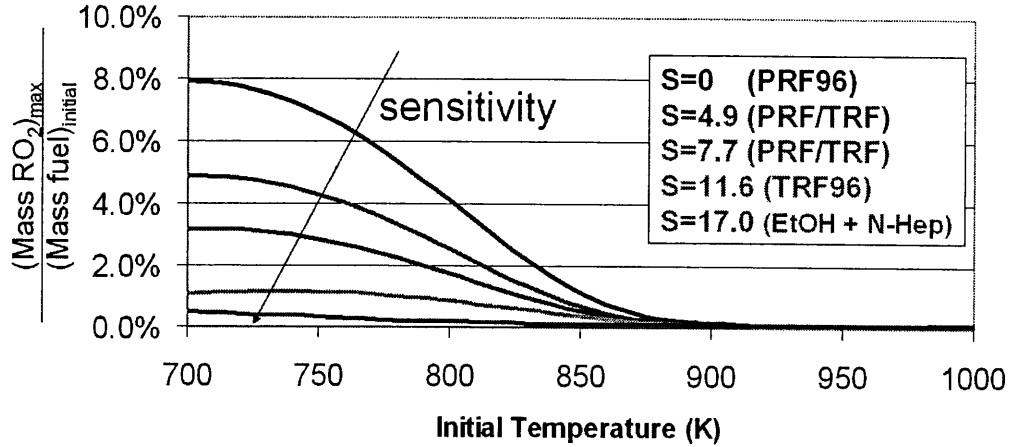
The chemical kinetic models found that as the initial temperature increases for the reaction, the amount of hydrogen peroxide required for the thermal explosion decreases. This trend is shown for PRF96 in Figure 6.14. The other fuels showed the same trend.



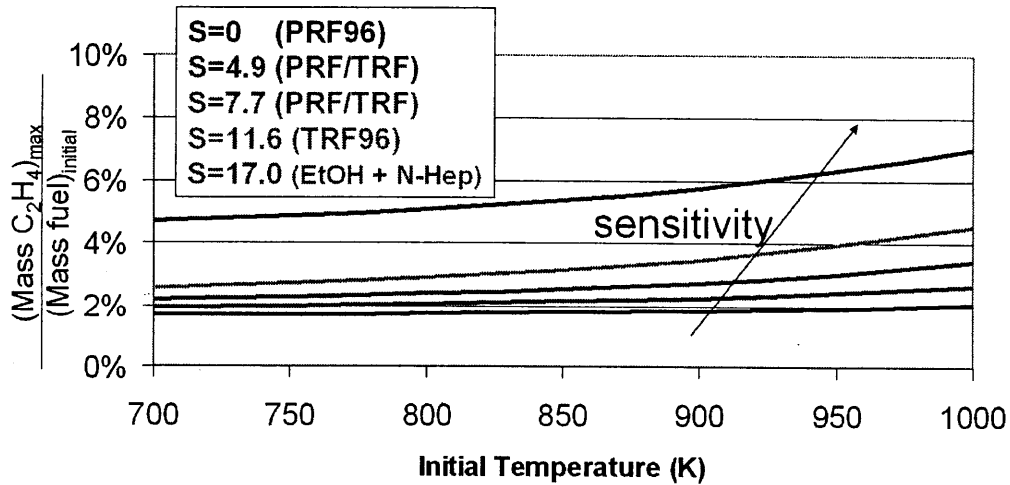
**Figure 6.14: The amount of hydrogen peroxide (H<sub>2</sub>O<sub>2</sub>) required for a thermal explosion at different initial temperatures in a constant pressure batch reactor, with the pressure set at 50 bar. At lower temperatures, a higher concentration of hydrogen peroxide is required for the thermal explosion to occur.**

Hydroperoxy alkyl radicals (RO<sub>2</sub>) are an intermediate associated with low temperature combustion. At higher temperatures, these radicals dissociate, so only trace amounts are found at temperatures above 900 K. Figure 6.15 shows the maximum amount of hydroperoxy alkyl radicals produced as an intermediate in the autoignition reaction. The plot shows two important trends. First, as the temperature increases the amount of the radical decreases. Second, as the sensitivity of the fuel increases, the amount of hydroperoxy alkyl radicals produced as an intermediate decreases.

Ethylene (C<sub>2</sub>H<sub>4</sub>) is an intermediate associated with high temperature combustion. Figure 6.16 shows the maximum amount of ethylene produced as an intermediate in the autoignition reaction, and the plot follows the opposite trends to that of the hydroperoxy alkyl radicals. The amount of ethylene produced increases with temperature. Also, more sensitive fuels produce more ethylene than less sensitive fuels; this trend becomes more apparent at higher temperatures.



**Figure 6.15:** The maximum amount of hydroperoxy alkyl radicals ( $\text{RO}_2$ ) produced as an intermediate at different initial temperatures in a constant pressure batch reactor, with the pressure set at 50 bar. The trend shows that more sensitive fuels produce less hydroperoxy alkyl radicals.

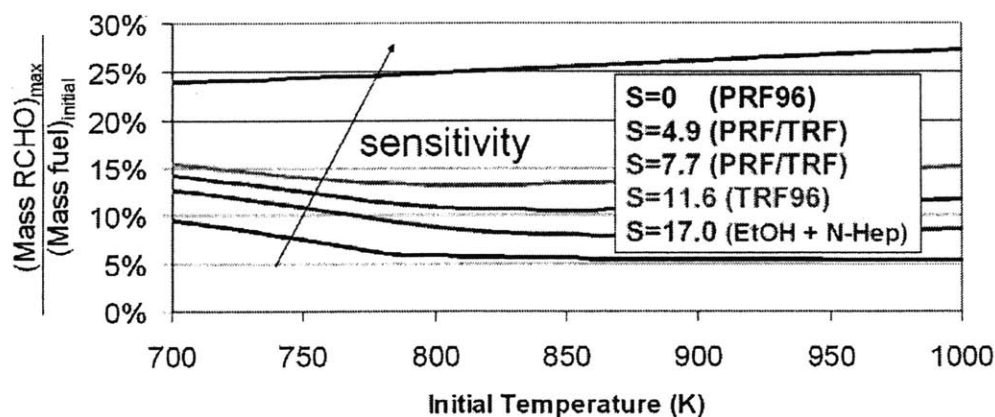


**Figure 6.16:** The maximum amount of ethylene molecules ( $\text{C}_2\text{H}_4$ ) produced as an intermediate at different initial temperatures in a constant pressure batch reactor, with the pressure set at 50 bar. The trend shows that more sensitive fuels produce more ethylene.

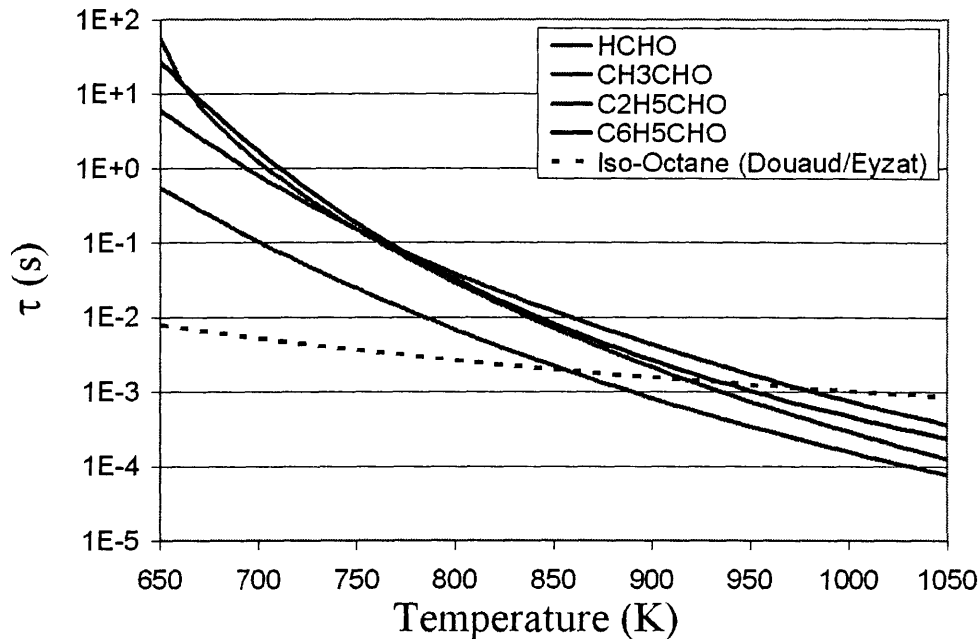
The production of hydroperoxy alkyl radicals in less sensitive fuels corresponds with them having faster low temperature autoignition. Meanwhile, the production of ethylene in more sensitive fuels shows that they have faster high-temperature combustion. These trends correspond to the findings in the previous section.

Aldehydes (RCHO) are another important intermediate in autoignition chemistry. Figure 6.17 shows that between 5% and 30% of the fuel mass becomes an aldehyde during the autoignition process. As the sensitivity of the fuel increases, the amount of aldehydes produced also increases. The plot also shows that the amount of aldehydes produced as an intermediate has a negligible temperature dependence. Therefore, even at low temperatures, a significant amount of the fuel forms into aldehydes.

Chemical models were run for four different aldehydes to determine how their autoignition delay times depend on temperature. The four aldehydes chosen are formaldehyde (HCHO), acetaldehyde (CH<sub>3</sub>CHO), propionaldehyde (C<sub>2</sub>H<sub>5</sub>CHO), and benzaldehyde (C<sub>6</sub>H<sub>5</sub>CHO). Acetaldehyde and benzaldehyde are the aldehyde intermediates of ethanol and toluene autoignition. The results from the chemical models are plotted in Figure 6.18, along with the plot for iso-octane, as predicted by the Douaud-Eyzat equation, as a reference. The plot shows that all the aldehydes have long autoignition delay times at lower temperatures and fast autoignition delay times at high temperatures. The autoignition delay times for the four aldehydes have stronger temperature dependences than what the Douaud-Eyzat equation predicts. The Douaud-Eyzat equation gives that for a fuel,  $d(\ln \tau)/d(1/T) = 3800$ . However, for the aldehydes, the value of this derivative is between 15000 and 17000.



**Figure 6.17: The maximum amount aldehydes (RCHO) produced as an intermediate at different initial temperatures in a constant pressure batch reactor, with the pressure set at 50 bar. The trend shows that more sensitive fuels produce more aldehydes.**



**Figure 6.18: The autoignition delay time as a function of temperature at a pressure of 50 bar, for formaldehyde (HCHO), acetaldehyde (CH<sub>3</sub>CHO), propionaldehyde (C<sub>2</sub>H<sub>5</sub>CHO), and benzaldehyde (C<sub>6</sub>H<sub>5</sub>CHO). Also included in the plot is iso-octane from the Douaud/Eyzat equation, as a reference.**

Hydrogen peroxide, hydroperoxy alkyl radicals, ethylene, and aldehydes are the crucial intermediates in explaining the chemical fundamentals of fuel sensitivity. The chemical models showed that as the temperature increases:

- 1) The critical amount of H<sub>2</sub>O<sub>2</sub> required for a thermal explosion decreases.
- 2) The production of RO<sub>2</sub> decreases and so there is less low temperature combustion.
- 3) The production of C<sub>2</sub>H<sub>4</sub> increases and so there is more high temperature combustion.
- 4) The production of RCHO stays relatively constant, though their dissociation rate gets significantly faster.

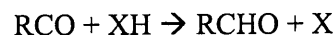
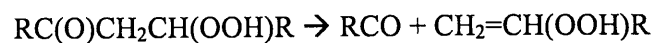
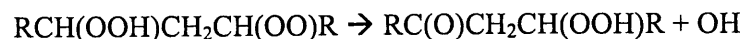
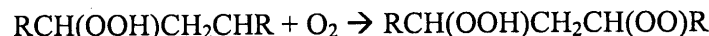
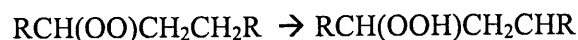
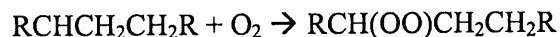
The models also show that as sensitivity increases:

- 1) The production of RO<sub>2</sub> as an intermediate decreases.
- 2) The production of C<sub>2</sub>H<sub>4</sub> as an intermediate increases.
- 3) The production of RCHO as an intermediate increases.

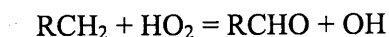
Since RCHO competes with the production of H<sub>2</sub>O<sub>2</sub>, at low temperatures when the critical amount of H<sub>2</sub>O<sub>2</sub> is larger, more sensitive fuels (i.e. those with higher amounts of RCHO) are more resistant to autoignite. However, at higher temperatures, such as those in the MON test, the critical amount of H<sub>2</sub>O<sub>2</sub> is lower, and aldehydes will undergo degenerative branching, forming more H<sub>2</sub>O<sub>2</sub>, resulting in faster autoignition.

### 6.3.2 FORMATION OF RCHO

Fuel molecules undergo the following process to form aldehydes at low temperatures:



If the RCH<sub>2</sub> radical formed from the extraction of hydrogen is stable at low temperatures, aldehydes can be formed at medium temperatures:



The chemical kinetic models found that the RCH<sub>2</sub> radicals for toluene and ethanol are stable at low temperatures, explaining why these hydrocarbons form large amounts of aldehydes.

## 6.4 CONCLUSIONS

The chemical kinetic models performed in this chapter to investigate the chemical fundamentals of fuel sensitivity showed that:

- For modern engines, much of the autoignition chemistry occurs in the transition region between high and low temperature combustion.

- Fuels with a higher sensitivity have a higher temperature dependence on autoignition in the transition region. A stronger temperature dependence on  $\tau$  in the transition region results in slower low temperature combustion and faster high temperature combustion. Fundamentally, sensitivity is how “sensitive” a fuel’s autoignition chemistry is to temperature in the transition region.
- As sensitivity increases, the fuel produces less hydroperoxy alkyl radicals and more aldehydes as intermediates. The hydroperoxy alkyl radicals allow for fast low temperature combustion, while aldehydes are relatively stable at low temperatures. However, aldehydes react very rapidly at high temperatures.
- More sensitive fuels are more prone to form aldehydes than non-sensitive fuels. The formation of aldehydes requires a stable  $RCH_2$  radical at low temperatures, as is the case for ethanol and toluene.



## CHAPTER 7: HISTORIC SHIFTS IN K VALUES

The analysis in Chapter 5 found that K relates the maximum endgas temperatures in an engine to that of the RON and MON tests. In a more general sense, K is an indicator as to how well the RON and MON test bracket the autoignition behavior of a fuel. If K is 1, the fuel behaves similar to how it would behave in the MON test. If K is 0, the fuel behaves as it would in the RON test. If K is between 0 and 1, the two tests bracket the autoignition behavior of the fuel. However, if K is above 1 or less than 0, the RON and MON test no longer accurately capture the antiknock properties of the fuel.

Values from literature, Coordinated Research Council reports, and WAVE models were analyzed to study the shift in K values from 1 in 1932 to its current negative value.

### 7.1 EARLY VALUES OF K

When the RON test was first developed in 1928, critics complained that the test was not relevant to on-the-road conditions. The culprit was found to be that the CFR Engine has a much more advanced cooling system than those in 1928 commercial SI engines, which had cylinder temperatures almost 100°C hotter than the CFR Engine. To compensate for this discrepancy and to match on-the-road engine conditions, a new test was developed with a heated intake system. This test was the MON, which was introduced in 1932. Hence, in 1932, the average value of K for on the road engines was 1, corresponding to the OI being the MON.

Only three years later, engine technology had advanced enough that the oil industry re-evaluated the MON test. The L-3 knock test method was developed in 1935 to reflect the changes in on-the-road OI. The tests were set at a condition such that K was equal to 0.65. However, this test technique was never adopted for fuel rating purposes. [9]

In 1960, the Ethyl Corporation performed a study to evaluate the RON and MON tests. They found that K had dropped to an average value of 0.5 by 1946 and to 0.33 by 1961 [9]. A

committee was set up to look at how to change the RON and MON tests. As a consequence, the Ethyl Corporation pushed for modifications set of tests, which went unheeded [43].

## **7.2 1951-1991 COORDINATED RESEARCH COUNCIL STUDY**

Due to the engine-fuel relationship of knock, fuel companies need to know the octane requirements of the fleet to properly refine their fuels. Therefore, the Coordinated Research Council (CRC), a consortium of engine and fuel companies, performed annual statistical surveys to determine the octane requirements for fleet vehicles. These studies looked at the “distributions of vehicles octane requirements as a function of satisfaction levels and fuel sensitivity in a sample representative of modern vehicles [26].” The CRC first began performing these annual studies following World War II. These studies were continued until it was deemed that the inclusion of knock sensors on cars limited their necessity. The scope of the surveys was diminished starting in 1992. After 1996, the surveys were no longer conducted.

These studies by the CRC looked at different fuels so that their data could address how new fuel technology affects the octane appetite of the fleet. For each annual study, a set of test fuels of varying ON was produced. These fuels were meant to be representative of the fuels on the market. Multiple fuel sets were sometimes necessary, such as when both leaded and unleaded fuels were available. However, at a minimum, every study included both primary reference fuels and full-boiling range unleaded fuels (FBRU), which were meant to represent commercial fuels. The sensitivities of the fuels were typically between 7 and 10. [26]

The CRC performs their tests at wide-open-throttle acceleration. The vehicle is mounted on a chassis dynamometer, and the vehicle accelerates until the engine reaches its top speed or until knock occurs. If the engine does not knock during the acceleration, the fuel is replaced with a fuel with a lower octane number. The process was repeated until the engine knock. The tester then records the minimum fuel octane number that avoided knock, as well as the conditions (e.g. intake air temperature, engine speed, intake air pressure) that precipitated knock. [26]

### 7.2.1 DETERMINING K FROM SURVEY DATA

Since the FBRU test fuels were blended to be representative of fuels in the market, they have non-zero sensitivities. The value of S as a function of RON was given in each survey. Identical tests were performed with both FBRUs and PRFs, effectively giving the OI of the FBRU for a given engine at a given condition.

$$K = \frac{RON_{FBRU} - ON_{PRF}}{S_{FBRU}} \quad (\text{Eq. 7.1})$$

At some engine conditions, the speed associated with knock onset was significantly different for the FBRU and the PRF. Since K is speed dependent, these data points were removed from this analysis.

This analysis chose to use the surveys from 1951, 1961, 1971, 1981, and 1991 [26]. These surveys were chosen because they were in 10 year increments, finishing in 1991, the last complete CRC Octane Requirement Survey.

### 7.2.2 CHANGE IN THE MAXIMUM REQUIRED OCTANE NUMBER

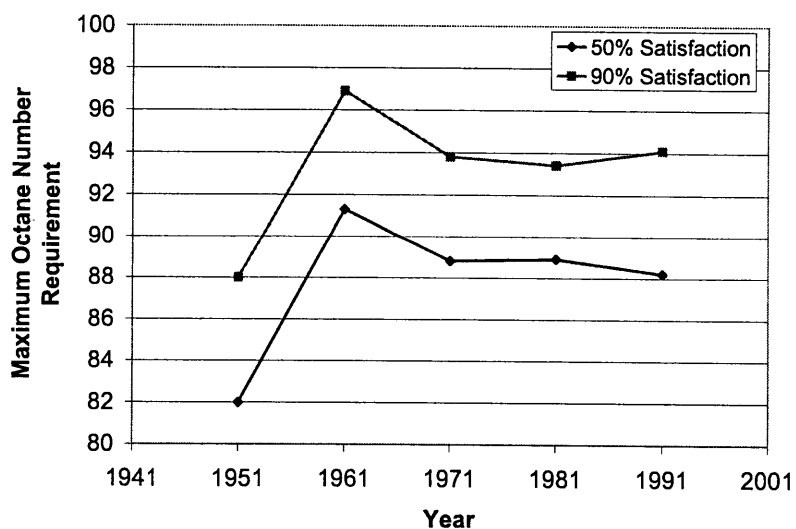
Figure 7.1 gives the (R+M)/2 of the fuel required to avoid knock in 50% and 90% of the fleet. The trends show that the value increases between 1951 and 1961. This increase is due to the increased availability of high octane fuels, due to new refining technology developed during World War II [15]. Between 1961 and 1971, the maximum ON requirement decreases. This decrease is due to the phasing out of lead as an anti-knock agent. Between 1971 and 1991, the value stays fairly constant.

### 7.2.3 AVERAGE K VALUE

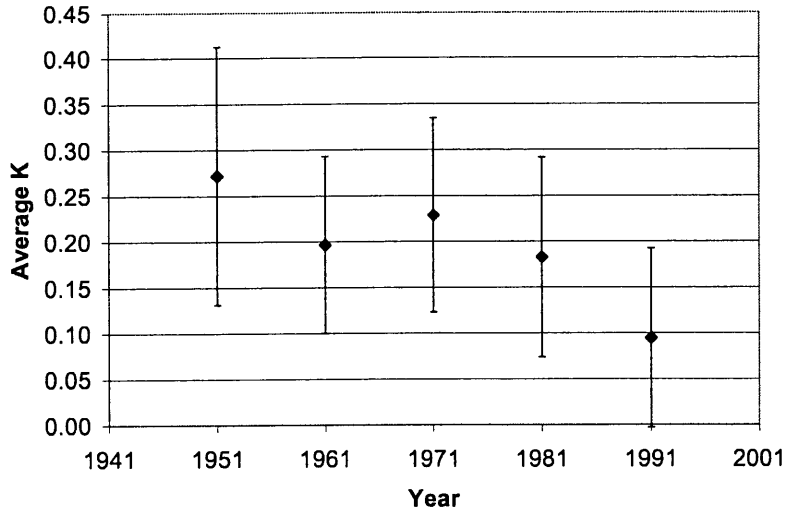
The average value of K for 1951, 1961, 1971, 1981, and 1991 are shown in Figure 7.2. The plot shows that the average value of K decreased between 1951 and 1961. The value then stayed fairly constant between 1961 and 1981. The average value of K then significantly decreases

again between 1981 and 1991. If the trend between 1981 and 1991 were to be extrapolated, the value of K would be around 0 by 2001. This value agrees with the findings of Kalghatgi [12].

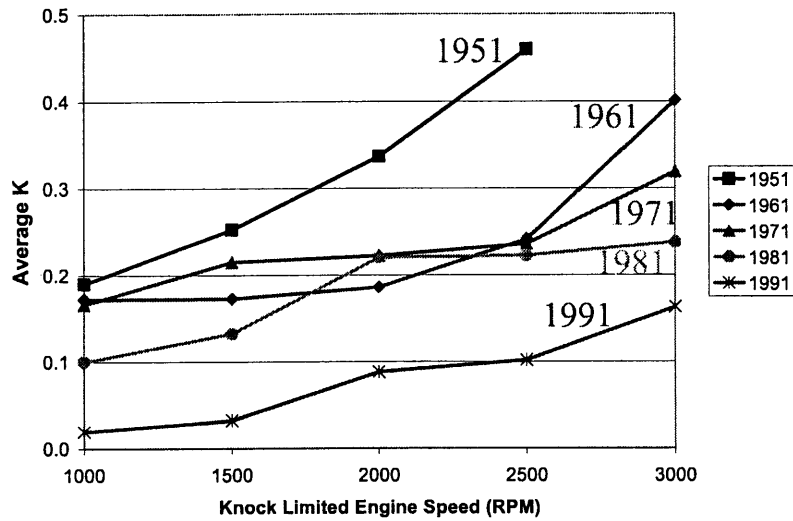
It should be noted that the large error bars are due to the large range of vehicles that were tested each year. For example, in 1951, 450 different vehicles were tested. The vehicles included “new design” vehicles (i.e. manufactured in 1951) and “control” vehicles (i.e. manufactured in 1946-1950). Additionally, vehicles included both cars and light trucks, which have very different operating regimes [26]. The large error bars also occur because different engines have different knock limited speeds. Figure 7.3 shows the average value of K for the five years as a function of speed. This plot shows that K increases with engine speed, following the trend found in Chapter 5. Additionally, the plot shows that between 1951 and 1961, K decreased substantially, especially at higher speeds. Between 1961 and 1981, the change in K only occurs at low and high speeds. The average value of K does not change much in the mid-speed range (2000-2500 rpm). Between 1981 and 1991, the value of K dropped by approximately 0.1 at all speeds.



**Figure 7.1: The Maximum ON required to satisfy 50% (blue) and 90% (magenta) of the fleet in 1951 to 1991.**



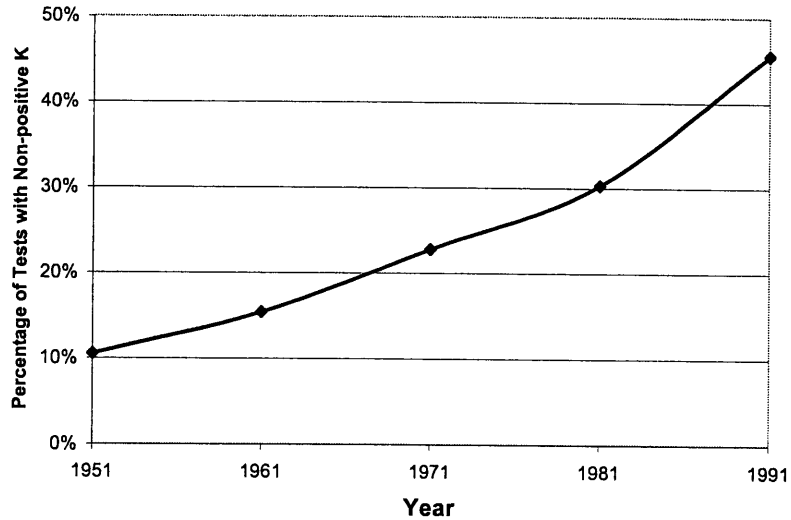
**Figure 7.2: The average value of K in 1951, 1961, 1971, 1981, and 1991.**



**Figure 7.3: The average value of K at each engine speed for 1951 to 1991.**

Figure 7.3 shows that K only reaches values of 0.5 at high speeds in 1951. In other years, K is well below this value, even at high speeds. Therefore the assumption that  $K = 0.5$ , the value of the OI that is placed on fuel pumps, was already inaccurate by 1951.

The goal of the RON and MON test were to bracket the knock limited region. That way, the behavior of a fuel in an engine could be interpolated between the MON and RON values (i.e. have a positive value of  $K$ ). However, Figure 7.4 shows that between 1951 and 1991, the number of tests outside of this range (i.e. having a non-positive value of  $K$ ) increased steadily.



**Figure 7.4: The percentage of engine tests in the CRC surveys that had negative values of  $K$ .**

#### **7.2.4 CHANGES IN ENGINE TECHNOLOGY BETWEEN 1928 AND PRESENT**

The fact that the octane number tests have not changed since 1928 is remarkable considering the vast technological advancements in engine technology. Engine computer units now allow for advanced engine controls, replacing antiquated servos and mechanical devices. Engine geometries are designed using CFD and chemical kinetic modeling to optimize burn speeds and minimize knock. All of these changes can be exemplified through the change in engine horsepower. The 1928 Ford Model T engine could produce a maximum of 22 HP, corresponding to 1600 RPM. Meanwhile, the 2008 Ford Fusion engine, which has the same displaced volume as the Model T, produces a maximum of 221 HP corresponding to 6250 RPM [14].

Figure 7.5 shows the change in the average engine displaced volume and compression ratio between 1928 and the present. The value for 1928 was taken from Taylor [7], the values for 1951 to 1991 were taken from the CRC Reports, and the value for 2008 was taken from Wards [14]. Figure 7.5 shows that the compression ratio has increased rapidly between 1928 and 1961. It then levels off between 1961 and 1981 and continued to rise from 1981 to 2008. The displaced volume increased steadily between 1951 and 1971. The value then sharply declines between 1971 and 1981, and then begins to creep back to higher values.

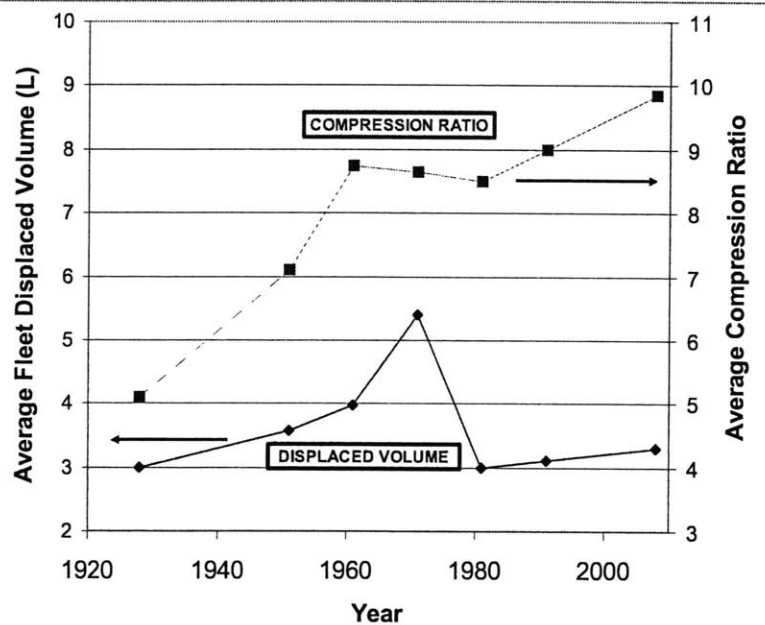
The increase in compression ratio between 1928 and 1961 can be attributed to the commercial availability of high octane fuels. The development of the octane tests allowed a standardized testing of different fuels, hence allowing for fuel optimization. Further, during World War II, the United States developed many techniques, such as catalytic cracking, to mass produce high octane fuels. These techniques slowly spread into the commercial sector, and by 1961, new cars were utilizing this high octane fuel so that the engines could operate at higher compression ratios. [15]

Between 1961 and 1971, the compression ratio stayed the same, but the average displaced volume increased dramatically. The methodology at the time to increase engine power was to simply make the engine bigger. However, this trend was non-sustainable due to the oil crisis in the mid 1970s. Between 1971 and 1981, the average displaced volume decreased by 35%. The compression ratio also decreased between 1971 and 1981 because tetraethyl lead, a key antiknock agent, was being removed from fuels on the market.

Between 1981 and 2008, advancements in engine technology facilitated an increase in compression ratio, allowing for the engine power output to increase without increasing the displaced volume.

The biggest change in early engine design between 1928 and 1951 was the “notable strides in engine cooling. [9]” These engine cooling techniques included full-length cylinder jackets which allowed for the free circulation of water around the cylinder. These techniques eliminated hot

spots which were a common source of autoignition. The better engine cooling resulted in a decrease in the final end-gas temperatures, hence decreasing  $K$  significantly.



**Figure 7.5: The average displaced volume and compression ratios in 1951-1991.**

Another major change in the engine operating conditions during these 80 years is the steady increase in the intake air pressure. Engine designers strive to increase the volumetric efficiency of the engine, hence decreasing the pressure losses in the intake manifold. Consequently, with fewer losses in the intake manifold, the intake air pressure at wide open throttle is higher. The results from Chapter 5 showed that as the intake air pressure increases,  $K$  decreases.

Figure 7.6 shows the torque versus engine speed curve for different intake air systems. The increase in torque corresponds to an increase in the intake air pressure. The figure is from 1989, so the “contemporary 2-valve” engine corresponds to those that would have been likely present in 1991 [6]. Figure 7.7 shows that in 1991, half of the car engines used a four valve system and half used a two valve system. A linear extrapolation gives that a negligible number of engines had 4 valves before 1982. The major improvement between “historic” and “contemporary” 2-valve engines is engine tuning. Between 1951 and 1981, the intake air pressure increased due to



tuning, which decreased the losses in the intake system, especially at higher speeds. The use of 4-valve cylinders further increased the intake air pressure by increasing the flow area.

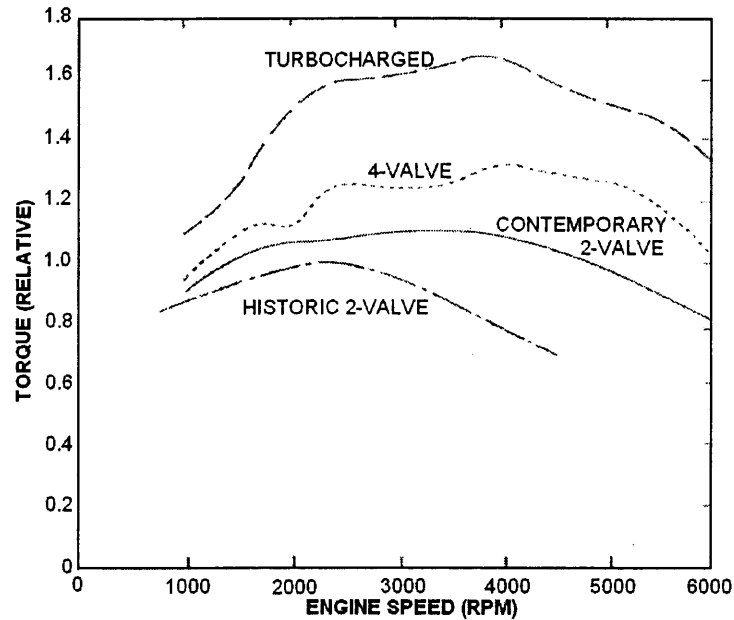


Figure 7.6: Engine breathing technology in 1991 [6].

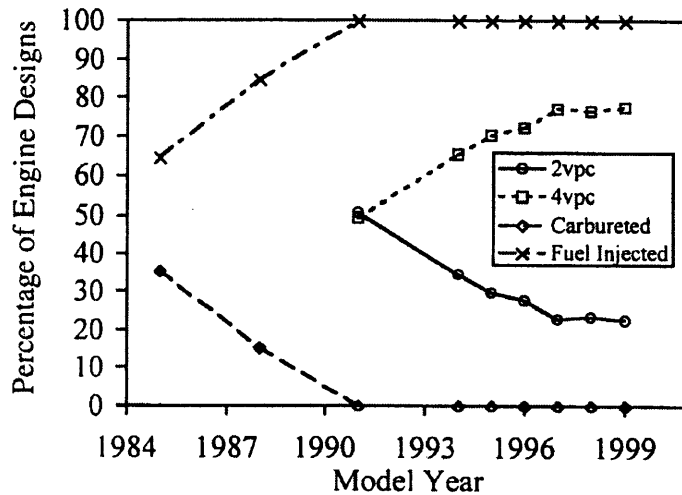


Figure 7.7: Engine valve and fuel injection technology between 1985 and 1999 [44]

The other major parameter that plays a role in  $K$  is the intake air temperature. Figure shows that by 1991, all new engines were equipped with fuel injectors instead of carburetors. Extrapolating

from the plot gives that in 1981, 40 percent of engines had fuel injectors, and a negligible number of engines had fuel injectors in 1951, 1961, and 1971. This increased use of fuel injectors come from the fuel metering requirements necessary for strict emission controls.

Fuel injectors do not require that the intake air be heated up so that the fuel would vaporize. Rather, the pressurized drops are sprayed onto the hot intake valve, which vaporizes the fuel. Therefore, the increased use of fuel injectors would result in a significant decrease in the intake air temperature, and hence a decrease in  $K$ . The strong decrease in  $K$  value between 1981 and 1991 is due to the wide spread use of fuel injection systems.

### **7.3 KNOCK LIMITS OF HISTORIC, CURRENT, AND FUTURE SI ENGINES**

The above analysis gives the average value of  $K$  as a function of year. However, since  $K$  is a property of the engine operating conditions, it has a large range of values for any engine. WAVE was used to model different SI engines and to determine how the knock-limited range of each engine. Over the knock-limited range, the relationships found in Chapter 5 were used to determine a statistical distribution of  $K$  values.

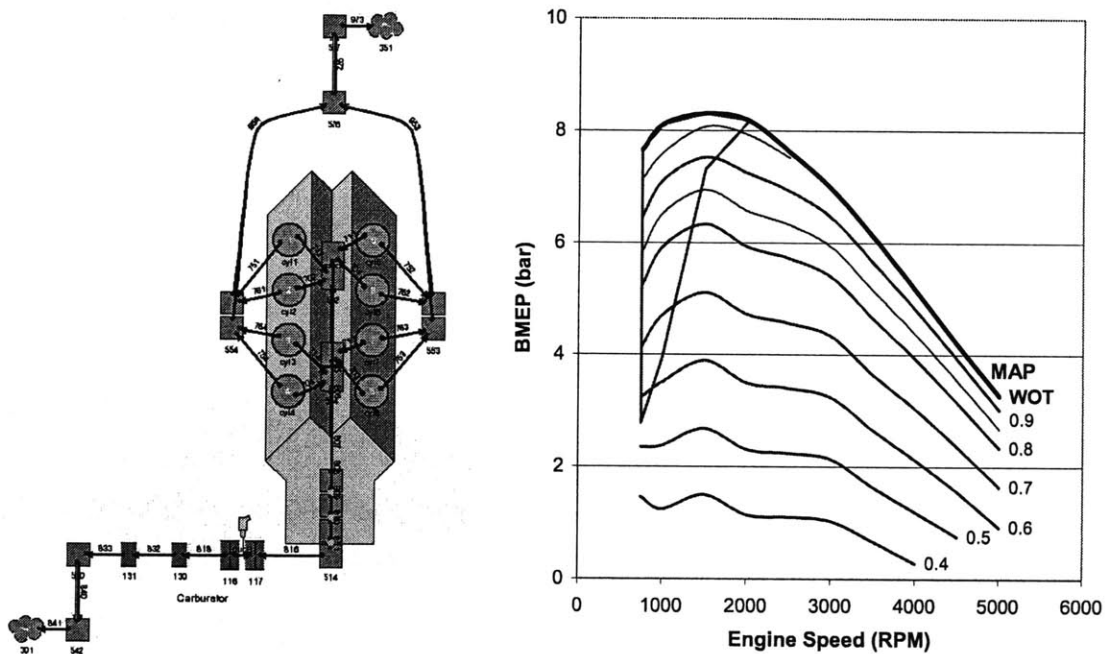
#### **7.3.1 HISTORIC (1951) SI ENGINE KNOCK LIMITED RANGE**

An engine model was created in WAVE to determine the knock limited range of a 1951 engine. The 1951 CRC data gives that the most common engine configuration for the year was the V-8 engine with a displaced volume of 4.0 L and a compression ratio of 7.0. The engine is carbureted and naturally aspirated. The spark plug is located on the side of the chamber, hence increasing the burn rate time by 40-50% [3]. The engine also only has 2 valves per cylinder. The engine model is shown in Figure 7.8.

With this engine model, the MBT timing was found over a range of operating conditions, ranging from a 750 rpm to 5000 rpm at different loads. The fuel was set to have an  $(R+M)/2$  value of 82, and WAVE's knock model was then actuated. The knock limited range was determined over the operating range of the engine. The engine map and the corresponding

knock-limited region are displayed in Figure 7.8 for an intake air temperature of 52°C. This high intake air temperature is due to the heating require for carburetors.

At 750 rpm, the engine is knock limited even when the MAP is 0.55 bar, due to the low speeds. As the speed increases, the knock-limited range of MAPs decreases. At 2000 rpm, the engine is only knock limited at wide open throttle. The engine is not knock limited above 2000 rpm.



**Figure 7.8: WAVE Model for a 1951 V-8 engine and the corresponding engine map. The area enclosed in red is the knock-limited range of engine speeds and intake-air pressures.**

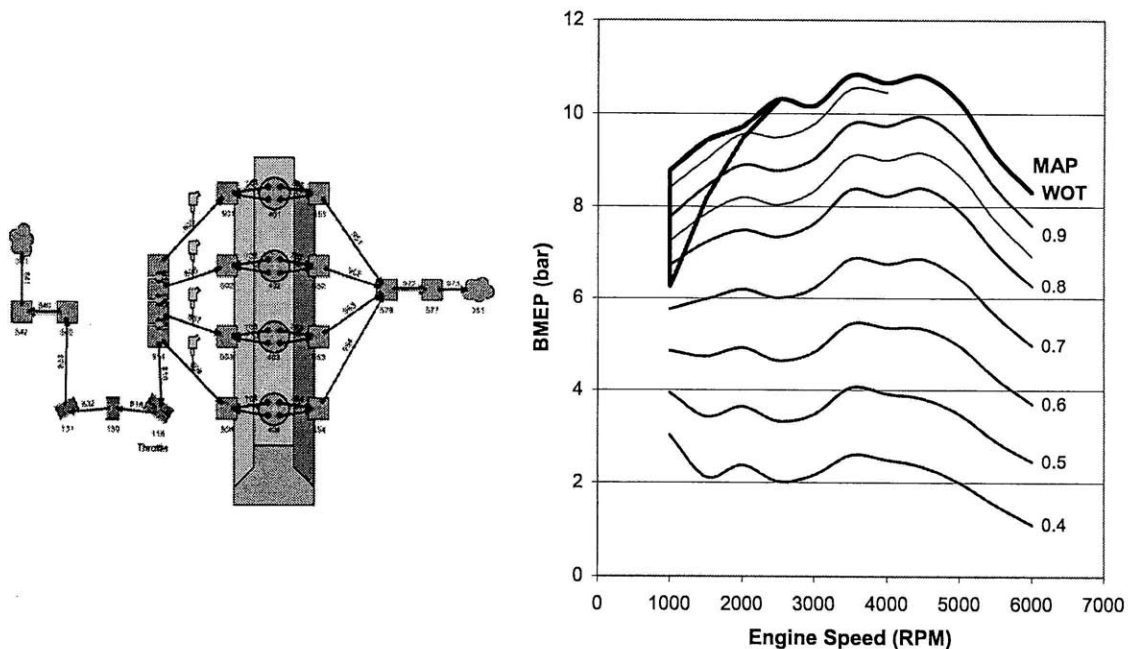
### 7.3.2 MODERN SI ENGINE KNOCK LIMITED RANGE

The engine model described in the previous section was updated to represent modern engine technology. The V-8 configuration was replaced with an inline 4-cylinder engine. The compression ratio was set to 9.5 with a displaced volume of 2.0 L. The carburetor was replaced with port fuel injectors, and the spark plug was moved to the top of the pent-roof. The engine is

still naturally aspirated. The engine also has 4 valves per cylinder. The engine model is shown in Figure 7.9.

Following the same procedure outlined in the above section, the operating map and the knock limited range for the engine was determined for engine speeds from 1000 rpm to 6000 rpm. The fuel was set to have an (R+M)/2 value of 91. The engine map and the corresponding knock-limited region are displayed in Figure 7.9, for an intake air temperature of 30°C.

At 1000 rpm, the engine is knock limited when the flow is throttled down to a MAP of 0.75 bar. At 2500 rpm, the engine is still knock limited at WOT, but at speeds above 2500 rpm, the engine is no longer knock limited.



**Figure 7.9: WAVE Model for a 2008 inline 4-cylinder engine and the corresponding engine map. The area enclosed in red is the knock-limited range of engine speeds and intake-air pressures.**

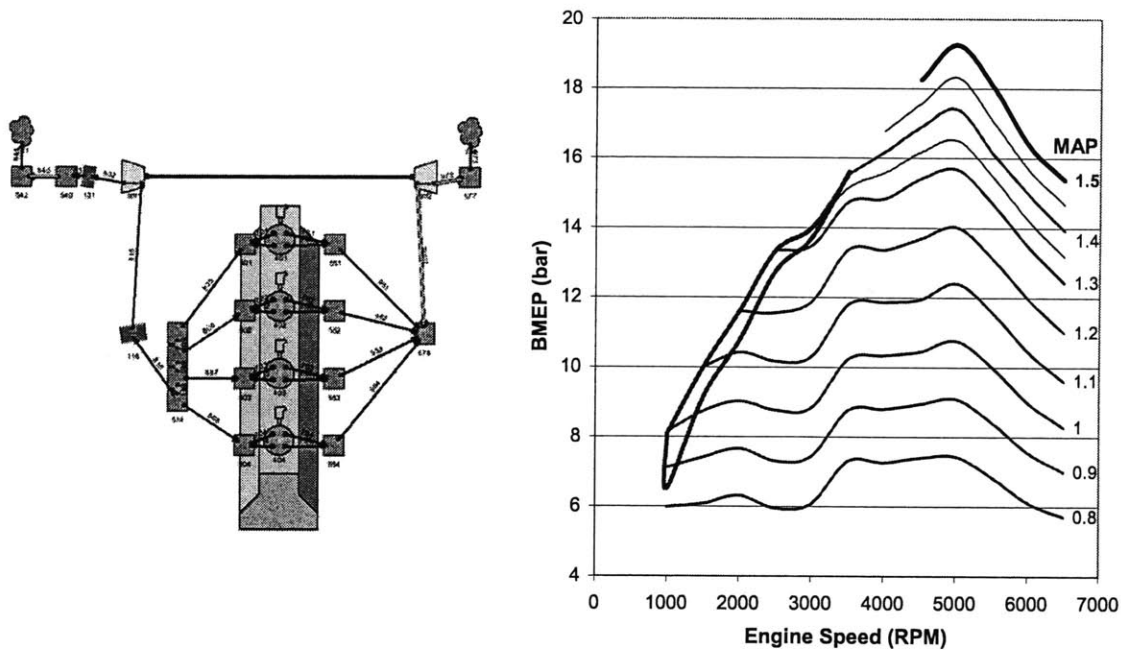
### 7.3.3 FUTURE SI ENGINE KNOCK LIMITED RANGE

Engines are moving towards downsized, boosted engine. So the “future” SI engine for this analysis is a downsized, boosted, 4-cylinder engine, and is loosely based on the GM EcoTec engine. The intake is connected to a turbocharger and intercooler. Since the turbocharger increases the power output from the engine significantly, the size of the engine can be decreased to 1.6 L. The compression ratio was decreased to 8.8 in order to decrease the knock-limited range. The engine has 4-valves per cylinder with variable valve timing. The port-fuel injectors are replaced with direct injectors. The engine model is shown in Figure 7.10.

The turbocharger map was approximated based off Figure 15.36 in [3]. There is no boost at 1000 rpm, and the amount of boost is increased until 4500 rpm, where it reaches a maximum of 50%, corresponding to an intake air pressure of 1.5 bar. An intercooler following the turbocharger brings the intake air temperature down. The charge cooling effects associated with direct injection further decreases the intake air temperature.

Following the same procedure outlined in the above sections, the operating map and the knock limited range for the engine was determined for engine speeds from 1000 rpm to 6500 rpm. The fuel was set to have an (R+M)/2 value of 91. The engine map and the corresponding knock-limited region are displayed in Figure 7.10 for an intake air temperature of 30°C, before taking into account charge cooling efforts.

At 1000 rpm, the engine is knock limited when the flow is throttled down to a MAP of 0.85 bar. This speed is less knock limited than the modern engine at this speed because the lower compression ratio and the use of charge cooling. As the speed increases, the amount of boost also increases, causing higher speeds to also be knock limited. At 3500 rpm, the engine is still knock limited at a MAP of 1.4 bar. At higher speeds, the model predicted that the engine was not knock limited.



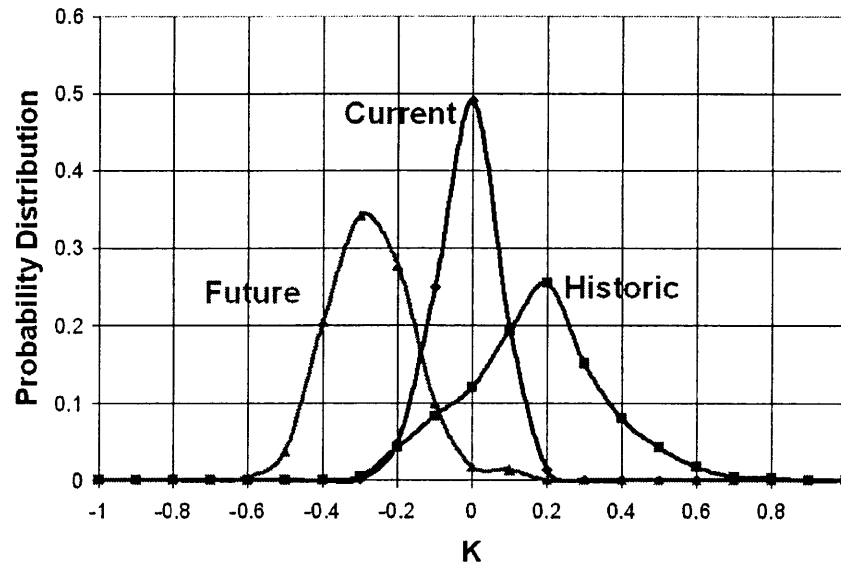
**Figure 7.10: WAVE Model for a future turbo-charged 4-cylinder engine and the corresponding engine map. The area enclosed in red is the knock-limited range of engine speeds and intake-air pressures.**

### 7.3.4 VALUES OF K FOR HISTORIC, CURRENT, AND FUTURE ENGINE

The knock limited ranges for the above models give the knock-limited speeds and their corresponding intake air pressures. The experimental results from Chapter 5 gives the relationship between values of K and the intake air pressure, the engine speed, and the intake air temperature. An even distribution of points was taken over the knock limited regions for each engine configuration. At each point, the engine speed, the intake air pressure, and the intake air temperature was used to determine the value of K. The probability distribution of K for each engine is shown in Figure 7.11.

The results show that the knock limited range of modern engines has an average K value of -0.02, with a  $2\sigma$  of 0.2. For modern engines, the RON, which corresponds to  $K=0$ , describes the knock-properties of a fuel well. The older engine has a higher value of K, with an average value

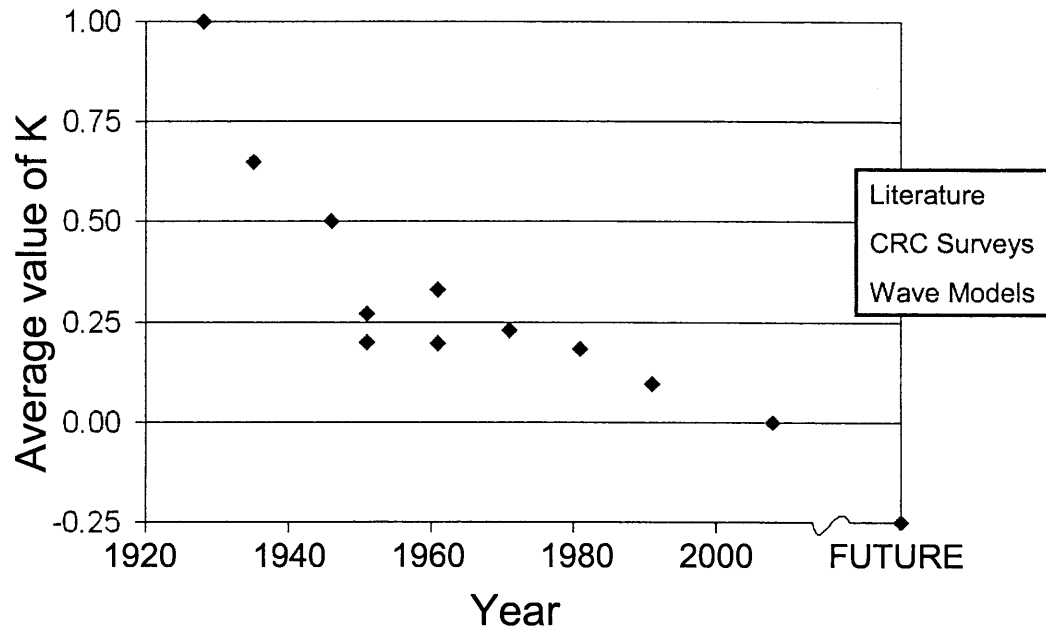
of 0.2 with a  $2\sigma$  of 0.5. It should be noted that though K was higher in 1951, it was still well below 0.5, which corresponds to  $(RON+MON)/2$ . Future engine trends are showing that K is becoming increasingly negative. The average value of K for the future engine was -0.3 with a  $2\sigma$  of 0.3. This shift in K is due to the increasing intake air pressure and the effective drop in the intake air temperature due to charge cooling.



**Figure 7.11: The statistical distribution of K values for a historic, current, and future engine. The knock limited range of conditions for each engine was found through WAVE; these conditions were then entered into the correlation presented in Chapter 5 to determine the value of K at the different engine operating conditions.**

## 7.4 CONCLUSIONS

The results for the above section are combined into Figure 7.12. This analysis shows that K has been decreasing since the invention of the octane number tests in 1928. Initially, the value of K decreased significantly due to advanced cooling techniques that decreased the maximum end-gas temperature. The value of K then continued to decrease as carburetors were replaced with fuel injectors which reduced the intake air temperature and hence increased the maximum end-gas temperature. K will continue to decrease as engines become turbo-charged and use direct-injection.



**Figure 7.12: The average value of K as a function of the year, found from literature (red), the CRC surveys (blue), and WAVE Models (green).**



## CHAPTER 8: MODIFICATIONS TO THE OCTANE NUMBER TESTS

Chapter 7 showed that  $K$  has decreased from a value of 1 in 1930 to being negative in 2008, and that as engines continue to be boosted,  $K$  will further decrease. A value of  $K$  between 0 and 1 is required for a fuel's OI to be bracketed by the MON and RON tests. However, when  $K$  is negative, the fuel's OI is no longer properly bracketed, and the RON and MON test lose their relevance in predicting a fuel's antiknock performance.

Chapters 5 and 6 showed the underlying cause of this problem. Since  $K$  relates the maximum end-gas temperature to the RON and MON tests, a negative  $K$  implies that the maximum end-gas temperatures are less than those of the RON and MON tests. The high end-gas temperature in the MON test creates a bias towards fuels with slow high temperature combustion, such as PRFs. However, for modern engines, the maximum end-gas temperatures at knock limited conditions are in the transition region between low and high temperature combustion. Therefore, optimal fuels for modern engines should have slow autoignition chemistry in that transition region. Therefore, a proper antiknock metric should characterize fuel chemistry in this region.

### 8.1 CHANGING REFERENCE FUELS

The spirit of the RON and MON tests is to simplify the autoignition chemistry of a complex fuel to that of a binary blend. The binary blend of iso-octane and n-heptane was originally selected because they were commercially available in 1928. However, since most fuels do not exhibit the negative-temperature coefficient of paraffins, a “logical” solution to correcting the octane number tests is to simply change the binary blend.

The binary reference blend is switched from being blends of iso-octane and n-heptane to blends of toluene and n-heptane. The Research Toluene Number (RTN) can then be defined as the percentage of toluene in binary blend that autoignites at the same compression ratio as the test fuel at RON conditions. The Motor Toluene Number (MTN) can similarly be defined to be the same as the RTN but at the MON conditions.

The RTN and MTN can be determined for a fuel by mapping that fuel's RON and MON value to a different scale. Figure 8.1 gives the RON and MON for different blends of toluene and n-heptane. A blend of 18.3% n-heptane and 81.7% toluene has a RON of 100 and a MON of 88.5. Therefore, if a fuel has a RON of 100, it would have an RTN of 81.7. Similarly, if a fuel has a MON of 88.5, it would have a MTN of 81.7. Table 8.1 shows the RTN that a fuel would have for a given RON and the MTN for a given MON.

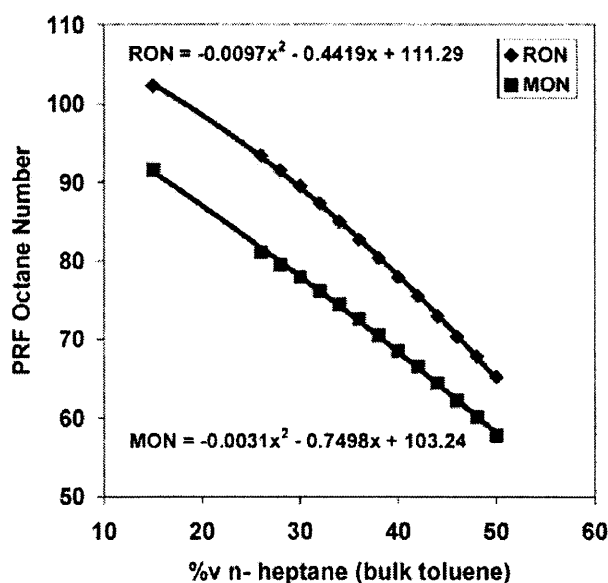


Figure 8.1: RON and MON of Toluene Reference Fuels as a function of the volumetric percentage of n-heptane [38].

RON	RTN
100.0	81.7
95.0	75.9
90.0	70.7
85.0	66.0
80.0	61.6
75.0	57.5
70.0	53.7
65.0	50.0

MON	MTN
100.0	95.7
95.0	89.5
90.0	83.5
85.0	77.7
80.0	72.2
75.0	66.9
70.0	61.7
65.0	56.7

Table 8.1: The Research and Motor Toluene Numbers (RTN and MTN) for a fuel based on its Research and Motor Octane Numbers (RON and MON)

Using Table 8.1, the RTN and MTN for PRF96, TRF96, and UTG96 were determined. The values, along with the RON and MON values are shown in Table 8.2. Since all three fuels have the same RON, they all have the same RTN. However, the MTN changes between the three different fuels. Since the reference fuel is now a TRF, TRF96 has no sensitivity and has an MTN of 78 equal to the RTN. PRF96 has a sensitivity of -12.5 with an MTN of 90.5. UTG96 has a sensitivity of -2.5 with an MTN of 80.5.

	RON	MON	(R+M)/2		RTN	MTN	(R+M)/2
PRF96	96.0	96.0	96.0		78.0	90.5	84.3
TRF96	96.1	84.5	90.3		78.0	78.0	78.0
UTG96	96.1	87.0	91.6		78.0	80.5	79.2

**Table 8.2: The Research and Motor Toluene Number for PRF96, TRF96, and UTG96**

Most commercial fuels have sensitivities similar to that of UTG96, and hence by changing the reference fuels, the sensitivity would be approximately zero. However, the issue arises in that fuels are designed to maximize their anti-knock quality. Therefore, fuels would begin to move towards being more like a PRF in order to boost the MTN number. However, as seen in Chapter 5, a PRF tends to have worse antiknock performance in a modern engine than a TRF with the same RON.

Therefore, simply changing the reference fuels will not suffice as the change needed to update the octane number tests.

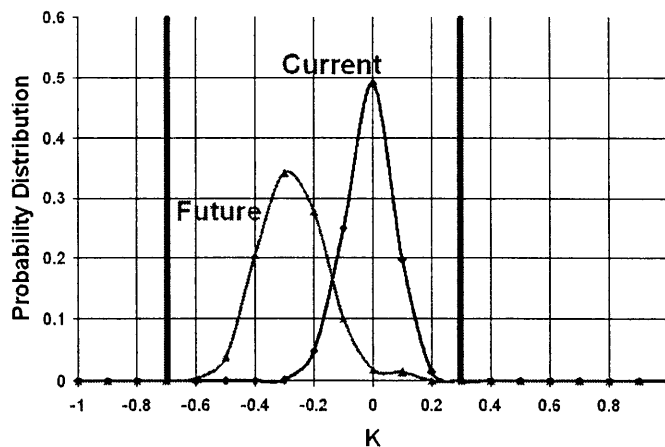
## 8.2 CHANGING THE ENGINE OPERATING CONDITIONS

As found in Chapter 5, the end-gas temperatures in the MON test are much higher than what is found in normal engines. Though lower, the end-gas temperatures in the RON test is still on the upper end of the spectrum of end-gas temperatures for modern engines. To properly bracket the test methods, the end-gas temperatures must be decreased for both tests. Therefore, the Octane Number tests need to be realigned to better bracket the knock limited regime. A much more comprehensive data set, including “on-the-road” data, would be required for a full analysis.

However, using the experimental data collected, an approach is presented to show how to determine improved test conditions for the RON and MON tests.

The proper test conditions can be determined through the distribution of K values for current and future engines presented in Section 7.3. As shown in Figure 8.2,  $K = -0.7$  and  $K = 0.3$  set the lower and upper bound of K values for the knock-limited regimes of these engines. Hence, if K for the RON test was shifted down to -0.7, and K for the MON test was shifted down to 0.3 (as opposed to 0 and 1 respectively), the tests would better bracket the knock limited operating region of both modern and near-future engines. A modified set of test conditions are given in Table 8.3, which correspond to these values of K. These test conditions were determined through the correlation developed in Chapter 5 that relates K to the engine operating conditions.

Modifying the octane tests to these conditions does not require changing the CFR Engine or the test procedures, since the spark location and compression ratio were found to not affect K. Changing the intake air temperature of the CFR Engine involves changing the heater setting, and the speed can be changed by interchanging the pulleys. However, changing the intake air pressure, would require the addition of a compressor.



**Figure 8.2: The statistical distribution of K values for current and future engines based off the WAVE models performed in Chapter 7. The red lines indicate the values of K that bracket the knock limited range of current and future engine.**

Engine Parameters	RON*	MON*
Intake air temperature (°C)	30	60
Intake air pressure (bar)	1.45	1
Engine Speed (rpm)	1200	3000

**Table 8.3: Suggested operating conditions for a modified RON and MON test**

The modified MON and RON values (denoted as MON\* and RON\*) of different fuels with these new operating conditions can be predicted from the following equation:

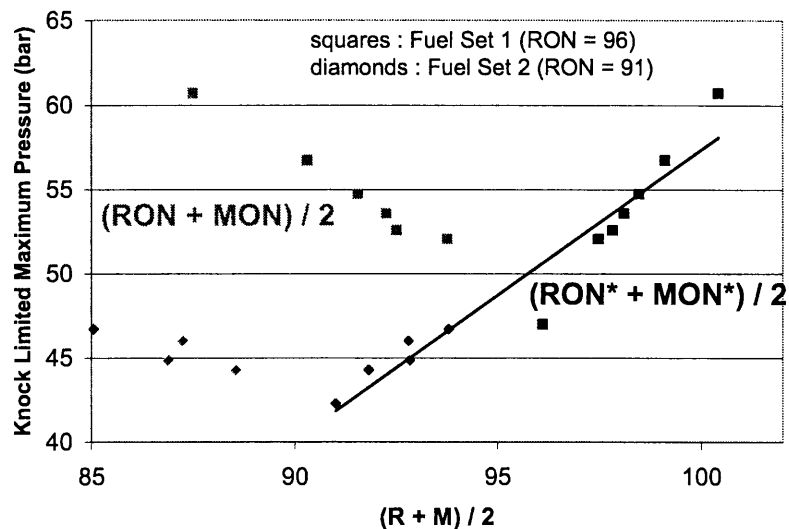
$$\begin{aligned}
 RON^* &= RON + 0.7(RON - MON) \\
 MON^* &= RON - 0.3(RON - MON)
 \end{aligned}
 \tag{8.1}$$

In Chapter 5, it was found that a normal knock-limited operating condition,  $K$  was negative, such that higher sensitivity fuels have a higher knock limited maximum pressure for a fixed RON. This data is replotted in Figure 8.3 as a function of  $(R+M)/2$  from the traditional test and the modified tests. With the traditional test, there is a discontinuity between the  $RON = 91$  and  $RON = 96$  values, but also, fuels with a lower  $(R+M)/2$  have better anti-knock performance. However, with the new testing conditions, the anti-knock performance of the fuel steadily increases with  $(R^*+M^*)/2$ .

It should be noted that with these approximations, the combination  $(R^*+M^*)/2$  can be written in terms of the current RON and MON as  $R+0.25(R-M)$ . Current US regulations set a minimum anti-knock index defined as  $R-0.5(R-M)$ . Thus, even if the test conditions are not changed, the anti-knock index could be modified to better reflect the anti-knock performance of modern fuels.

By changing the tests, the OI can be interpolated instead of extrapolated, minimizing inaccuracy. Additionally, having two test conditions that bracket the knock-limited regime embraces the original spirit of the RON and MON tests. However, merely changing the regulations would not be adequate as we move towards higher levels of boosting. Figure 5.13 shows that at high levels of boost,  $K$  is no longer independent of fuel. Therefore, as engines technology moves further and further into boosting, extrapolation from the current tests can be misleading.

One of the goals of this study was to develop a methodology for determining a more relevant set of octane number test engine operating conditions. The above represents a preliminary assessment. A more extensive set of tests is required to determine the full range of knock limited modern engine operating conditions, and the octane number test conditions that appropriately define fuel behavior for this range of conditions. Furthermore, as new engine technology is adopted, the tests should be continually updated to account for this new technology.



**Figure 8.3: The knock limited maximum pressure plotted against the average of the RON and the MON tests for the ASTM test case (gray) and for the modified tests described in this paper (black)**

### 8.3 BENEFIT OF CHANGING REGULATIONS

Changing the RON and MON tests requires a large capital cost. Rather than modifying the tests, the test regulations can be modified in light of the research presented in this thesis as well as in other sources [9,12,45]. The Coordinated Research Council is currently in the initial phases of a project to determine the effects of MON and RON on knock in commercial engines [46]. The ultimate goal of this project is to determine the optimum RON, MON, and sensitivity values of fuels.

Currently, fuels are required to have a minimum (R+M)/2 value and a minimum MON value. For a regular fuel, these values are 87 and 83, respectively. Therefore, fuel refiners are required to add expensive iso-paraffins into the fuel to increase the MON value to 83 [47]. However, this study found that increasing the MON value is counter-productive to increasing the antiknock properties of a fuel; thus, the MON requirement should be removed. The following scenarios look at the potential benefits of removing the MON requirement, using the modern and future engines modeled in Sections 7.3.2 and 7.3.3. The important engine parameters for this study are given in Table 8.4. The compression ratio was increased for each engine based off the values given in Table 8.5, which states that an OI increase of approximately 5.5 would allow for a compression ratio increase of 1.

Engine Parameters	Modern NA	Future TC, DI
Average Value of K	0	-0.3
Compression Ratio	9.5	8.8
Max Thermal Brake Efficiency (%)	31.217	33.135

**Table 8.4: The average value of K, compression ratio, and maximum thermal brake efficiency for a modern naturally aspirated engine and for a future downsized-boosted direct injected engine. The maximum thermal brake efficiencies for both engines occur at 5000 rpm.**

Engine Parameters	Parameter variation	Octane index variation
Compression ratio	+1	+4 to +7
Spark advance (°CA)	+1	+0.5 to +1
Intake air temperature (°C)	+25	+1 to +4
Intake air pressure (mbar)	-10	-0.5 to -1
Equivalence ratio	+0.2	-4
Hygrometry (g water / kg of dry air)	+4	-1

**Table 8.5: Engine parameters that effect octane requirements [40]**

Scenario 1: Removing the MON requirement:

For regular fuels, if the MON requirement vanishes, the MON value could decrease from 83 to 79 [40], causing the average fuel sensitivity to increase from 8 to 12. Since the average value of K is 0 for the NA engine, simply decreasing the MON of the fuel would not change the average OI of the fuel in that engine. However, for the TC-DI engine, this would correspond to an increase in the OI of 1.2. According to Table 8.5, the compression ratio could increase to 9.0. WAVE predicts that this increase in compression ratio would cause the brake thermal efficiency to increase to 33.345 percent.

The major benefit of this scenario is that the refineries would save on the cost (both energy and financially) of increasing the MON, hence decreasing the overall well-to-wheel carbon footprint.

Scenario 2: Increasing the RON from the energy savings from removing the MON requirement:

Removing the MON requirement would save the refiners money and energy; some of these savings could potentially be used to increase the RON. According to European Oil Company Organization for Environment, Health and Safety, the cost of increasing the RON of an unleaded fuel from 91 to 94 is negligible for a fixed sensitivity [48]. Keeping the sensitivity fixed at 12, the fuel could have a RON of 94 and a MON of 82.

For the NA engine, this would correspond to an increase in OI of 3, which in turn would correspond to an increase in compression ratio to 10.04. The WAVE model predicted that with this change in compression ratio, the brake thermal efficiency would increase to 31.844 percent, corresponding to a percentage increase of 2 percent. For the TC-DI engine, the compression ratio could be increased to 9.54, which increases the thermal brake efficiency to 33.987 percent. The percentage increase is 3 percent over the status quo.

The results for both parameters are given in Table 8.6, which shows that the increase in thermal brake efficiency can be substantial, especially for the second scenario for the TC-DI engine. Hence, removing the MON requirement would be beneficial to all parties involved. Car



companies would be able to increase their miles per gallons. Refineries would save money on refining the fuels. Customers would have to spend less money at the pump.

Engine Parameters	Modern NA	Future TC, DI
Scenario 1: Compression Ratio	9.50	9.00
Scenario 1: Max Thermal Brake Efficiency	31.217	33.345
Scenario 2: Compression Ratio	10.04	9.54
Scenario 2: Max Thermal Brake Efficiency	31.844	33.987

**Table 8.6: The increases in compression ratio and maximum thermal brake efficiency due to getting rid of the minimum MON requirement (Scenario 1) and by using the corresponding energy savings to increase the average fuel RON (Scenario 2).**

#### 8.4 CONCLUSION

In light of the research presented in the previous chapters, the current RON and MON test must be changed. The following modifications are evaluated:

- Changing the reference fuels does not improve the applicability of these tests.
- It is necessary to change the test conditions to accurately capture the autoignition quality of a fuel. A methodology is described that can be used to determine a new set of test conditions is presented.
- The benefits of getting rid of MON requirements are shown to be beneficial to car producers, oil companies, and consumers.

(this page intentionally left blank)

## CHAPTER 9: SUMMARY AND CONCLUSIONS

1. This study determined the relevancy of the Research and Motor Octane Number (RON and MON) tests in predicting the antiknock performance of fuels in modern spark ignition engines. In doing so, the following studies in the physical and chemical properties of knock were performed:

- Different instruments—pressure transducers, microphones, and accelerometers—were experimentally evaluated for measuring knock onset and knock intensity. It was found that for all three instruments, the knock intensity and excited frequencies depend on the instrument location. The first circumferential mode (6 kHz), the only audible excited frequency, was reliably picked up by most of the instruments at most locations. The intensity of this frequency correlates well with audible noise, which, though arbitrary, is perhaps the most reliable knock metric.
- Experiments were performed to determine the physical phenomena that govern knock onset in modern SI Engines. These experiments found that autoignition excites two ranges of frequencies, a lower audible range and a higher inaudible range. At the audible knock limit, individual cycle knock intensities above 2 bar start to occur in a few percent of the cycles at 6 kHz, the oscillation frequency within the audible range. As spark timing is advanced, the knock intensity increases, and the fraction of cycles with intensity above this threshold at 6 kHz increases rapidly. The CFR engine also was found to have two ranges of excited frequencies. The lower audible frequency is similar to that of the modern engine, though the higher inaudible frequencies are different.
- An experimental study was conducted to investigate what parameters effect K in the equation:  $OI = RON - K \times S$ . Where the OI is the Octane Index, a measure of the antiknock quality of fuel, the RON is the OI at a fixed condition, and S is the fuel sensitivity. The results showed that over most conditions K is negative, and hence for a given RON, fuels with a higher sensitive have better antiknock performance. The experimental data showed that K is strongly dependent on intake air temperature, engine speed, and intake air pressure. These trends agree with the results from chemical kinetic model calculations. It was then

found that K correlates the maximum end-gas temperatures in the engine to those of the RON and MON tests.

- Chemical kinetic model calculations were performed to investigate the fundamentals that determine the fuel's sensitivity. These model calculations showed that sensitivity indicates how "sensitive" a fuel's autoignition chemistry is to mixture temperature in the transition region, a region between high and low temperature combustion. On a more fundamental level, as sensitivity increases the fuel produces less hydroperoxy alkyl radicals and more aldehydes as intermediates. The hydroperoxy alkyl radicals have fast low temperature autoignition, while aldehydes are relatively unreactive at low temperatures. However, aldehydes autoignite very rapidly at high temperatures. Fuels with higher sensitivities (i.e. those that form aldehydes as an intermediate) have more stable  $RCH_2$  radicals, which facilitate the production of aldehydes.
- WAVE cycle simulations, octane requirement reports, and other literature were used to determine how the parameter K has shifted with time. An average value of K should be between 0 and 1 for the RON and MON tests to properly bracket the knock limited range of engines. This study found that K has been decreasing since the invention of the octane number tests in 1928 due to decreasing end-gas temperatures.

2. These results were used to determine the relevancy of the RON and MON tests and interpret K (the relative weighting of the two tests) and sensitivity (the difference between the two tests):

- Physically, modern engines have a complicated combustion chamber geometry (e.g. pent roof, hemi, etc...) compared to the pancake-shaped combustion chamber of a CFR Engine. This change in geometry results in a difference in the high frequency acoustic modes that are excited when an engine knocks. These modes are above the threshold of human hearing. However, since the bores of modern engines are similar to that of a CFR engine, both have a strong first circumferential mode at approximately 6 kHz, which is within the audible threshold. Therefore, the octane tests capture the physics of audible knock in modern engines.
- From the equation,  $OI = RON - K \times S$ , the  $K \times S$  term is the change in the OI when compared to the RON test. For modern engines, this difference was found to be due to changes in the endgas temperatures. K relates the maximum end-gas temperatures in an engine to that of

the RON and MON test.  $S$ , the fuel sensitivity, captures how the fuel will respond to these changes in temperature. As sensitivity increases, the fuel's autoignition delay time has a higher temperature dependence and hence has slower low temperature chemistry and faster high temperature chemistry. Since the autoignition integral for the two fuels approaches 1 at the same time in the RON test, lower end-gas temperatures would allow for sensitive fuels to have better antiknock performance. However, higher end-gas temperatures, such as those in the MON test, would allow for non-sensitive fuels to have better antiknock performance.

- Since, modern engines tend to operate at negative  $K$ , their maximum endgas temperature are below that of the RON and MON tests. The MON test operates at end-gas temperatures over 100 K hotter than modern engines, creating a bias towards fuels with good antiknock performance in the high temperature combustion region. Therefore, fuels with high sensitivities have poor antiknock performance at higher temperatures. However, good antiknock performance in the high temperature region corresponds to poor antiknock performance at lower temperatures. Since modern engines operate at these lower temperatures, for a given RON, fuels with a higher sensitive are more desirable than those with lower sensitivity.

3. A few possible techniques were examined that could increase the relevancy of the octane number tests for knock in modern engines:

- Changing the reference fuels without changing the test conditions does not improve the applicability of the tests.
- The results from this study suggest that test conditions should be changed to properly represent the autoignition chemistry of fuels in modern engines. The tests should be changed to properly bracket the knock limited range of conditions, hence allowing a value of  $K$  between 0 and 1. A methodology was presented for determining a more relevant set of RON and MON test engine operating conditions. A modified set of test conditions is presented, though a much more extensive survey of knock in modern engines is necessary to properly determine more appropriate test conditions.
- Removing the MON test requirements can result in a substantial increase in engine efficiency, while saving oil refineries money.

- This investigation into changing the octane tests is based off the underlying physics and chemistry in the engine. However, it does not address several key issues that would be necessary in modifying this established set of tests. Primarily, it does not address the change in capital or refining cost if the RON and MON test are in fact modified.

In conclusion, this study provided valuable insight into knock in both modern engines and in the octane tests. Though the octane tests capture the physical properties of knock in modern engines, the tests do not accurately capture the chemical properties of knock.

## APPENDIX A: THE CFR ENGINE

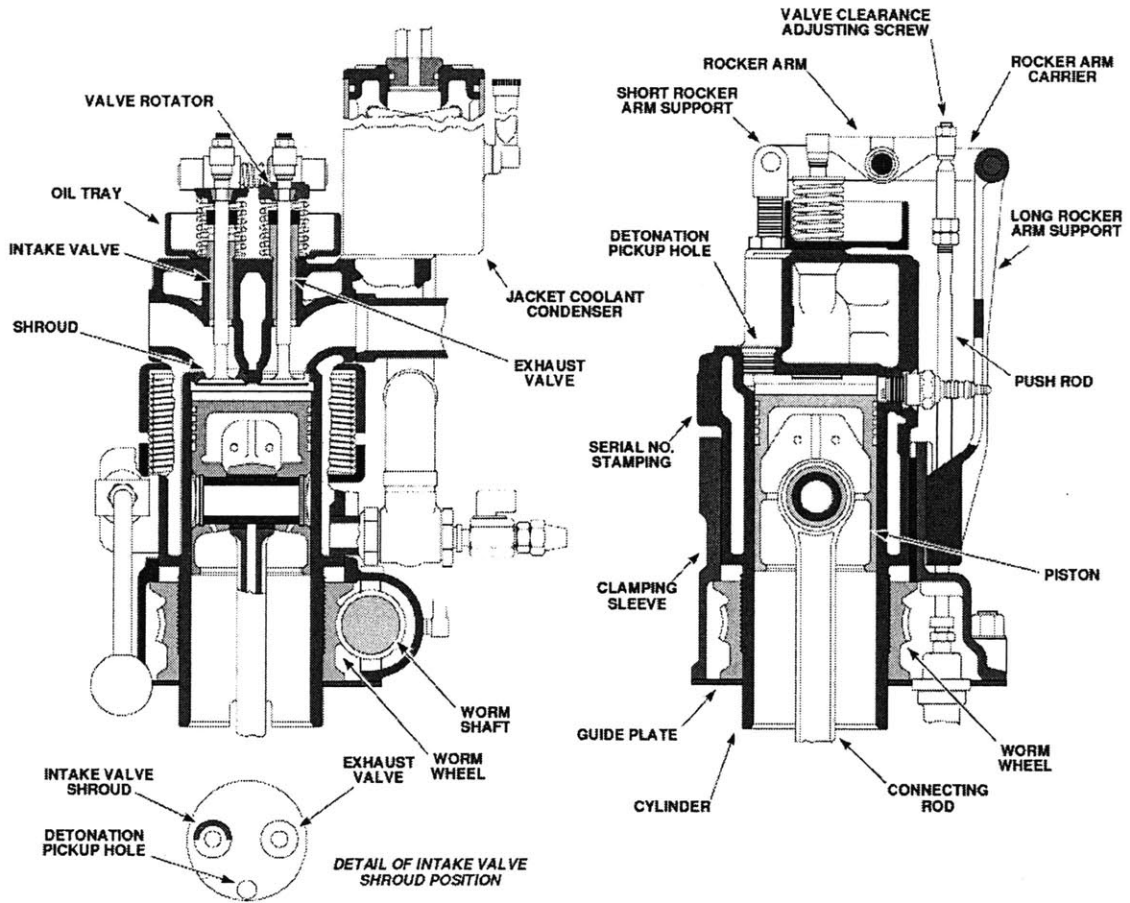


Figure A.1: The CFR Engine [35]

(this page intentionally left blank)



## APPENDIX B: MON AND RON OF DIFFERENT PURE HYDROCARBONS

	RON	MON	S	C	H	C-C	C=C	
2,2-Dimethylpentane	92.8	95.6	-2.8	7	16	6		Parrafin
2,2-Dimethylbutane	91.8	93.4	-1.6	6	14	5		Parrafin
Iso-Octane	100	100	0.0	8	18	7		Parrafin
2-Methylbutane	92.3	90.3	2.0	5	12	4		Parrafin
2,3-Dimethylpentane	91.1	88.5	2.6	7	16	6		Parrafin
n-Butane	95	92	3.0	4	10	3		Parrafin
1,1-Dimethylcyclopentane	92.3	89.3	3.0	7	14	7		Napthene
2,3,4-Trimethylpentane	102.7	95.9	6.8	8	18	7		Parrafin
2,3-Dimethylbutane	103.5	94.3	9.2	6	14	5		Parrafin
Methylcyclopentane	91.3	80	11.3	6	12	6		Napthene
Hex-2-ene	92.7	80.8	11.9	6	12	4	1	Olefin
2-Methylbut-2-ene	97.3	84.7	12.6	5	10	3	1	Olefin
Indane	103.5	89.8	13.7	9	10	7	3	Aromatic
4-Methylhex-2-ene	96.8	83	13.8	7	14	5	1	Olefin
Hex-3-ene	94	80.1	13.9	6	12	4	1	Olefin
3-Methylpent-1-ene	96	81.2	14.8	6	12	4	1	Olefin
2-Methylpent-1-ene	95.1	78.9	16.2	6	12	4	1	Olefin
Toluene	120	103.5	16.5	7	8	4	3	Aromatic
2,3-Dimethylbut-2-ene	97.4	80.5	16.9	6	12	4	1	Olefin
Propylene	102	85	17.0	3	6	1	1	Olefin
Cyclopenta-1,3-diene	103.5	86.1	17.4	5	6	3	2	Diolefin
Pent-2-ene	98	80	18.0	5	10	3	1	Olefin
Ethylcyclopropane	102.5	83.9	18.6	5	10	5		Napthene
Ethylene	100	81	19.0	2	4		1	Olefin
2-Methylbut-1-ene	102.5	81.9	20.6	5	10	3	1	Olefin
Methylcyclopentene	93.6	72.9	20.7	6	10	5	1	Diolefin
Cyclopentene	93.3	69.7	23.6	5	8	4	1	Diolefin

**Figure B.1: The RON and MON of different fuels [40]**

(this page intentionally left blank)

## WORKS CITED

- 1 Bureau of Transportation Statistics, "Number of U.S. Aircraft, Vehicles, Vessels, and Other Conveyances," available at [http://www.bts.gov/publications/national\\_transportation\\_statistics/](http://www.bts.gov/publications/national_transportation_statistics/)
- 2 "On the Road in 2035: Reducing Transportations Petroleum Consumption and GHG Emissions," A. Bandivadekar, K. Bodek, L. Cheah, C. Evans, T. Groode, J. Heywood, E. Kasseris, M. Kromer, and M. Weiss, Report from Laboratory for Energy and the Environment, MIT, July 2008.
- 3 Heywood, J.B., *Internal Combustion Engine Fundamentals*, McGraw-Hill, 1988.
- 4 By, A., Kempinski, B., and Rife, J.M., "Knock in Spark Ignition Engines." SAE paper 810147, 1981.
- 5 Konig, G., and Sheppard, C.G.W., "End Gas Autoignition and Knock in a Spark Ignition Engine," SAE Paper 902135, presented at the International Fuels and Lubricants Meeting and Exposition, Tulsa Oklahoma, October 22-25, 1990. Sequence of images comes from a video of high speed movies produced by G. Konig, J. Pan, and C.G.W. Sheppard in the research activity described in this paper.
- 6 Amann, C.A., "The Automotive Spark-Ignition Engine--An Historical Perspective," *History of the Internal Combustion Engine*, American Society of Mechanical Engineers, 1989.
- 7 Taylor, C.F., *The Internal-Combustion Engine in Theory and Practice*, vol 2, MIT Press, 1968.
- 8 Brooks, D.B., "A Review of the Development of Reference Fuel Scales for Knock Rating." SAE Paper 460230, presented at the SAE Annual Meeting, Detroit, MI, January 7-11, 1946.
- 9 Bartholomew, E., "New Knock-Testing Methods Needed to Match Engine and Fuel Progress." SAE Paper 610200, 1961.
- 10 American Society for Testing Materials: Designation: D 2699 – 03a, "Standard Test Method for Research Octane Number of Spark-Ignition Fuel", Annual book of ASTM Standards, vol. 5.05, 2003.
- 11 American Society for Testing Materials: Designation: D 2700 – 03a, "Standard Test Method for Motor Octane Number of Spark-Ignition Fuel", Annual book of ASTM Standards, vol. 5.05, 2003.
- 12 Kalghatgi, G.T., "Fuel Anti-Knock Quality – Part 1, Engine Studies", SAE paper 2001-01-3584, 2001.
- 13 Kalghatgi, G.T., "Fuel Anti-Knock Quality – Part 2, Vehicle Studies—How Relevant is Motor Octane Number (MON) in Modern Engines", SAE paper 2001-01-3585, 2001.
- 14 Ward's Automotive Group Databases: Light Vehicle Engines, North American Availability and Specifications for 2008.
- 15 Palucka, T., "The Wizard of Octane," *Invention & Technology*, Winter 2005.

- 16 The Ricardo Company, "What is WAVE," available at <http://www.ricardo.com/engineeringservices/software.aspx?page=wave>
- 17 Cheung, J.M., and Heywood, J.B., "Evaluation of a One-Zone Burn-Rate Analysis Procedure Using Production SI Engine Pressure Data," SAE paper 932749, presented at the SAE Fuels and Lubricants Meeting and Exposition, Philadelphia, PA, October 18-21, SAE Trans., Vol. 102, 1993.
- 18 Leppard, W.R., "The Chemical Origin of Fuel Octane Sensitivity", SAE paper 902137, 1990.
- 19 Tanaka, S., Ayala, F., and Keck, J.C., "A Reduced Chemical Kinetic Model for HCCI Combustion of Primary Reference Fuels in a Rapid Compression Machine," *Combustion and Flame*, Vol. 133, pp. 467-481, 2003
- 20 Andrae, J.C.G., Björnbom, P., Cracknell, R.F., and Kalghatgi, G.T., "Autoignition of Toluene Reference Fuels at High Pressures Modeled with Detailed Chemical Kinetics," *Combustion and Flame*, Vol. 149, pp. 2-24, 2007
- 21 Marinov, N. M, "A Detailed Chemical Kinetic Model for High Temperature Ethanol Oxidation," *Int. J. Chem. Kinet.* 31:183-220, 1999.
- 22 Sakai, Y., Ozawa, H., Ogura, T., Miyoshi, A., Koshi, M., and Pitz, W.J, "Effects of Toluene Addition to Primary Reference Fuel at High Temperature," SAE 2007-01-4104, 2007.
- 23 Naber, J.D., Blough, J.R., Frankowski, D., Goble, M., and Szpytman, J.E., "Analysis of Combustion Knock Metrics in Spark-Ignition Engines," presented at the 2006 SAE World Congress, Detroit, MI, April 3-6, 2006.
- 24 Syrimis, M., and Assanis, D.N., "Knocking Cylinder Pressure Data Characteristics in a Spark-Ignition Engine," *Trans. of the ASME*, Vol. 125, April, 2003.
- 25 Waukesha Engine Division, Dresser Industries, Inc., "An International Historic Mechanical Engineering Landmark: The Waukesha CFR Fuel Research Engine." Bulletin No. 1163. June 1980.
- 26 The Coordinated Research Council. Octane Number Requirement Surveys for 1951, 1961, 1971, 1981, 1991. CRC Reports CRC-266, CRC-357, CRC-448, CRC-525, CRC-580, 1992.
- 27 Draper, C.S., "Pressure Waves Accompanying Detonation in the Internal Combustion Engine," *Journal of the Aeronautical Sciences*, Vol. 5, 1938.
- 28 Scholl, D., Davis, C., Russ, S., and Barash, T., "The Volume Acoustic Modes of Spark-Ignited Internal Combustion Chambers," SAE paper 980893, presented at the International Congress & Exposition, Detroit, MI, February 23-26, 1998.
- 29 Eng., J.A., "Characterization of Pressure Waves in HCCI Combustion," SAE paper 2002-01-2859, presented at Powertrain & Fluid Systems Conference & Exhibition, San Diego, CA, October 21-24, 2002.

- 30 Chun, K.M., and Heywood, J.B., "Characterization of Knock in a Spark-Ignition Engine," SAE paper 890156, SAE International Congress & Exposition, Detroit, MI, February 27 – March 3, 1989.
- 31 Kleeman, A.P., Menegazzi, P., Henriot, S., and Marchal, A., "Numerical Study on Knock for an SI Engine by Thermally Coupling Combustion Chamber and Cooling Circuit Simulation," SAE 2003-01-0563, presented at the SAE World Congress, Detroit, MI, March 3-6, 2003.
- 32 Castagne, J.P., Dumas, J.P., Henriot, S., and Lafossas, F.A., "New Knock Localization Methodology for SI Engines," SAE paper 2003-01-1118, presented at the 2003 SAE World Congress, Detroit, MI, March 3-6, 2003.
- 33 Brunt, M.F.J., Pond, C.R., and Biundo, J., "Gasoline Engine Knock Analysis using Cylinder Pressure Data," SAE Paper 980896, presented at the International Congress & Exposition, Detroit, MI, February 23-26, 1998.
- 34 Douaud, A.M., and Eyzat, P., "Four-Octane-Number Method for Predicting the Anti-Knock Behavior of Fuels and Engines," SAE paper 780080, SAE Trans., Vol. 87, 1978.
- 35 Bizub, J., Dresser - Waukesha Engine Division, Private Communication, April 2009.
- 36 Swarts, A., Yates, A., Viljoen, C., and Coetzer, R., "A Further Study of Inconsistencies between Autoignition and Knock Intensity in the CFR Octane Rating Engine," SAE paper 2005-01-2081, 2005.
- 37 The Coordinated Research Council, "Road Rating Techniques," CRC-259, 1951.
- 38 Gerty, M.D., and Heywood, J.B., "An Investigation of Gasoline Engine Knock Limited Performance and the Effects of Hydrogen Enhancement," SAE paper 2006-0228, 2006 SAE World Congress, Detroit, MI, April 3-6, 2006.
- 39 Kalghatgi, G.T., Nakata, K., and Mogi, K., "Octane Appetite Studies in Direct Inject Spark Ignition (DISI) Engines," SAE paper 2005-01-0244, 2005.
- 40 Guibet, J.C., *Fuels and Engines, Institute Francais du Petrole Publications*, 1999.
- 41 Myers R.H., and Montgomery, D.C., *Response Surface Methodology: Process and Product Optimization Using Designed Experiments*. 2nd Edition, Wiley, 2002.
- 42 McMurry, J., *Organic Chemistry*, 6th Edition, Brooks/Cole, 2004
- 43 "New Tests for Gasoline Octane Ratings are Coming," Oil and Gas Journal, Vol 58, 1960.
- 44 Chon, D.M. and Heywood, J.B., "Performance Scaling of Spark-Ignition Engines: Correlation and Historical Analysis of Production Engine Data", SAE paper 2000-01-0565, 2000.
- 45 Milpied, J., Jeuland, N., Plassat, G., Guichaoua, S., Dioc, N., Marchal, A., Schmelzle, P., "Impact of Fuel Properties on the Performances and Knock Behavior of a Downsized Turbocharged DI SI Engine - Focus on Octane Numbers and Latent Heat of Vaporization," SAE paper 2009-01-0324.

- 46 Coordinated Research Council, "2008 Fall Performance Committee and Group Meetings," 2008.
- 47 Institute of Petroleum. *Modern Petroleum Technology*, 5th Edition Part II. Wiley 1984.
- 48 European Oil Company Organization for Environment, Health and Safety (CONCAWE), "Assesment of the Energy Balances and Economic Consequences of the Reduction and Elimination of Lead in Gasoline." CONCAWE Report 11/83R.